

Derivatives and Inverse of Cascaded Linear+Nonlinear Neural Models

M. Martinez-Garcia^{1,2}, P. Cyriac³, T. Batard³, M. Bertalmío³, J. Malo^{1*}

¹ Image Processing Lab., Univ. València, Spain

² Instituto de Neurociencias, CSIC, Alicante, Spain

³ Information and Communication Technologies Dept., Univ. Pompeu Fabra, Barcelona, Spain

* jesus.malo@uv.es

Abstract

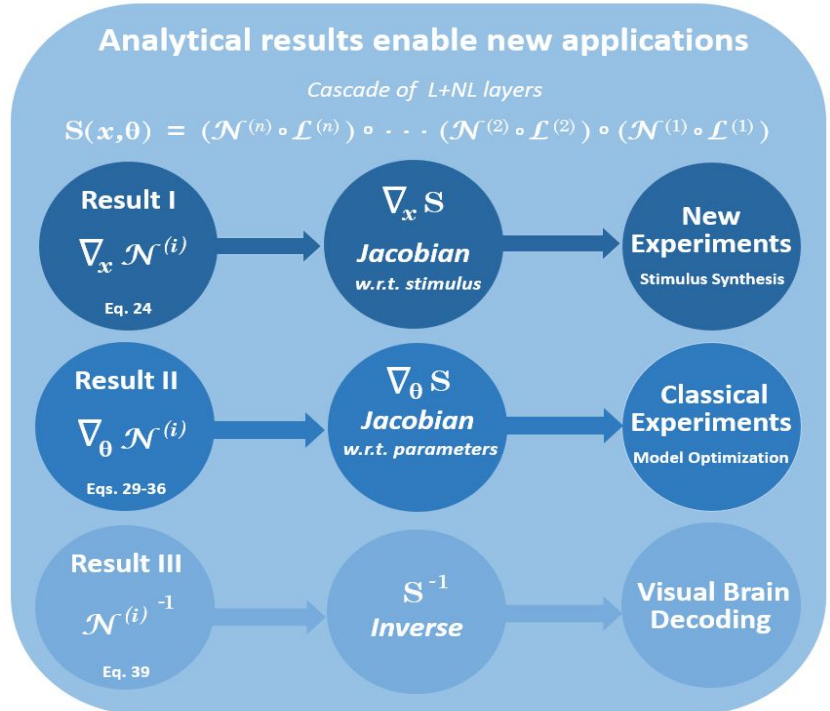
In vision science, cascades of *Linear+Nonlinear* transforms are very successful in modeling a number of perceptual experiences [1]. However, the conventional literature is usually too focused on only describing the *forward* input-output transform.

Instead, in this work we present the mathematics of such cascades beyond the forward transform, namely the Jacobian matrices and the inverse. These analytic results are important for three reasons: (a) they are strictly necessary in new experimental methods based on the synthesis of visual stimuli with interesting geometrical properties, (b) they are convenient to learn the model from classical experiments or alternative goal optimization, and (c) they are a promising model-based alternative to blind machine-learning methods for neural decoding. Moreover, the statistical properties of the neural model are more intuitive by using this kind of vector formulation.

The theory is checked by building and testing a vision model that actually follows the modular program suggested in [1]. Our *derivable* and *invertible* model consists of a cascade of modules that account for brightness, contrast, energy masking, and wavelet masking. To stress the generality of this modular setting we show examples where some of the canonical *Divisive Normalization* modules are substituted by equivalent modules such as the *Wilson-Cowan* interaction model [2,3] (at the V1 cortex) or a tone-mapping model [4] (at the retina). In the Discussion we address three illustrative applications. First, we show how the *Jacobian (w.r.t. the input)* plays a major role in setting the model by allowing novel psychophysics based on the geometry of the neural representation (as in [5]). Second, we show how the *Jacobian (w.r.t. the parameters)* can be used to find the model that better reproduces classical psychophysics of image distortion. In fact, thanks to the presented derivatives, this cascade of isomorphic canonical modules has been psychophysically tuned to work together for the first time. Third, we show how the analytic *inverse* may improve regression-based visual brain decoding.

Contents

1	Introduction	3
2	Results	5
2.1	Notation and general considerations	5
	Stimuli as vectors	5
	The visual pathway: modular L+NL architecture	5
	Canonical and alternative nonlinearities	7
	Jacobian matrices of L+NL cascades	8
	Jacobian and perceptual distance	11
2.2	Result I: Jacobian with regard to the stimulus	12
2.3	Result II: Jacobian with regard to the parameters	13
2.4	Result III: Analytic inverse	15
3	Discussion	16
3.1	Jacobian with regard to the image in stimulus synthesis	18
3.2	Jacobian with regard to the parameters in model optimization	22
3.3	Analytic inverse in visual brain decoding	26
4	Concluding remarks	28
5	Supplementary Materials	i
5.1	A cascaded L+NL vision model	i
5.2	Derivative of a linear function with regard to its parameters	iv
5.3	Derivation of the Jacobian with regard to the stimulus	vi
5.4	Derivation of the Jacobian with regard to the parameters	vii
5.5	Derivation of the inverse	x
5.6	Region-based approach to MAXimum Differentiation	x
5.7	Maximization of correlation with subjective opinion	xii
5.8	The BioMultiLayer-L+NL Toolbox	xiii
5.9	Toolbox-oriented matrix properties	xviii



1 Introduction

The mathematics of *Linear+Nonlinear* (L+NL) transforms is interesting in neuroscience because cascades of such modules are key in explaining a number of perceptual experiences [1]. For instance, in vision, perceptions of color, motion and spatial texture are tightly related to L+NL models of similar functional form [6–8]. The literature is usually focused on describing the behavior, i.e. setting the parameters of the *forward* input-output transform. However, understanding the transform computed by the sensory system, S , goes beyond predicting the output from the input. The mathematical properties of the model (*formulation* of S , *derivatives*, ∇S , and *inverse*, S^{-1}), are also relevant, both in *visual neuroscience* and in related applied disciplines like *image processing*.

Formulation is relevant. In visual neuroscience, the classical *image processing-like* notation based on *filters* is appropriate only if the response of a population of sensors can be seen as a convolution of the input with the *receptive field* function(s). In this classical setting the physical dimensions of the signal domain are explicit (e.g. space, time, and wavelength), so that visual stimuli are 4-dimensional objects ready to be sampled and filtered.

However, a more abstract view of the function carried out by the system (e.g. Efficient Coding [9, 10]) is more intuitive by using a *vector notation* in high-dimensional spaces, i.e. by considering the manifolds where the stimuli live [11, 12]. This *vector notation* of the stimuli, as in current *statistical learning* [13], is practical to think about the population of sensors as feature extractors (as opposed to filters) that map the input into a different representation, where *location* and *distances* are relevant for stimuli discrimination and decision making. In this alternative setting, the vector notation stresses the relevance of the *geometry* of the neural representation. The cascade of transforms in the model S can also be seen as a series of deformations of the input representation. This geometrical view is important both to propose information theoretic interpretations of behavior [14–21] and to propose experimental techniques based on distances and subspaces [5, 22–25]. For example, this change of perspective in the consideration of images (from two-dimensional arrays to d -dimensional vectors) led image processing from classical *Wiener filtering* denoising [26], to *projection-onto-the-manifold* denoising such as, for instance, Kernel Singular Value Decomposition [27].

Derivatives are relevant. The Jacobian, ∇S , represents a local linear approximation of the nonlinear system, S . The dot product definition of *receptive field* introduced for linear systems [15, 28] could be extended to nonlinear systems using the Jacobian matrix with regard to the stimulus. Therefore, this Jacobian is convenient to properly formulate concepts such as adaptive (stimulus dependent) receptive fields or adaptive features. The change of variable theorem [29, 30] implies that the Jacobian w.r.t. the stimulus controls how the volume element is enlarged or compressed in the deformations suffered by the representation along the neural pathway. Given the relation between the information and the volume of the signal manifold [31, 32], this Jacobian plays an important role in determining the amount of information lost (or neglected) along the neural pathway. Riemannian geometry describes how metric matrices change under nonlinear transforms [30]. As a result, subjective distances also depend on the Jacobian w.r.t. the stimulus [33–35], and these distances characterize the discrimination ability (or threshold psychophysics). This Jacobian is also the key to characterize the propagation of noise throughout the system [36]. Therefore when discrimination is related to the noise at the internal representation [25, 37, 38], thresholds at the input space are also characterized by the Jacobian w.r.t. the input. Novel psychophysical techniques such as Maximum Differentiation [5, 22–24] synthesize stimuli for the experiments through the gradient of the perceptual distance, and it depends on the Jacobian w.r.t. the input. On the other hand, characterizing the Jacobian w.r.t. the parameters is also important. First, it is relevant in order to learn the L+NL cascade that better reproduces classical experiments (e.g. physiological responses or psychophysical judgements), as opposed to approaches that rely on exhaustive search (as in [35, 39–41]). Second, an explicit expression for this Jacobian is important to understand the optimization for alternative goals such as optimal coding, as opposed to approaches that rely on implicit automatic differentiation (as in [42]).

Reliable subjective image distances (and hence the Jacobian w.r.t. stimulus) have paramount relevance in image processing applications judged by human viewers [43–45]. Examples include

tone mapping and contrast enhancement [46], image coding [33, 34, 47], motion estimation and video coding [39, 48, 49], denoising [50, 51], visual pattern recognition [52], or search in image databases [53]. In all these cases, either the subjective distance between the original and the processed image has to be minimized, or the distance used to find image matches has to be perceptually meaningful.

Inverse is relevant. In neuroscience, visual brain decoding [54–56] may benefit from the analytic inverse, S^{-1} , because it may lead to improvements of the current techniques based on blind regression [57]. Interestingly, the benefits of the inverse may not only be limited to straightforward improvements on the decoded images: the inverse may also give rise to alternative methods to determine the parameters of the model. For instance, the best parameters of S would be those that lead to better reconstructions through the corresponding S^{-1} . Note that another relevant point of the Jacobian is its relation to the inverse: according to the theorem of the inverse function [29], the non-singularity of the Jacobian is the necessary condition for the existence of the inverse.

In the image processing side, the relevance of the inverse is obvious in perceptual image/video coding where the signal is transformed to the perceptual representation prior to quantization [34, 47–49]: decompression implies the inverse to reconstruct the image. Another example is white balance based on human color constancy (or chromatic adaptation): in general, adaptation may be understood as a transform to an invariant representation which is insensitive to irrelevant changes (as for instance the nature of the illumination) [19, 20, 58]. Models of this class of invariant representations could be easily applied for color constancy if the transform is invertible.

In this paper we derive three analytic results for neural models consisting on cascades of canonical Linear+Nonlinear modules: (i) the Jacobian with regard to the stimulus, (ii) the Jacobian with regard to the parameters, and (iii) the inverse.

We discuss the use of the above results in the context of an illustrative *derivable* and *invertible* vision model made of L+NL modules that address brightness perception, contrast computation, energy masking, and orientation/scale masking. Specifically, we discuss the use of the analytical derivatives to get the parameters of different L+NL layers: (1) the Jacobian with regard to the image is used for stimuli generation in *geometry*-based psychophysics as in [5], and (2) the Jacobian with regard to the parameters is used to maximize the alignment with subjective distortion measures, improving the brute-force approaches in [35, 39, 41]. Finally, (3) we discuss how the analytic inverse may be a successful alternative to decoding techniques based on blind linear regression [59] or nonlinear kernel-ridge regression [56]. Analytic results and applications can be reproduced using the associated **BioMultiLayer-L+NL** toolbox.

Following the spirit of formulae compendia such as [60, 61], the expressions derived here are a necessary reference for further research on a specific L+NL layer. For instance, note that the cascaded framework is useful to optimize one layer at a time (assuming reasonable values for the other layers). In this work, all the analytic results and proofs are given for the canonical *divisive normalization* [1]. Nevertheless, we also provide examples where some of the normalization modules are substituted by equivalent NL layers such as the Wilson-Cowan interaction [2, 3] (at the V1 cortex) or a tone-mapping model [4] (at the retina). In fact, this cascade of isomorphic canonical modules that follows the program suggested in [1] has been psychophysically tuned to work together for the first time thanks to the presented analytic results. Interestingly, the PDFs of the responses along the network suggest that this psychophysically tuned architecture also has interesting statistical properties. This is remarkable since this statistical behavior was not imposed a-priori in any way. Therefore, consistently with previous reports in individual layers [62, 63], this is an additional evidence in favour of the Efficient Coding Hypothesis [9, 10].

Despite the relevance of these ubiquitous neural models, the above mathematical issues have not been addressed in the experimental literature. Interestingly, even though the machine learning literature deals with similar (deep) architectures [64], these details are not made explicit either because of the increasing popularity of automatic differentiation [65]. For instance, in [42, 66] biologically plausible L+NL architectures are optimized according to psychophysical data or to efficient coding principles. Unfortunately, the Jacobian w.r.t. the parameters was hidden behind automatic differentiation. In this situation, explicit expressions showing the role of biologically relevant parameters will provide intuition and insight.

2 Results

2.1 Notation and general considerations

Stimuli as vectors

An *image* in the retina, $\mathbf{x}^0(\mathbf{p}, \lambda)$, is a function describing the spectral irradiance in each spatial location, \mathbf{p} , and wavelength, λ . Assuming a dense enough sampling, the continuous input image can be represented by a discrete hyperspectral array with no information loss. The specific sampling pattern has no major relevance since the continuous signal can always be obtained from the discrete signal [67]. Here we will assume Cartesian sampling in space and wavelength. Cartesian sampling implies that the hyperspectral array consists of b matrices of size $h \times w$, where the l -th matrix represents the discrete spatial distribution of the energy of l -th discrete wavelength ($l = 1, \dots, b$). In vision models the spatio-spectral resolution of human viewers should determine the sampling frequencies. Given the cut-off frequencies of the achromatic and chromatic CSFs [68, 69], and given the smoothness of the achromatic and opponent spectral sensitivities [70, 71], the spatial dimensions may be sampled at about 80 samples/degree (cpd) and the spectral dimension at about 0.1 samples/nm [72].

Using an appropriate rearrangement of the hyperspectral array, the input image can be thought as a *vector* in a d_0 -dimensional space,

$$\mathbf{x}^0(\mathbf{p}, \lambda) \xrightarrow{\text{vect}} \mathbf{x}^0 = \begin{pmatrix} x_1^0 \\ x_2^0 \\ \vdots \\ x_k^0 \\ \vdots \\ x_{d_0}^0 \end{pmatrix} \quad (1)$$

i.e. the input stimuli, $\mathbf{x}^0(\mathbf{p}, \lambda)$, which are functions defined in a discrete 3-dimensional domain, are rearranged as a d_0 -dimensional *column vectors*, $\mathbf{x}^0 = \text{vect}(\mathbf{x}^0(\mathbf{p}, \lambda)) \in \mathbb{R}^{d_0 \times 1}$, where $d_0 = h \times w \times b$. Note that with the considered sampling frequencies, the dimension of the input stimuli is *huge* even for moderate image sizes (small angular field in the visible spectral range).

The particular scanning pattern in the rearrangement function, $\text{vect}(\cdot)$, has no major relevance as long as it can be inverted back to the original spatio-spectral domain. Here we will use the *last-dimension-first* convention used in the `Matlab` functions `im2col.m` and `col2im.m`. The selected rearrangement pattern has no fundamental effect, but it has to be taken into account to make sense of the structure of the matrices of the model acting on the input vector.

This rearrangement function, $\text{vect}(\cdot)$, will be also a convenient choice when computing derivatives with regard to the elements of the matrices involved in the model.

The visual pathway: modular L+NL architecture.

The visual system may be thought as an operator, S , transforming the input d_0 -dimensional vectors (stimuli) into d_n -dimensional output vectors (or sets of d_n responses),

$$\mathbf{x}^0 \xrightarrow{S(\mathbf{x}^0, \Theta)} \mathbf{x}^n \quad (2)$$

where $\mathbf{x}^n \in \mathbb{R}^{d_n \times 1}$ is the response vector, and Θ is the set of parameters of the model. Vectorial output is equivalent to considering d_n separate sensors (or mechanisms) acting on the stimulus, \mathbf{x}^0 , leading to the corresponding individual responses, x_k^n , where $k = 1, 2, \dots, d_n$. In this view, the k -th sensor would be responsible for the k -th dimension of the response vector, \mathbf{x}^n . The number of separate sensors analyzing the signal may not be the same as the input dimension, so in general $d_n \neq d_0$. The number of parameters of the model, d_Θ , depends on the specific functional form of the considered transform.

As suggested in [1], the global response described above may be decomposed as a series of feed-forward elementary operations, or a cascade of n modules (stages or layers), $S^{(i)}$, where $i = 1, 2, \dots, n$,

$$\begin{array}{c}
S(x^0, \Theta) \\
\curvearrowright \\
x^0 \quad x^1 \quad x^2 \dots x^{i-1} \quad x^i \dots x^{n-1} \quad x^n \\
\begin{array}{ccccccc}
\curvearrowright & \curvearrowright & & \curvearrowright & & \curvearrowright & \\
S^{(1)} & S^{(2)} & & S^{(i)} & & S^{(n)} &
\end{array}
\end{array} \quad (3)$$

i.e. the global response is the composition of the elementary responses:

$$S = S^{(n)} \circ S^{(n-1)} \circ \dots \circ S^{(2)} \circ S^{(1)}$$

The intermediate representations of the signal along this response path may have different dimension, i.e. $\mathbf{x}^i \in \mathbb{R}^{d_i \times 1}$, because the number of mechanisms in stage $S^{(i)}$ may be different from the number of mechanisms in $S^{(i-1)}$. Each layer in the above deep network architecture has its own parameters, $\mathbf{x}^{i+1} = S^{(i)}(\mathbf{x}^i, \Theta^i)$. Again, d_{Θ^i} , depends on the specific functional form of the i -th layer. Each layer performs a linear+nonlinear (L+NL) operation:

$$\dots \mathbf{x}^{i-1} \xrightarrow{\mathcal{L}^{(i)}} \mathbf{y}^i \xrightarrow{\mathcal{N}^{(i)}} \mathbf{x}^i \dots \quad (4)$$

i.e. each layer is a composition of two operations: $S^{(i)} = \mathcal{N}^{(i)} \circ \mathcal{L}^{(i)}$. Let us briefly note that, while in most models the linear operation is followed by the nonlinear one, which is why we use this formulation here, in some instances an inverted scheme of a nonlinear+linear model might be more suitable [73, 74]. That scenario can be handled by our framework as well, after some trivial modification (e.g. choosing the linear operation in the first layer of the L+NL model to be the identity, so that the first layer becomes in practice the nonlinear operation of the first layer followed by the linear operation of the second layer, and the whole cascade gets shifted into a NL+L form).

The linear operation, $\mathcal{L}^{(i)}$, is represented by a matrix $L^i \in \mathbb{R}^{d_i \times d_{i-1}}$. The number of rows in the matrix L^i corresponds to the number of *linear* sensors in layer $S^{(i)}$. This number of mechanisms determines the dimension of the linear output, $\mathbf{y}^i \in \mathbb{R}^{d_i \times 1}$,

$$\mathbf{y}^i = L^i \cdot \mathbf{x}^{i-1} \quad (5)$$

In the nonlinear operation, $\mathcal{N}^{(i)}$, each output of the previous linear operation undergoes a saturation transform. Phenomena such as *masking* or *lateral inhibition* imply that the saturation of y_k^i should depend on the neighbors $y_{k'}^i$, with $k' \neq k$. This saturation is usually formalized using *divisive normalization* [1]. This adaptive saturation is a canonical neural operation and it is at the core of models for color [71], motion [75], and spatial texture vision [8]. Nevertheless, other alternative nonlinearities may be considered as discussed below. In general, this saturating interaction will depend on certain parameters θ^i ,

$$\mathbf{x}^i = \mathcal{N}^{(i)}(\mathbf{y}^i, \boldsymbol{\theta}^i) \quad (6)$$

Summarizing, in this cascaded setting, the parameters of the i -th layer are (1) the weights of the bank of *linear* sensors represented in $\mathcal{L}^{(i)}$ (the rows of the matrix L^i), and (2) the parameters of the nonlinear saturating interaction, $\mathcal{N}^{(i)}$, i.e.

$$\Theta^i = \{L^i, \theta^i\} \quad (7)$$

Note that according to Eq. 5, the rows of the L^i play the same scalar-product role as standard linear receptive fields [15, 28]). The only difference is that the rows of L^i are defined in the space of vectors \mathbf{x}^{i-1} instead of being defined in the input image space (of vectors \mathbf{x}^0).

Canonical and alternative nonlinearities

Divisive Normalization in matrix notation. The conventional expressions of the *canonical* divisive normalization saturation use an element-wise formulation [1],

$$x_k^i = \mathcal{N}^{(i)}(\mathbf{y}^i, \boldsymbol{\theta}^i)_k = \text{sign}(y_k^i) \frac{|y_k^i|^{\gamma^i}}{b_k^i + \sum_{k'} H_{kk'}^i |y_{k'}^i|^{\gamma^i}} = \text{sign}(y_k^i) \frac{|y_k^i|^{\gamma^i}}{\mathcal{D}^{(i)}(|\mathbf{y}^i|)_k} = \text{sign}(y_k^i) \frac{e_k^i}{\mathcal{D}^{(i)}(\mathbf{e}^i)_k} \quad (8)$$

This expression, in which the *energy* of each linear response is $e_k^i = |y_k^i|^{\gamma^i}$, combines conventional *matrix-on-vector* operations (such as the product $H \cdot \mathbf{e}$ in the denominator) with a number of *element-wise* operations: the division of each coefficient of the vector in the numerator by the corresponding coefficient of an inhibitory *denominator vector*, $\mathcal{D}^{(i)}$; the element-wise absolute value (or rectification) to compute the *energy*; the element-wise exponentiation; the element-wise computation of sign, and its preservation in the response through an element-wise product. Therefore, the parameters of this divisive normalization are: the excitation and inhibition exponent, γ ; the semisaturation constants in the vector, \mathbf{b} ; and the interaction matrix in the denominator, H ,

$$\boldsymbol{\theta}^i = \{\gamma^i, \mathbf{b}^i, H^i\}$$

The matrix-on-vector operation in the denominator is key in understanding *masking* and *adaptation*. This is because the k -th row of H^i describes how the neighbor activities $|y_{k'}^i|^{\gamma^i}$ saturate (or mask) the response of the k -th nonlinear response. The effect of these parameters are extensively analyzed elsewhere [1].

From a formal perspective, the combination of element-wise and matrix-on-vector operations in the conventional expression makes differentiation and inversion from Eq. 8 extremely cumbersome. This can be alleviated by a matrix-vector expression where the individual coefficients, k , are not explicitly present. Incidentally, this matrix expression will imply more efficient code in matrix-oriented environments such as **Matlab**.

In order to get such matrix-vector form, it is convenient to recall the equivalence between the element-wise (or Hadamard) product and the operation with diagonal matrices [61]. Given two vectors \mathbf{a} and \mathbf{b} , their Hadamard product is:

$$\mathbf{a} \odot \mathbf{b} = \mathbb{D}_{\mathbf{a}} \cdot \mathbf{b} = \mathbb{D}_{\mathbf{b}} \cdot \mathbf{a} \quad (9)$$

where $\mathbb{D}_{\mathbf{a}}$ is the diagonal matrix with vector \mathbf{a} in the diagonal.

Using the matrix form of the Hadamard product and the definitions of *energy*, $\mathbf{e}^i = |\mathbf{y}^i|^{\gamma^i}$ and *denominator vector*, $\mathcal{D}^{(i)}(\mathbf{e}^i) = \mathbf{b}^i + H^i \cdot \mathbf{e}^i$, the conventional Divisive Normalization, Eq. 8, can be re-written with diagonal matrices without referring to the individual components of the vectors:

$$\mathbf{x}^i = \mathcal{N}^{(i)}(\mathbf{y}^i, \boldsymbol{\theta}^i) = \mathbb{D}_{\text{sign}(\mathbf{y}^i)} \cdot \mathbb{D}_{(\mathbf{b}^i + H^i \cdot \mathbf{e}^i)}^{-1} \cdot \mathbf{e}^i = \mathbb{D}_{\text{sign}(\mathbf{y}^i)} \cdot \mathbb{D}_{\mathcal{D}^{(i)}(\mathbf{e}^i)}^{-1} \cdot \mathbf{e}^i \quad (10)$$

where the model parameters are $\boldsymbol{\theta}^i = \{\gamma^i, \mathbf{b}^i, H^i\}$. Similarly to Von-Kries adaptation [76], this matrix form of Divisive Normalization is nonlinear because the diagonal of the matrix depends on the signal. The derivation of the results (proofs given in the Supplementary Materials) shows that the above matrix version of Divisive Normalization is extremely convenient to avoid cumbersome individual element-wise partial derivatives and to compute the analytic inverse.

Alternative nonlinearities: Wilson-Cowan equations and tone-mapping. Even though all the elementary L+NL layers of the deep network in Eq. 3 could be implemented by a composition of Eqs. 5 and 10 (as suggested in [1]), here we also consider particular alternatives for the nonlinearities that have been proposed to account for the response at specific stages in the visual pathway. Namely, the Wilson-Cowan equations [2,3], which could account for the masking between local-oriented sensors [41]; and nonlinear models of brightness perception such as the ones used in tone mapping [4,63,77]. The consideration of these alternatives for specific stages stresses the generality of the proposed framework since, as shown in the examples of the Discussion, the network equations can be applied no matter the specific functional form of each stage (provided the elementary derivatives and inverses are known).

The Wilson-Cowan equations [2,3] describe the temporal evolution of the mean activity of a population of neurons at the V1 cortex. In what follows, we consider the following form of the Wilson-Cowan equations

$$\dot{\mathbf{x}}^i(t) = -\alpha \mathbf{x}^i(t) + \mu W \cdot f(\mathbf{x}^i(t)) + \lambda \mathbf{y}^i \quad (11)$$

where α, μ, λ are coupling coefficients, $W = W_{k,k'}$ is a kernel which decays with the difference $|k - k'|$, f is a sigmoid function and t is time.

The steady-state equation of the evolution equation (11) is

$$0 = -\alpha \mathbf{x}^i + \mu W \cdot f(\mathbf{x}^i) + \lambda \mathbf{y}^i \quad (12)$$

Existence and uniqueness of the solution of the steady-state equation (11) are not guaranteed in the general case. We refer the reader to [78] for some conditions on the coefficients α, μ, λ and the sigmoid f for which the existence and uniqueness of the solution is guaranteed.

From now on, we assume that we are in a case where we have existence and uniqueness of the solution of the steady-state equation. Then, we define the Wilson-Cowan transform $N^{(i)}(\mathbf{y}^i)$ of \mathbf{y}^i as the unique solution \mathbf{x}^i of the steady-state equation.

While the Wilson-Cowan equations are sensible for populations of cortical neurons, brightness-from-luminance models may account for nonlinearities at earlier stages of the visual pathway (e.g. in the retina). An illustrative example of these specific nonlinearities which is connected to image enhancement applications through tone mapping is the two-gamma model in [77]. In this model the nonlinear saturation is a simple exponential function with no interaction between neighbor dimensions,

$$\mathbf{x} = \text{sign}(\mathbf{y}) \odot |\mathbf{y}|^{\gamma(|\mathbf{y}|)} \quad (13)$$

where all operations (sign, rectification, exponentiation) are dimension-wise. However, note that the exponent is a function of the magnitude of the input tristimulus value. Specifically,

$$\gamma(|\mathbf{y}|) = \gamma_H - (\gamma_H - \gamma_L) \cdot \frac{\mu_1^m}{(\mu_1^m + |\mathbf{y}|^m)} \quad (14)$$

The exponent has different values for low and high inputs, γ_L and γ_H respectively (hence the two-gamma name). The transition of γ between γ_L and γ_H happens around the value $|\mathbf{y}| = \mu_1$. This transition is smooth, and its sharpness is controlled by the exponent m .

This expression for γ has statistical grounds since the resulting nonlinearity approximately equalizes the PDF of luminance values in natural scenes [63,79], which is a sensible goal in the information maximization context [80]. This nonlinearity can be applied both to linear luminance values [77,81] as well as to linear opponent color channels [58,82]. Therefore, this specific nonlinearity could be applied after a linear stage where the spectrum in each spatial location is transformed into opponent tristimulus values. Special modification of the nonlinearity around zero is required to address the singularity of the derivative in zero. We will be more specific on this point when we address the Jacobian of this two-gamma model below.

Jacobian matrices of L+NL cascades

In the modular setting outlined above, variation of the responses may come either from variations of the stimulus, \mathbf{x}^0 , or from variations of the parameters, Θ . On the one hand, for a given set of fixed parameters, many properties of the sensory system depend on how the output depends on the stimuli, i.e. many properties depend on the Jacobian of the transform with regard to the image, $\nabla_{\mathbf{x}^0} S$ (where the subindex at the derivative operator indicates the derivation variable). In particular, this Jacobian is critical to decode the neural representation (existence of inverse), and to describe perceptual distance between stimuli. As an example, the Discussion shows how this Jacobian is key in the generation of stimuli fulfilling certain geometric requirements involved in recent psychophysics. On the other hand, when looking for the parameters that better explain certain experimental behavior, it is necessary to know how the response depends on the parameters, i.e. the key is the Jacobian with regard to the parameters, $\nabla_{\Theta} S$. As an

example, the Discussion shows how this Jacobian can be used to maximize the correlation with subjective opinion in visual distortion psychophysics.

In these notation preliminaries we address the general properties of these Jacobian matrices (both $\nabla_{\mathbf{x}^0} S$ and $\nabla_{\Theta} S$) in the context of the modular network outlined above. The interest of these preliminaries is that we show that the problem of computing $\nabla_{\mathbf{x}^0} S$ and $\nabla_{\Theta} S$ reduces to the computation of the Jacobian matrices of the elementary nonlinearities ($\nabla_{\mathbf{y}^i} \mathcal{N}^{(i)}$ and $\nabla_{\theta^i} \mathcal{N}^{(i)}$ respectively). These elementary Jacobians, $\nabla_{\mathbf{y}^i} \mathcal{N}^{(i)}$ and $\nabla_{\theta^i} \mathcal{N}^{(i)}$, and the inverse, $\mathcal{N}^{(i)-1}$ (whose existence is related to $\nabla_{\mathbf{y}^i} \mathcal{N}^{(i)}$), are the three analytical results of the paper, and will be addressed in the next subsections. Specifically, for the divisive normalization, in Eq. 24 (result I), Eqs. 29-36 (result II), and Eq. 39 (result III).

Local-linear approximation. The response function, S , can be seen as a nonlinear change of coordinates depending on the (independent) variables \mathbf{x}^0 and Θ . Therefore, around certain $(\mathbf{x}_A^0, \Theta_A)$, this function can be expanded in Taylor series and its properties depend on the matrices of derivatives with regard to these variables [29,30], in this case, the Jacobian matrices $\nabla_{\mathbf{x}^0} S$ and $\nabla_{\Theta} S$,

$$\Delta \mathbf{x}^n = \nabla_{\mathbf{x}^0} S \cdot \Delta \mathbf{x}^0 + \nabla_{\Theta} S \cdot \Delta \Theta \quad (15)$$

This is the *local-linear approximation* of the nonlinear response for small perturbations of the stimulus or the parameters. In Eq. 15 the derivatives are computed at $(\mathbf{x}_A^0, \Theta_A)$, the vector $\Delta \mathbf{x}^0 \in \mathbb{R}^{d_0 \times 1}$ is the variation of the stimulus; and $\Delta \Theta \in \mathbb{R}^{d_{\Theta} \times 1}$ is a vector with a perturbation of the d_{Θ} parameters in the model. Note that the column vector of model parameters (of dimension d_{Θ}) is obtained simply by concatenating the parameters of the different layers.

The Jacobian with regard to the parameters necessarily has variables from different layers, so it makes an extensive use of the chain rule. Therefore, let's start with the Jacobian with regard to the stimulus and then, let's introduce the chain rule for this simpler case.

Global Jacobian with regard to the stimulus. At certain point \mathbf{x}_A^0 , one may make independent variations in all the dimensions of the input. Note that statistical independence of the dimensions of the stimuli is a different issue (different from formal mathematical independence in the expression). Actually, in general, the dimensions of natural stimuli are not statistically independent [10,20]. Omitting the (fixed) parameters, Θ_A , for the sake of clarity, the Jacobian with regard to the input is the following concatenation (independent variables imply concatenation of derivatives [29,30]),

$$\nabla_{\mathbf{x}^0} S(\mathbf{x}_A^0) = \left[\frac{\partial \mathbf{x}^n(\mathbf{x}_A^0)}{\partial x_1^0}, \dots, \frac{\partial \mathbf{x}^n(\mathbf{x}_A^0)}{\partial x_j^0}, \dots, \frac{\partial \mathbf{x}^n(\mathbf{x}_A^0)}{\partial x_{d_0}^0} \right]$$

where $\frac{\partial \mathbf{x}^n(\mathbf{x}_A^0)}{\partial x_j^0} \in \mathbb{R}^{d_n \times 1} \quad \forall j$. Expanding these column vectors, we see that $\nabla_{\mathbf{x}^0} S \in \mathbb{R}^{d_n \times d_0}$:

$$\nabla_{\mathbf{x}^0} S(\mathbf{x}_A^0) = \begin{bmatrix} \frac{\partial \mathbf{x}^n(\mathbf{x}_A^0)_1}{\partial x_1^0} & \frac{\partial \mathbf{x}^n(\mathbf{x}_A^0)_1}{\partial x_j^0} & \frac{\partial \mathbf{x}^n(\mathbf{x}_A^0)_1}{\partial x_{d_0}^0} \\ \vdots & \vdots & \vdots \\ \frac{\partial \mathbf{x}^n(\mathbf{x}_A^0)_k}{\partial x_1^0} & \dots & \frac{\partial \mathbf{x}^n(\mathbf{x}_A^0)_k}{\partial x_j^0} & \dots & \frac{\partial \mathbf{x}^n(\mathbf{x}_A^0)_k}{\partial x_{d_0}^0} \\ \vdots & \vdots & \vdots & \vdots & \vdots \\ \frac{\partial \mathbf{x}^n(\mathbf{x}_A^0)_{d_n}}{\partial x_1^0} & \frac{\partial \mathbf{x}^n(\mathbf{x}_A^0)_{d_n}}{\partial x_j^0} & \frac{\partial \mathbf{x}^n(\mathbf{x}_A^0)_{d_n}}{\partial x_{d_0}^0} \end{bmatrix} \quad (16)$$

Note that this Jacobian may depend on the input, \mathbf{x}^0 , because the *slope* of the response (the behavior of the system) may be different in different points of the stimulus space.

Note also that, for fixed parameters, according to Eq. 15, the global nonlinear behavior of the system can be linearly approximated in a neighborhood of some stimulus, \mathbf{x}_A^0 , using the Jacobian with regard to the stimulus, i.e. variations of the response linearly depend on variations of the input for small distortions $\Delta \mathbf{x}^0$.

Chain rule: global Jacobian in terms of the Jacobians of the layers. The Jacobian of the composition of functions (e.g. the multi-layer architecture we have here), can be decomposed as the product of the individual Jacobian matrices. For example, given the composition, $f \circ g \circ h = f(g(h(x)))$, the application of the *chain rule* leads to:

$$\nabla_{\mathbf{x}} f(g(h(x))) = \frac{\partial f}{\partial \mathbf{x}} = \frac{\partial f}{\partial g} \cdot \frac{\partial g}{\partial h} \cdot \frac{\partial h}{\partial \mathbf{x}} = \nabla_g f \cdot \nabla_h g \cdot \nabla_{\mathbf{x}} h$$

Note that when inputs and outputs are multidimensional (*matrix chain-rule*) the order of the product of Jacobians is important for obvious reasons. Following the above, the Jacobian of the cascade can be expressed in terms of the Jacobian of each layer:

$$\nabla_{\mathbf{x}^0} S = \nabla_{\mathbf{x}^{n-1}} S^{(n)} \cdot \nabla_{\mathbf{x}^{n-2}} S^{(n-1)} \cdot \dots \cdot \nabla_{\mathbf{x}^{i-1}} S^{(i)} \cdot \dots \cdot \nabla_{\mathbf{x}^1} S^{(2)} \cdot \nabla_{\mathbf{x}^0} S^{(1)} = \prod_{i=n}^1 \nabla_{\mathbf{x}^{i-1}} S^{(i)} \quad (17)$$

Similarly to $\nabla_{\mathbf{x}^0} S$, in general $\nabla_{\mathbf{x}^{i-1}} S^{(i)}$ is point-dependent and rectangular. Note that $\nabla_{\mathbf{x}^{i-1}} S^{(i)} \in \mathbb{R}^{d_i \times d_{i-1}}$. Given the L+NL structure of each layer, $S^{(i)} = \mathcal{N}^{(i)} \circ \mathcal{L}^{(i)}$, we can also apply the chain rule inside each layer,

$$\nabla_{\mathbf{x}^{i-1}} S^{(i)} = \nabla_{\mathbf{y}^i} \mathcal{N}^{(i)} \cdot L^i \quad (18)$$

where we used the trivial derivative of a linear function [60]: $\nabla_{\mathbf{x}^{i-1}} \mathcal{L}^{(i)} = \nabla_{\mathbf{x}^{i-1}} L^i \cdot \mathbf{x}^{i-1} = L^i$.

Note that assuming we know the parameters of the system (the linear weights, L^i , in each layer, and the parameters of the nonlinearities, θ^i), after Eqs. 17 and 18 the final piece to compute the Jacobian of the system with regard to the stimulus is the Jacobian of the specific nonlinearities, $\nabla_{\mathbf{y}^i} \mathcal{N}^{(i)}$. Solving this remaining unknown will be the first analytical result of the paper (Result I), namely Eq. 24.

Jacobian with regard to the parameters. For a given set of parameters, Θ_A , one may introduce independent perturbations in the parameters of each layer. Therefore, the Jacobian with regard to the (independent) parameters is the following concatenation,

$$\nabla_{\Theta} S = \begin{bmatrix} \nabla_{\Theta^1} S & \nabla_{\Theta^2} S & \dots & \nabla_{\Theta^n} S \end{bmatrix} \quad (19)$$

where each $\nabla_{\Theta^i} S \in \mathbb{R}^{d_n \times d_{\Theta^i}}$ is a rectangular matrix with d_{Θ^i} being the dimension of Θ^i ; and the input (\mathbf{x}_A, Θ_A) was omitted for the sake of clarity. Note that actual independence among the different parameters is different from formal mathematical independence in the expression. In fact, certain interaction between layers can be required to get certain computational goal.

Applying the chain rule for the Jacobian with regard to the parameters of the i -th layer,

$$\begin{aligned} \nabla_{\Theta^i} S &= \frac{\partial \mathbf{x}^n}{\partial \mathbf{x}^{n-1}} \cdot \frac{\partial \mathbf{x}^{n-1}}{\partial \mathbf{x}^{n-2}} \cdot \dots \cdot \frac{\partial \mathbf{x}^{i+1}}{\partial \mathbf{x}^i} \cdot \frac{\partial \mathbf{x}^i}{\partial \Theta^i} \\ &= \left[\prod_{l=n}^{i+1} \nabla_{\mathbf{x}^{l-1}} S^{(l)} \right] \cdot \nabla_{\Theta^i} S^{(i)} \end{aligned} \quad (20)$$

Note how Eq. 20 makes sense, both dimensionally and qualitatively. First, note that $\prod_{l=n}^{i+1} \nabla_{\mathbf{x}^{l-1}} S^{(l)} \in \mathbb{R}^{d_n \times d_i}$ and $\nabla_{\Theta^i} S^{(i)} \in \mathbb{R}^{d_i \times d_{\Theta^i}}$. Second, it makes sense that the effect of changing the parameters in the i -th layer has two terms: one describing how the change affects the response of this layer (given by $\nabla_{\Theta^i} S^{(i)}$), and other describing the propagation of the perturbation through the remaining layers of the network (given by the product of the other Jacobians -with regard to the stimulus-, $\prod_{l=n}^{i+1} \nabla_{\mathbf{x}^{l-1}} S^{(l)}$).

Now, taking into account that in each layer the parameters come from the linear and the nonlinear parts, and these could be varied independently, we obtain:

$$\nabla_{\Theta^i} S^{(i)} = \begin{bmatrix} \nabla_{L^i} S^{(i)} & \nabla_{\theta^i} S^{(i)} \end{bmatrix} = \begin{bmatrix} \frac{\partial \mathbf{x}^i}{\partial \mathbf{y}^i} \cdot \frac{\partial \mathbf{y}^i}{\partial L^i} & \nabla_{\theta^i} \mathcal{N}^{(i)} \end{bmatrix}$$

where we applied the chain rule in the Jacobian with regard to the matrix L^i , and the fact that, by definition, $\nabla_{\theta^i} S^{(i)} = \nabla_{\theta^i} \mathcal{N}^{(i)}$.

Further development of the first term requires the use of the derivative of a linear function with regard to the elements in the matrix L^i . This technical issue is addressed in the Supplementary Material 5.2. Using the result derived there, namely Eq. 68, the above equation reduces to:

$$\nabla_{\theta^i} S^{(i)} = \begin{bmatrix} \nabla_{\mathbf{y}^i} \mathcal{N}^{(i)} \cdot \mathbf{B}_{(\mathbf{x}^{i-1})^\top}^{d_i} & \nabla_{\theta^i} \mathcal{N}^{(i)} \end{bmatrix} \quad (21)$$

where, as stated in Eq. 68, $\mathbf{B}_{(\mathbf{x}^{i-1})^\top}^{d_i}$ is just a block diagonal matrix made from d_i replications of the (known) vector \mathbf{x}^{i-1} , and this expression assumes that the elements of the perturbations ΔL^i are vector-arranged row-wise, e.g. using $\text{vect}(\Delta L^{i\top})$. Note that in Eq. 21, the only unknown terms are the Jacobian of the nonlinearity: $\nabla_{\mathbf{y}^i} \mathcal{N}^{(i)}$, already referred to as the first analytical result of this work (Eq. 24), and $\nabla_{\theta^i} \mathcal{N}^{(i)}$, which will be the second analytical result of the work (Result II), namely Eqs. 29-36.

Jacobian and perceptual distance

In the input-output setting represented by S , perceptual decisions (e.g. discrimination between stimuli) will be made on the basis of the information available in the response (output) space and not in the input space. This role of the response space in stimulus discrimination is consistent with (i) the psychophysical practice that assumes uniform just noticeable differences in the response domain to derive the slope of the response from experimental thresholds [6, 8, 58], and (ii) the formulation of subjective distortion metrics as Euclidean measures in the response domain [33–35, 83].

Perceptual distance: general expression. The perceptual distance, \mathfrak{d}_p , between two images, \mathbf{x}_A^0 and \mathbf{x}_B^0 , can be defined as the *Euclidean distance in the response domain*:

$$\mathfrak{d}_p^2(\mathbf{x}_A^0, \mathbf{x}_B^0) = |\mathbf{x}_B^n - \mathbf{x}_A^n|_2^2 = (\mathbf{x}_B^n - \mathbf{x}_A^n)^\top \cdot (\mathbf{x}_B^n - \mathbf{x}_A^n) = \Delta \mathbf{x}^{n\top} \cdot \Delta \mathbf{x}^n \quad (22)$$

An Euclidean distance in the response domain implies a non-Euclidean measure in the input image domain [25, 30, 33, 35, 84]. One may imagine that, for nontrivial S^{-1} , the inverse of the points in the sphere of radius $|\Delta \mathbf{x}^n|_2$ around the point \mathbf{x}_A^n will no longer be a sphere (not even a convex region!) in the input space. The size and orientation of these *discrimination regions* determine the visibility of distortions $\Delta \mathbf{x}^0$ on top of certain background image, \mathbf{x}_A^0 . Different Euclidean lengths in the image space (different $|\Delta \mathbf{x}^0|_2$) will be required in different directions in order to lead to the same perceptual distance \mathfrak{d}_p . The variety of orientations and sizes of the well-known Brown-MacAdam color discrimination regions [85] is an intuitive (just three-dimensional) example of the above concepts.

Perceptual distance: 2nd-order approximation. Assuming the local-linear approximation of the response around the reference image, Eq. 15, we have $\Delta \mathbf{x}^n = \nabla_{\mathbf{x}} S(\mathbf{x}_A^0) \cdot \Delta \mathbf{x}^0$. Under this approximation, the perceptual distance from the reference image reduces to:

$$\mathfrak{d}_p^2(\mathbf{x}_A^0, \mathbf{x}_B^0) = \Delta \mathbf{x}^{0\top} \cdot \nabla_{\mathbf{x}} S(\mathbf{x}_A^0)^\top \cdot \nabla_{\mathbf{x}} S(\mathbf{x}_A^0) \cdot \Delta \mathbf{x}^0, \quad (23)$$

with $\mathbf{x}_B^0 = \mathbf{x}_A^0 + \Delta \mathbf{x}^0$. Therefore, the matrix $M(\mathbf{x}_A^0) = \nabla_{\mathbf{x}} S(\mathbf{x}_A^0)^\top \cdot \nabla_{\mathbf{x}} S(\mathbf{x}_A^0)$ plays the role of a non-Euclidean metric matrix induced by the sensory system. This is a 2nd-order approximation because in this way, perceived distortion only depends on the interaction between the deviations in *pairs* of locations: $M(\mathbf{x}_A^0)_{ij} \Delta x_i^0 \Delta x_j^0$.

Note that a constant value for the distance in Eq. 23 defines an ellipsoid oriented and scaled according to the metric matrix $M(\mathbf{x}_A^0)$. In this 2nd-order approximation, the *discrimination regions* reduce to *discrimination ellipsoids*. The properties of these ellipsoids depend on the metric and hence on the Jacobian of the response w.r.t. the stimulus (i.e. on Result I below). In particular, the orientation depends on the eigenvectors of M and the scaling depends on the eigenvalues.

The simplicity of Eq. 23 depends on the assumption of quadratic norm in Eq. 22 (as opposed to other possible summation exponents in Minkowski metrics [29]). Note that using other norms would prevent writing the distance in the response domain through the dot product of $\Delta \mathbf{x}^n$. Therefore, the linear approximation would not be that easy. With non-quadratic summation the distance would still depend on the elements of the Jacobian (and hence on Result I), but the expression would be more complicated, and the reasoning through Jacobian-related eigenvectors would not be as intuitive.

2.2 Result I: Jacobian with regard to the stimulus

The problem of computing the Jacobian with regard to the stimulus in the cascade of L+NL modules, $\nabla_{\mathbf{x}_0} S$, reduces, according to Eqs. 17 and 18, to the computation of the Jacobian of the nonlinearity with regard to the stimulus in every layer, $\nabla_{\mathbf{y}^i} \mathcal{N}^{(i)}$. In this section we give the analytical result of the required Jacobian, $\nabla_{\mathbf{y}^i} \mathcal{N}^{(i)}$, in the canonical divisive normalization case, and for two alternative nonlinearities. Proofs of this first set of analytical results are given in the Supplementary Material 5.3. The role of this analytical result in generating stimuli for novel psychophysics is illustrated in the Discussion, Section 3.1.

Jacobian of the canonical nonlinearity with regard to the stimulus. The matrix form of the divisive normalization, Eq. 10, based on the diagonal matrix notation for the Hadamard products, is convenient to easily compute the Jacobian (see the explicit derivation in the Supplementary Material 5.3), which leads to,

$$\nabla_{\mathbf{y}^i} \mathcal{N}^{(i)} = \mathbb{D}_{\text{sign}(\mathbf{y}^i)} \cdot \mathbb{D}_{\mathcal{D}^{(i)}(\mathbf{e}^i)}^{-1} \cdot \left[\mathbb{1} - \mathbb{D}\left(\frac{\mathbf{e}^i}{\mathcal{D}^{(i)}(\mathbf{e}^i)}\right) \cdot H^i \right] \cdot \mathbb{D}_{(\gamma^i |\mathbf{y}^i|^{\gamma^i - 1})} \cdot \mathbb{D}_{\text{sign}(\mathbf{y}^i)} \quad (24)$$

Eq. 24 shows that the Jacobian, $\nabla_{\mathbf{y}^i} \mathcal{N}^{(i)}$, depends on the subtraction of two matrices, where the first one is *diagonal* and the second one depends on H^i , the matrix describing the interaction between the intermediate linear responses. Note that the role of the interaction is *subtractive*, i.e. it reduces the slope (for positive H^i). In situations where there is no interaction between the different coefficients of \mathbf{y}^i , $H_{kl}^i = 0 \ \forall k \neq l$, the resulting $\nabla_{\mathbf{y}^i} \mathcal{N}^{(i)}$ is point-dependent, but diagonal.

Eq. 24 also shows that the sign of the linear coefficients has to be considered *twice* (through the multiplication by the diagonal matrices at the left and right). This detail in the sign (which is crucial to set the direction in gradient descent), was not properly addressed in previous reports of this Jacobian (e.g. in [34, 35, 62]) because this literature was focused on properties which are independent of the sign (diagonal nature, effect on the metric, and determinant respectively).

Jacobian of alternative nonlinearities with regard to the stimulus. The forward Wilson-Cowan transform does not have an explicit expression since the solution evolves from a differential equation. As a result, there is no analytic solution of the Jacobian either. However its inverse is analytical (as detailed in the next section, Eq. 40). Therefore, given the relation between the Jacobian matrices of inverse functions, namely $\nabla_{\mathbf{y}^i} \mathcal{N}^{(i)} = \left(\nabla_{\mathbf{x}^i} \mathcal{N}^{(i)-1} \right)^{-1}$, we can compute the Jacobian of the *forward* Wilson-Cowan transform from the Jacobian of its inverse.

Specifically, derivation with regard to the response in the analytic inverse given in Eq. 40 is straightforward, and it leads to:

$$\nabla_{\mathbf{x}^i} \mathcal{N}^{(i)-1}(\mathbf{x}^i) = \frac{1}{\lambda} (\alpha \mathbb{1} - \mu W \cdot \mathbb{D}_{f'(\mathbf{x}^i)}) \quad (25)$$

As a result, the Jacobian of the *forward* Wilson-Cowan nonlinearities at the point \mathbf{y}_A^i is,

$$\nabla_{\mathbf{y}^i} \mathcal{N}^{(i)}(\mathbf{y}_A^i) = \left(\nabla_{\mathbf{x}^i} \mathcal{N}^{(i)-1}(\mathbf{x}_A^i) \right)^{-1} \quad (26)$$

assuming that $\nabla_{\mathbf{x}^i} \mathcal{N}^{(i)-1}$ is nonsingular at $\mathbf{x}_A^i = \mathcal{N}^{(i)}(\mathbf{y}_A^i)$. Note that, in general, this Jacobian matrix will be nondiagonal because of the inhibitory interactions between sensors expressed in the (nondiagonal) matrix W .

For the other example of alternative nonlinearity, the two-gamma saturation model, the Jacobian with regard to the stimulus is a diagonal matrix since this special nonlinearity is a point-wise operation. From Eq. 13, according to the derivation given in the Supplementary Material 5.3, the Jacobian of the two-gamma model is:

$$\nabla_{\mathbf{y}} \mathcal{N} = \mathbb{D}_{|\mathbf{y}|^{\gamma(|\mathbf{y}|)}} \cdot \left[\mathbb{D}_{\left((\gamma_H - \gamma_L) \cdot \frac{m |\mathbf{y}|^{(m-1)} \cdot \mu_1^m}{(\mu_1^m + |\mathbf{y}|^m)^2} \right)} \cdot \mathbb{D}_{\log |\mathbf{y}|} + \mathbb{D}_{\left(\frac{\gamma(|\mathbf{y}|)}{|\mathbf{y}|} \right)} \right] \quad (27)$$

Note that the logarithm and the division by $|\mathbf{y}|$ imply a singularity in zero. Then, in order to guarantee the differentiability of the nonlinear transform, we propose a modification of the nonlinearity in a small neighborhood of 0. By choosing an arbitrarily small, ϵ , so that $0 < \epsilon \ll 1$, we modify Eq. 13 for small inputs in this way,

$$\mathbf{x} = \begin{cases} \text{sign}(\mathbf{y}) \odot |\mathbf{y}|^{\gamma(|\mathbf{y}|)} & \text{if } |\mathbf{y}| \geq \epsilon \\ \text{sign}(\mathbf{y}) \odot (a_1 |\mathbf{y}|^2 + a_2 |\mathbf{y}|) & \text{if } |\mathbf{y}| \leq \epsilon \end{cases} \quad (28)$$

where,

$$a_1 = \frac{\epsilon \frac{\partial |\mathbf{y}|^{\gamma(|\mathbf{y}|)}}{\partial |\mathbf{y}|}(\epsilon) - \epsilon^{\gamma(\epsilon)}}{\epsilon^2} \quad \text{and} \quad a_2 = \frac{2\epsilon^{\gamma(\epsilon)} - \epsilon \frac{\partial |\mathbf{y}|^{\gamma(|\mathbf{y}|)}}{\partial |\mathbf{y}|}(\epsilon)}{\epsilon}$$

With this modification around zero the two-gamma nonlinearity and its derivative are continuous and well defined everywhere: the Jacobian for $|\mathbf{y}| > \epsilon$ would be given by Eq. 27, and for smaller inputs $\nabla_{\mathbf{y}} \mathcal{N} = 2a_1 |\mathbf{y}| + a_2$, which is well defined at zero.

2.3 Result II: Jacobian with regard to the parameters

The problem of computing the Jacobian with regard to the parameters in the cascade of L+NL modules, $\nabla_{\Theta} S$, reduces, according to Eqs. 19 - 21, to the computation of the Jacobian of the nonlinearity with regard to the parameters in every layer, $\nabla_{\theta^i} \mathcal{N}^{(i)}$. In this section we give the analytical result of the required Jacobian in the canonical divisive normalization case. Proofs of this second analytical result are given in the Supplementary Material 5.4. The role of this analytical result in getting optimal models from classical psychophysics is illustrated in the Discussion, Section 3.2.

Jacobian w.r.t. parameters: general equations The parameters of the divisive normalization of the i -th layer that may be independently modified are $\theta^i = \{\gamma^i, \mathbf{b}^i, H^i\}$. Therefore, $\nabla_{\theta^i} \mathcal{N}^{(i)}$ is given by this concatenation:

$$\nabla_{\theta^i} \mathcal{N}^{(i)} = \begin{bmatrix} \nabla_{\gamma^i} \mathcal{N}^{(i)} & \nabla_{\mathbf{b}^i} \mathcal{N}^{(i)} & \nabla_{H^i} \mathcal{N}^{(i)} \end{bmatrix} \quad (29)$$

where, according to the derivation given in the Supplementary Material 5.4, we have,

$$\nabla_{\gamma^i} \mathcal{N}^{(i)} = \mathbb{D}_{\text{sign}(\mathbf{y}^i)} \cdot \mathbb{D}_{\mathcal{D}^{(i)}(\mathbf{e}^i)}^{-1} \cdot \left[\mathbb{D}_{\log |\mathbf{y}^i|} - \mathbb{D}_{\mathcal{D}^{(i)}(\mathbf{e}^i)}^{-1} \cdot \mathbb{D}_{(H^i \cdot \mathbb{D}_{\mathbf{e}^i} \cdot \log |\mathbf{y}^i|)} \right] \cdot \mathbf{e}^i \quad (30)$$

$$\nabla_{\mathbf{b}^i} \mathcal{N}^{(i)} = -\mathbb{D}_{\text{sign}(\mathbf{y}^i)} \cdot \mathbb{D}_{\mathbf{e}^i} \cdot \mathbb{D}_{\mathcal{D}^{(i)}(\mathbf{e}^i)}^{-2} \quad (31)$$

$$\nabla_{H^i} \mathcal{N}^{(i)} = -\mathbb{D}_{\text{sign}(\mathbf{y}^i)} \cdot \mathbb{D}_{\mathbf{e}^i} \cdot \mathbb{D}_{\mathcal{D}^{(i)}(\mathbf{e}^i)}^{-2} \cdot \mathbb{B}_{(\mathbf{e}^i)^\top}^{d_i} \quad (32)$$

where $\mathbb{D}_{\mathbf{v}}$ stands for a diagonal matrix with vector \mathbf{v} in the diagonal as stated in Eq. 9, and $\mathbb{B}_{\mathbf{v}}^d$ stands for a block diagonal matrix built by d -times replication of the matrix (or vector) \mathbf{v} as stated in the Supplementary Material 5.2 (in Eqs. 67 and 68). Note also that, consistently with the derivative of a linear function w.r.t. its parameters (in Suppl. Material 5.2), in order to apply the Jacobian in Eq. 32 on small perturbations of the matrix, H^i , the corresponding perturbation should undergo row-wise vectorization. For instance, imagine H^i is perturbed so that $H_*^i = H^i + \Delta H$. Then, the perturbation in the response should be computed as $\Delta \mathbf{x}^i = \nabla_{H^i} \mathcal{N}^{(i)} \cdot \text{vect}(\Delta H^\top)$.

Jacobian w.r.t. parameters: specific equations for Gaussian kernels The qualitative meaning of H^i (interaction between neighboring neurons) naturally leads to propose specific structures in the rows of these matrices. For instance, stronger interaction between closer neurons naturally leads to the idea of Gaussian kernels [8]. This functional parametrization implies a dramatic reduction in the number of unknowns because each row, $H_{k\star}^i$, with dimension d_i , could be described by a Gaussian defined by with only two parameters: amplitude and width. In the considered retina-V1 pathway the identity of the sensors is characterized by its 2D spatial location or by its 4D spatio-frequency location. In the most general case the index, k , of the sensor has spatio-frequency meaning:

$$k \text{ denotes a wavelet-like index} \Rightarrow k \equiv (p_{k1}, p_{k2}, f_k, \phi_k)$$

where $\mathbf{p}_k = (p_{k1}, p_{k2})$ is the optimal 2D location, f_k is the optimal spatial frequency, and ϕ_k is the optimal orientation of the k -th sensor. In V1, the interaction between the linear response y_k^i and the neighbors $y_{k'}^i$ decreases with the distance between k and k' in space, frequency and orientation [8]. Restricting ourselves to intra-subband interactions (which incidentally are the most relevant [35, 62]) one has:

$$H_{kk'}^i = \begin{cases} 0 & \forall k' \notin \text{subband } k \\ c_k^i \frac{dp_{k1} dp_{k2}}{2\pi \sigma_k^{i2}} e^{-\frac{\Delta_{kk'}^2}{2\sigma_k^{i2}}} & \forall k' \in \text{subband } k \end{cases} \quad (33)$$

where the relevant parameters are c_k^i and σ_k^i which respectively stand for the amplitude and width of the Gaussian centered in the k -th sensor. $\Delta_{kk'}^2 = (\mathbf{p}_k - \mathbf{p}_{k'})^\top \cdot (\mathbf{p}_k - \mathbf{p}_{k'})$ is the squared distance between the sensors, and $dp_{k1} dp_{k2}$ is just the spatial area of the discrete grid of sensors that sample the visual space in this subband. This implies that the pool of all interactions is $\sum_{k'} H_{kk'}^i = c_k^i$.

In the case of different interactions per sensor (different Gaussian in each row, $H_{k\star}^i$), derivatives with regard to the independent widths are,

$$\nabla_{\sigma^i} \mathcal{N}^{(i)} = \left[\nabla_{\sigma_1^i} \mathcal{N}^{(i)} \quad \nabla_{\sigma_2^i} \mathcal{N}^{(i)} \quad \dots \quad \nabla_{\sigma_k^i} \mathcal{N}^{(i)} \quad \dots \quad \nabla_{\sigma_{d_i}^i} \mathcal{N}^{(i)} \right] \quad (34)$$

With this parametrization of H we can develop Eq. 32 further: the dependence on individual widths can be obtained by using $\nabla_{\sigma_k^i} \mathcal{N}^{(i)} = \nabla_{H^i} \mathcal{N}^{(i)} \cdot \nabla_{H_{k\star}^i} H^i \cdot \nabla_{\sigma_k^i} H_{k\star}^i$, and the final result (see the Supplementary Material 5.4) is:

$$\nabla_{\sigma^i} \mathcal{N}^{(i)} = -\text{diag} \left[\mathbb{D}_{\text{sign}(\mathbf{y}^i)} \cdot \mathbb{D}_{\mathbf{e}^i} \cdot \mathbb{D}_{\mathcal{D}^{(i)}(\mathbf{e}^i)}^{-2} \cdot \begin{pmatrix} \mathbf{e}^{i\top} \\ \mathbf{e}^{i\top} \\ \vdots \\ \mathbf{e}^{i\top} \end{pmatrix} \cdot \mathbf{F}^i \right] \quad (35)$$

where,

$$\mathbf{F}_{kk'}^i = \begin{cases} 0 & \forall k' \notin \text{subband } k \\ c_k^i \frac{dp_{k1} dp_{k2}}{2\pi \sigma_k^{i2}} \left(\Delta_{kk'}^2 - 2\sigma_k^{i2} \right) e^{-\frac{\Delta_{kk'}^2}{2\sigma_k^{i2}}} & \forall k' \in \text{subband } k \end{cases}$$

A diagonal matrix for $\nabla_{\sigma^i} \mathcal{N}^{(i)}$ makes sense because the modification of the interaction width of a sensor only affects the nonlinear response of this sensor (similarly to the diagonal nature of $\nabla_{\mathbf{b}^i} \mathcal{N}^{(i)}$ in Eq. 31).

The derivative with regard to the vector of amplitudes of the Gaussian interactions, $\nabla_{\mathbf{c}^i} \mathcal{N}^{(i)}$, is a concatenation of columns (similarly to Eq. 34). It can also be computed from the chain rule and from the derivative w.r.t the corresponding variables. The result is:

$$\nabla_{\mathbf{c}^i} \mathcal{N}^{(i)} = -\text{diag} \left[\mathbb{D}_{\text{sign}(\mathbf{y}^i)} \cdot \mathbb{D}_{\mathbf{e}^i} \cdot \mathbb{D}_{\mathcal{D}^{(i)}(\mathbf{e}^i)}^{-2} \cdot \begin{pmatrix} \mathbf{e}^{i\top} \\ \mathbf{e}^{i\top} \\ \vdots \\ \mathbf{e}^{i\top} \end{pmatrix} \cdot \mathbf{G}^i \right] \quad (36)$$

where,

$$G_{kk'}^i = \begin{cases} 0 & \forall k' \notin \text{subband } k \\ \frac{dp_{k1} dp_{k2}}{2\pi \sigma_k^{i2}} e^{-\frac{\Delta_{kk'}^2}{2 \sigma_k^{i2}}} & \forall k' \in \text{subband } k \end{cases}$$

The number of free parameters can be further reduced if one assumes that the values of the semisaturation, b_k^i , or the parameters of the Gaussians, c_k^i and σ_k^i , have certain structure (e.g. constant along the visual space in each subband). One may impose this structure in Eqs. 31, 35 and 36 by right-multiplication of the jacobian by a binary matrix that describes the structure of the considered vector. For instance, assuming the same width all over each scale in a two-scales image representation, one only has two independent parameters. In that case:

$$\nabla_{\sigma^i_{\text{struct}}} \mathcal{N}^{(i)} = \nabla_{\sigma^i} \mathcal{N}^{(i)} \cdot M_{\text{struct}}$$

where, the structure matrix selects which coefficients belong to each scale:

$$M_{\text{struct}} = \begin{pmatrix} 1 & 0 \\ 1 & 0 \\ \vdots & \vdots \\ 1 & 0 \\ 0 & 1 \\ 0 & 1 \\ \vdots & \vdots \\ 0 & 1 \end{pmatrix}$$

2.4 Result III: Analytic inverse

The inverse of the global transform can be obtained inverting each individual L+NL layer in turn,

$$S^{-1} = S^{(1)-1} \circ S^{(2)-1} \circ \dots \circ S^{(n-1)-1} \circ S^{(n)-1} \quad (37)$$

where,

$$\mathbf{x}^{i-1} = S^{(i)-1}(\mathbf{x}^i) = L^{i\dagger} \cdot \mathcal{N}^{(i)-1}(\mathbf{x}^i) \quad (38)$$

Here we will focus on the $\mathcal{N}^{(i)-1}$ part because the linear part can be addressed by standard matrix inversion.

Here we present the analytical inverse of the canonical divisive normalization and of the Wilson-Cowan alternative. The inverse of the two-gamma nonlinearity is not addressed here but in the Supplementary Material 5.1 because, given the coupling between the input and the exponent, it has no analytical inverse. Nevertheless, a simple and efficient iterative method is proposed there to compute the inverse. The role of the analytical inverse in improving conventional decoding of visual signals is illustrated in the Discussion, Section 3.3.

A note on the linear part: the eventual rectangular nature of L^i (different number of outputs than inputs in the i -th layer) requires standard pseudoinverse, $(\cdot)^\dagger$, instead of the regular square-matrix inversion, $(\cdot)^{-1}$; and it may be regularized through standard methods [86, 87] in case L^i is ill-conditioned. Information loss in the pseudoinverse due to strong dimensionality reduction in L^i is not serious in the central region of the visual field due to mild undersampling of the fovea throughout the neural pathway [88]. The only aspect of the input that definitely cannot be recovered from the responses is the spectral distribution in each location. In color perception models the first stage is linear spectral integration to give opponent tristimulus values in each spatial location [71]. This very first linear stage is represented by a extremely fat rectangular matrix, $L^1 \in \mathbb{R}^{3 \times 300}$, in each location (300 wavelengths in the spectral visible region reduce to 3 tristimulus values), which definitely is not invertible though standard regularized pseudoinversion. Therefore, the inversion of a standard *retina-V1* model such as the one used in the Discussion may recover the tristimulus images but not the whole hyperspectral array.

Analytic inverse of the Divisive Normalization. Analytic inversion of standard divisive normalization, Eq. 8, is not obvious. However, using the diagonal matrix notation for the Hadamard product, the inverse is (see Supplementary Material 5.5),

$$\mathbf{y}^i = \mathcal{N}^{(i)-1}(\mathbf{x}^i) = \mathbb{D}_{\text{sign}(\mathbf{x}^i)} \cdot \left[\left(\mathbb{1} - \mathbb{D}_{|\mathbf{x}^i|} \cdot H^i \right)^{-1} \cdot \mathbb{D}_{\mathbf{b}^i} \cdot |\mathbf{x}^i| \right]^{\frac{1}{\gamma^i}} \quad (39)$$

where $[v]^{\frac{1}{\gamma^i}}$ is element-wise exponentiation of elements of the vector v .

Consistently with generic inverse-through-integration approaches based on $\nabla_{\mathbf{x}} S^{-1}$ [89], here Eq. 39 shows more specifically that in this linear-nonlinear architecture, *inversion* reduces to *matrix inversion*. While the linear filtering operations, L^i , may be inverted without the need of an explicit matrix inversion through surrogate signal representations (deconvolution in the Fourier or Wavelet domains), there is no way to avoid the inverse $(\mathbb{1} - \varepsilon)^{-1}$ in Eq. 39. This may pose severe computational problems in high-dimensional situations (e.g. in redundant wavelet representations). A series expansion alternative for that matrix inversion was proposed in [34], where it is substituted by a (more affordable) series of matrix-on-vector operations.

Inverse of the Wilson-Cowan equations. The expression of the inverse of the Wilson-Cowan transform is straightforward: by reordering the terms in the steady-state equation, Eq. 12, it follows,

$$\mathbf{y}^i = N^{(i)-1}(\mathbf{x}^i) = \frac{1}{\lambda}(\alpha \mathbf{x}^i - \mu W \cdot f(\mathbf{x}^i)) \quad (40)$$

Note that this inverse function is easily derivable w.r.t \mathbf{x}^i , which is required to obtain the corresponding Jacobian of the *forward* transform Eq. 26.

Relation between Result I and Result III. Result III (inverse) is obviously related to Result I (Jacobian with regard to the stimulus) because a sufficient condition for invertibility is that the Jacobian with regard to the stimulus is nonsingular for every image. Note that if the Jacobian is non singular, the inverse of the Jacobian can be integrated and hence, the global inverse can be obtained from the local-linear approximations as in other *local-to-global* methods, e.g. [17, 20, 58, 89].

This general statement is perfectly illustrated by the similarity between Eqs. 39 and 24. According to Eq. 39, inverting the divisive normalization reduces to inverting the matrix $(\mathbb{1} - \mathbb{D}_{|\mathbf{x}^i|} \cdot H^i)$. Similarly, according to Eq. 24, the singularity of the Jacobian depends on the very same matrix.

3 Discussion

In this section we discuss how to apply the three results presented above in (i) stimulus design in novel psychophysics, (ii) model fitting in classical physiology and psychophysics, and (iii) decoding of visual signals.

The model used as illustration throughout the discussion follows the program suggested in [1]: a cascade of four isomorphic canonical Linear+Nonlinear modules addressing brightness, contrast, frequency filtered contrast masked in the spatial domain, and orientation/scale masking. Despite the general architecture is pretty standard, these specific modules have been psychophysically tuned to work jointly for the first time. The behavior of the model is illustrated in Fig. 1, the details of each Linear+Nonlinear module are given in the Supplementary Material 5.1, and the code is available in http://isp.uv.es/docs/BioMultiLayer_L_NL.zip.

The obtention of the specific parameters of the model makes extensive use of the results presented here. First, following [5], the layers 2nd and 3rd were determined using MAXimum Differentiation (MAD) psychophysics. This new psychophysical procedure relies on stimuli generated from the *Jacobian of the response with regard to the image* (i.e. MAD requires Result I). Then, the layers 1st and 4th were fitted to reproduce subjective image distortion. The conventional brute-force fits used in image distortion models [35, 39, 41, 62], are improved here by applying the *Jacobian of the response with regard to the parameters* for gradient descent. In other words, parameter fitting in classical psychophysics improves using Result II.

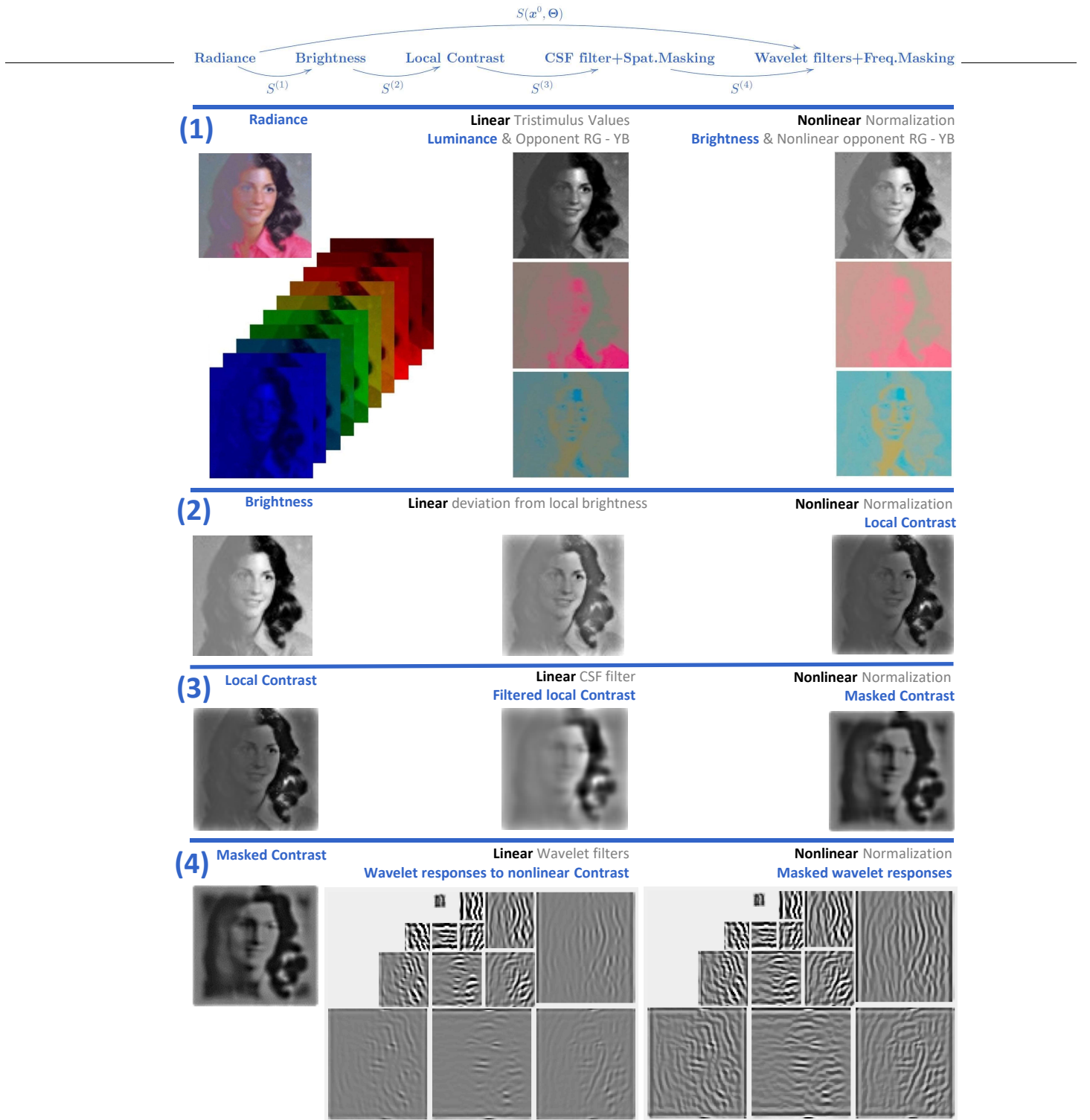


Fig 1. A cascade of isomorphic L+NL modules based on canonical Divisive Normalization. The input is the spatial distribution of the *spectral irradiance* at the retina. For this illustration we modified an image from the USC-SIPI Database [90] to reduce the contrast at the left part of the stimulus. (1) The linear part of the first layer consist of three positive LMS spectral sensitivities and a linear recombination of the LMS values with positive/negative weights. This leads to three tristimulus values in each spatial location: one of them is proportional to the luminance, and the other two have opponent chromatic meaning (red-green and yellow-blue). These linear tristimulus responses undergo adaptive saturation transforms. Perception of *brightness* is mediated by an adaptive Weber-like nonlinearity applied to the luminance at each location. This nonlinearity enhances the response in the regions with small linear input (low luminance). (2) The linear part of the second layer computes the deviation of the brightness at each location from the local brightness. Then, this deviation is nonlinearly normalized by the local brightness to give the local nonlinear contrast. (3) The responses to local contrast are convolved by center surround receptive fields (or filtered by the Contrast Sensitivity Function). Then the linearly filtered contrast is nonlinearly normalized by the local contrast. Again normalization increases the response in the regions with small input (low contrast). (4) After linear wavelet transform, each response is normalized by the activity of the neurons in the surround. Again, the activity relatively increases in the regions with low input. The common effect of the nonlinear modules throughout the network is response equalization. Supplementary Material 5.8 (Fig. 13) shows PDFs of the responses along the network which are consistent with previous reports of the predictive effect of Divisive Normalization.

Finally, the *analytical inversion of the nonlinear stages* (Result III), which is mandatory in perceptually inspired image compression [34], is compared here with conventional blind decoding techniques [54–56] used for visual brain decoding.

3.1 Jacobian with regard to the image in stimulus synthesis

Many times, stimuli design implies that the desired image should fulfill certain properties in the response domain. Examples include (i) *artistic style transfer* [91], in which the response to the synthesized image should be close to the response to the image from which the content is inherited, and should have a covariance structure close to the one in the response to the image from which style is inherited; and (ii) *Maximum Differentiation* [5, 22, 24], in which the synthesized images should have maximum/minimum perceptual distance with regard to a certain reference image with a constraint in the energy of the distortion. In both cases, fulfilling the requirements implies modifying the image so that the response is modified in certain direction. In such situations the Jacobian of the response with regard to the image (Result I) is critical.

Here we discuss in detail the case of MAXimum Differentiation (MAD). This technique is used to rank competing vision models by using them to solve a simple geometric question and visually assessing which one gave the better solution. While in conventional psychophysics the decision between two models relies on how well they fit thousands of individual measurements (either contrast incremental thresholds or subjective ratings of distortions), in MAD the decision between two models reduces to a single visual experiment.

The geometric question for the perception model in MAD is the following [22]: given a certain reference image, \mathbf{x}_A^0 , and the set of distorted images departing a certain amount of energy from the reference image, the sphere with center in \mathbf{x}_A^0 and certain fixed radius (or certain Mean Squared Error); the problem is looking for the images with maximum and minimum perceptual distance on the sphere, let's call them \mathbf{x}_{\min}^0 and \mathbf{x}_{\max}^0 . If the vision model is meaningful, \mathbf{x}_{\min}^0 and \mathbf{x}_{\max}^0 should have a very different visual appearance. The more accurate vision model will be the one leading to the pair of images which are maximally different. The discriminative power of this visual experiment comes from the fact that the synthesis of these stimuli involves comparing the performance of the models under consideration in every possible direction of the space of images.

Fig. 2(a) illustrates the geometric problem in MAD. The following paragraphs show how the different solutions to this geometric problem reduce to the use of Result I.

General, but numeric, solution to MAD. In general there is no analytical solution for such problem and hence one has to start from a guess image and modify it according to the direction of the gradient of the perceptual distance, $\nabla_{\mathbf{x}^0} d_p$, to maximize or minimize this distance. Of course, the problem, illustrated in Fig. 2(b), is that, a naive modification of the m -th guess, $\mathbf{x}_{[m]}^0$, in the direction of this gradient puts the solution out of the sphere: note the location of $\mathbf{x}_{\text{naive}}^0$ in pink, in Fig. 2(b). As proposed in [22], this departure from the sphere is solved by (i) subtracting the component parallel to the gradient of the Euclidean distance, $\nabla_{\mathbf{x}^0} d_1$ (see the point $\mathbf{x}_{\text{naive}'}^0$ in red), and (ii) projecting this displaced point back into the sphere (see the point $\mathbf{x}_{[m+1]}^0$ in orange). In summary, the complete iteration for the stimulus that maximizes/minimizes the distance is as follows [22]:

$$\mathbf{x}_{[m+1]}^0 = \mathbf{x}_{[m]}^0 \pm \lambda \left(\nabla_{\mathbf{x}^0} d_p - \frac{\nabla_{\mathbf{x}^0} d_1 \cdot \nabla_{\mathbf{x}^0} d_p^\top}{\nabla_{\mathbf{x}^0} d_1 \cdot \nabla_{\mathbf{x}^0} d_1^\top} \nabla_{\mathbf{x}^0} d_1 \right)^\top + \nu \nabla_{\mathbf{x}^0} d_1'^\top \quad (41)$$

where, λ is the constant that controls the convergence of the gradient descent, and ν can be computed analytically since the Euclidean distance of the point projected onto the sphere should be $|\mathbf{x}_{\text{naive}'}^0 + \nu \nabla_{\mathbf{x}^0} d_1'^\top - \mathbf{x}_A^0|^2 = r^2$, where, given the gradients, the only unknown is ν . Note that the gradients of the distances are *row vectors* since they should be applied on the column vectors describing the increments in the images: $\Delta d = \nabla_{\mathbf{x}^0} d \cdot \Delta \mathbf{x}^0$ (row vector times column vector). That is why we need to transpose the gradients before adding the modifications to $\mathbf{x}_{[m]}^0$, and the reason for the transposes in the scalar products of gradients (as in the projection $\nabla_{\mathbf{x}^0} d_1 \cdot \nabla_{\mathbf{x}^0} d_1^\top$, row vector times column vector). Note also that the

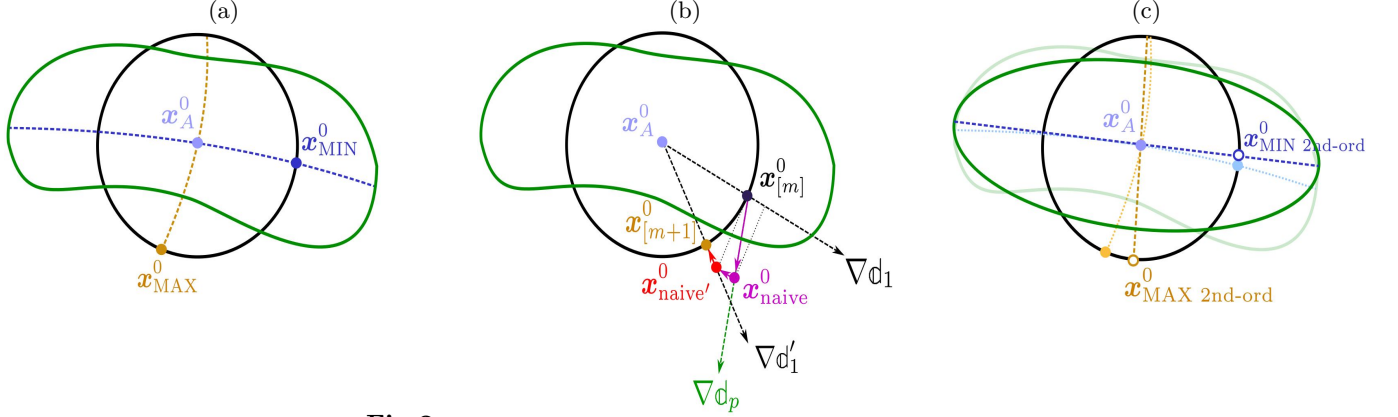


Fig 2. Stimulus generation in MAXimum Differentiation (MAD). (a) The MAD concept: given an original image, e.g. the point \mathbf{x}_A^0 in light blue, a perceptual distance measure, d_p , coming from a vision model (leading to the discrimination region in green), and certain fixed Euclidean distance, d_1 , (sphere in black); the problem is looking for the best and worst images on the sphere according to the perceptual distance d_p . The solution is given by the images that are in the directions (or paths) leading to the biggest or the lowest perceptual distortions (\mathbf{x}_{MAX}^0 and \mathbf{x}_{MIN}^0 , in dark blue and orange respectively). In the example, the path leading to the biggest perceptual difference (for the same Euclidean length) is the curve in orange because it represents the shortest path from the original image to the discrimination boundary in green. Equivalently, the path leading to the lowest perceptual difference (for the same Euclidean length) is the curve in blue because it represents the longest path to the discrimination boundary in green. (b) The MAD algorithm: start from a random point at the sphere and modify it to increase (or alternatively decrease) the perceptual distance following ∇d_p . Note that the naive application of the gradient implies a solution out of the sphere. This has to be projected on the sphere through the appropriate correction: first remove the component parallel to ∇d_1 , and then project in the direction of $\nabla d'_1$. (c) Second order approximation: approximate the perceptual discrimination regions by ellipsoids (local linear approximation of the vision model). In this way the MAD images are given by the directions of the maximum and minimum eigenvalue of the 2nd order metric matrix.

gradients without prime are computed at $\mathbf{x}_{[m]}^0$, and the gradient with prime is computed at $\mathbf{x}_{naive'}^0 = \mathbf{x}_{[m]}^0 \pm \lambda \left(\nabla_{\mathbf{x}^0} d_p^\top - \frac{\nabla_{\mathbf{x}^0} d_1 \cdot \nabla_{\mathbf{x}^0} d_p^\top}{\nabla_{\mathbf{x}^0} d_1 \cdot \nabla_{\mathbf{x}^0} d_1} \nabla_{\mathbf{x}^0} d_1^\top \right)$.

Now, let's address the gradients. The Euclidean distance with regard to the reference image evaluated at certain \mathbf{x}_B^0 is $d_1(\mathbf{x}_B^0) = \left((\mathbf{x}_B^0 - \mathbf{x}_A^0)^\top \cdot (\mathbf{x}_B^0 - \mathbf{x}_A^0) \right)^{1/2}$. Therefore, the gradient of the Euclidean distance with regard to \mathbf{x}_B^0 is:

$$\nabla_{\mathbf{x}_B^0} d_1(\mathbf{x}_B^0) = \frac{\partial \left(d_1(\mathbf{x}_B^0)^2 \right)^{1/2}}{\partial d_1(\mathbf{x}_B^0)^2} \cdot \frac{\partial d_1(\mathbf{x}_B^0)^2}{\partial (\mathbf{x}_B^0 - \mathbf{x}_A^0)} \cdot \frac{\partial (\mathbf{x}_B^0 - \mathbf{x}_A^0)}{\partial \mathbf{x}_B^0} = \frac{1}{d_1(\mathbf{x}_B^0)} (\mathbf{x}_B^0 - \mathbf{x}_A^0)^\top \cdot \mathbb{1}$$

More interestingly (since this was not addressed in [22]), the gradient of the perceptual distance in the cascaded setting considered here, which is defined at the response domain, Eq. 22, is,

$$\nabla_{\mathbf{x}_B^0} d_p(\mathbf{x}_B^0) = \frac{\partial \left(d_p(\mathbf{x}_B^0)^2 \right)^{1/2}}{\partial d_p(\mathbf{x}_B^0)^2} \cdot \frac{\partial d_p(\mathbf{x}_B^0)^2}{\partial (\mathbf{x}_B^n - \mathbf{x}_A^n)} \cdot \frac{\partial (\mathbf{x}_B^n - \mathbf{x}_A^n)}{\partial \mathbf{x}_B^0} = \frac{1}{d_p(\mathbf{x}_A^0, \mathbf{x}_B^0)} (\mathbf{x}_B^n - \mathbf{x}_A^n)^\top \cdot \nabla_{\mathbf{x}^0} S(\mathbf{x}_B^0) \quad (42)$$

which depends on the responses for the considered images, $\mathbf{x}^n = S(\mathbf{x}^0)$, and on the Jacobian of the response with regard to the input $\nabla_{\mathbf{x}^0} S(\mathbf{x}_B^0)$.

Eq. 42 together with the auxiliary results on $\nabla_{\mathbf{x}^0} S$ (Eqs. 17 and 18) imply that the application of MAD in the cascaded setting considered here, reduces to the use of Result I, i.e. Eq. 24 for the canonical nonlinearity, or the equivalent equations for the alternative nonlinearities considered (i.e. Eqs. 26 and 27).

Analytic, but approximated, solution to MAD. As stated in Section 2.1 when talking about the distance, Eq. 23, in the local-linear approximation the general discrimination regions are approximated by ellipsoids. In the illustration of Fig. 2, the (general) curved region in dark green in Figs. 2.a and 2.b is approximated by the ellipsoid in Fig. 2.c.

Under this approximation, the minimization/maximization of the perceptual distance on the Euclidean sphere has a clear analytic solution: the images with maximum and minimum

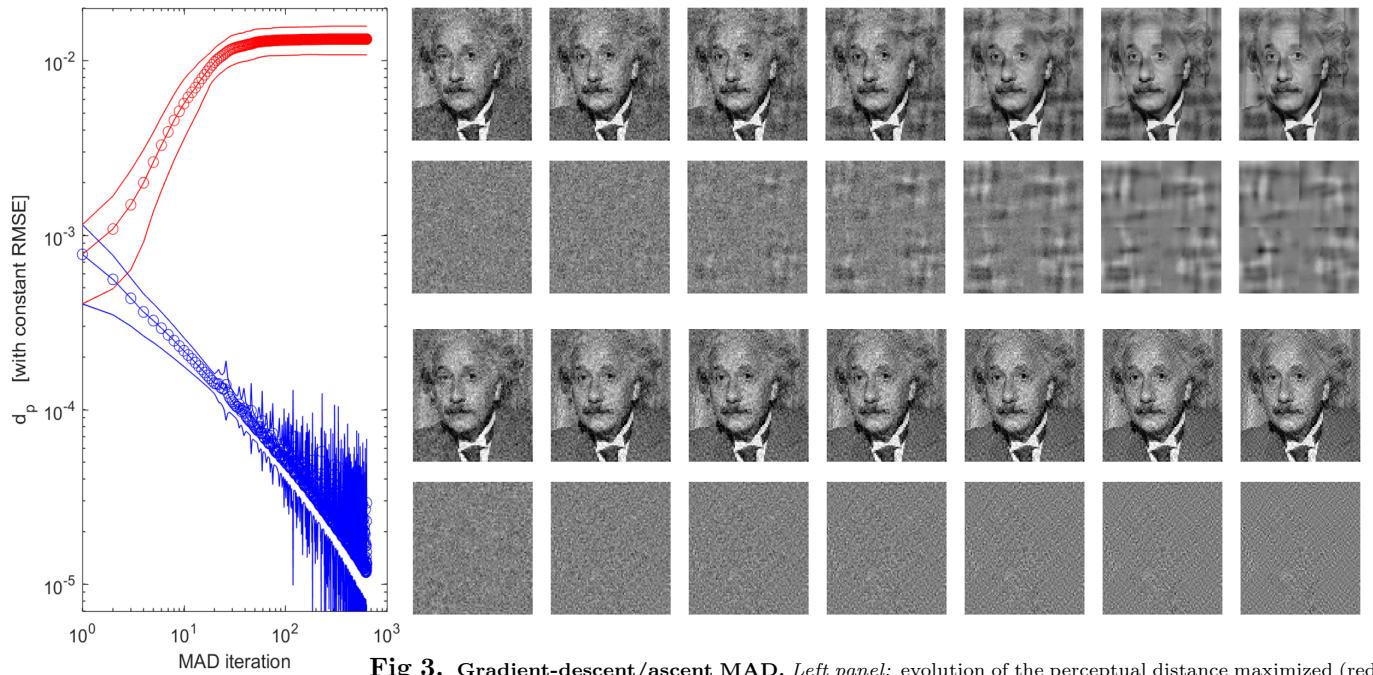


Fig 3. Gradient-descent/ascent MAD. *Left panel:* evolution of the perceptual distance maximized (red curve) or minimized (blue curve) from an initial white-noise distorted image. *Right panel (from left-to-right):* evolution of the intermediate MAD images on the sphere of constant MSE. The rows at the top show the evolution of progressively-worse images while maximizing the perceptual distance. The rows at the bottom show the equivalent evolution of the progressively-better images while minimizing the perceptual distance.

perceptual distance will be those in the directions of the eigenvectors with minimum and maximum eigenvalues of the metric matrix $M(\mathbf{x}_A^0)$. These, again, depend on the Jacobian of the response with regard to the stimulus, and hence on Result I.

The view of the MAD problem in terms of a metric matrix is also useful when breaking large images into smaller patches for computational convenience. In these patch-wise scenarios the global metric matrix actually has block-diagonal structure (see the Supplementary Material 5.6). Therefore, given the properties of block-diagonal matrices [87], the global eigenvectors (and hence the solution to MAD) actually reduce to the computation of the eigenvectors of the smaller metric matrices for each patch.

Illustration of the general and the analytic solutions. In this illustration we take a reference image and we launch a gradient descent/ascent search in the sphere of constant RMSE to look for the best/worst version of this image.

For the same image we compute the Jacobian with regard to the stimulus and we compute the eigenvectors of bigger and lower eigenvalue, i.e. the directions that lead to most/least visible distortions in the 2nd order approximation of the distance (approximated analytic MAD solution). For computational convenience we take a patch-wise approach considering distinct regions subtending 0.65 deg. This region-oriented approach certainly generates some artifacts in the block boundaries. However, the moderate visual impact of these edge effects suggests that for regions of this size (and above) it is fair to assume the block-wise independence of distortion. See additional comments on this computationally convenient assumption in Supplementary Material 5.6.

Fig. 3 shows the evolution of the general MAD distances and the solutions from the initial guess on the sphere (image corrupted with white-noise). Monotonic increase and decrease in the red and blue distance curves and progressive degradation or improvement in the images indicate both (a) the correctness of Result I, and (b) the accuracy of the parameters of the model used in this illustration.

Figures 4 and 5 show the results of the general MAD search and its analytic approximation respectively.

The main trend is this: the numerical procedure leads to noises of similar visual nature than the analytic procedure. This means that the iterative search is certainly attracted to the

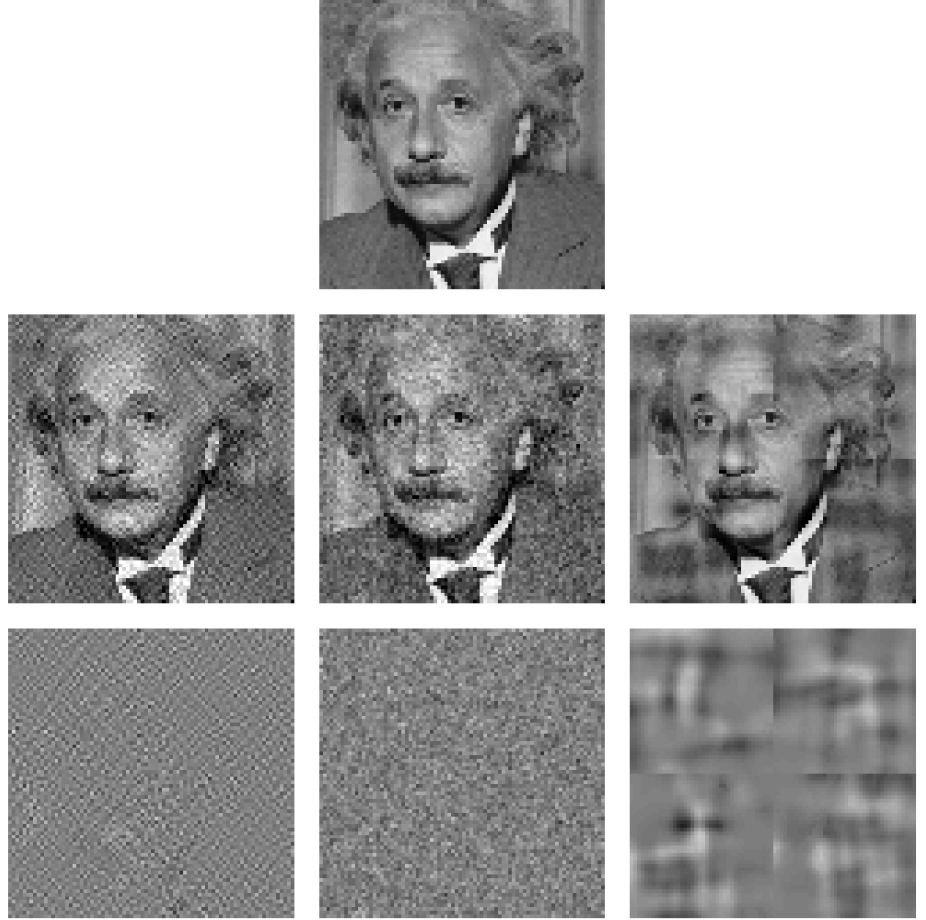


Fig 4. General numeric solution. *Top:* original image for comparison purposes. *Central row:* extreme images (perceptually best and worst -left and right-) for the same RMSE than the white-noise corrupted image at the center. Extreme images were computed using the gradient descent/ascent described in Eq. 41 (that requires Result I). The fact that these extreme images are actually better and worse than the central image indicates that the theory works. *Bottom row:* isolated distortions of the same energy added on top of the original image.

subspaces with low and high eigenvalues of the 2nd order metric. More specifically, in both cases (a) the algorithms tend to allocate high-contrast low-frequency artifacts in low-contrast regions (jacket and background) to increase the visibility of the noise, and (b) the algorithms tend to allocate high-frequency noise in high-contrast regions (e.g. the tie) to minimize its visibility.

There are differences between the general and the analytic solutions. In this example the visual difference between the pairs of the analytic (approximated) solution seems bigger than the visual difference between the general (numeric) solution. In principle, the numeric solution follows more closely the actual geometry induced by the perception model (amorphous discrimination region versus approximated ellipsoid). However, the finite length of the gradient descent search and the eventual trapping in local minima may prevent the practical use of the general technique (not to speak about the substantially higher computational cost of the search!).

Nevertheless, the qualitative similarities of the solutions (the nature of the distortions and its spatial location) is more relevant than the small quantitative differences. In the model considered throughout this Discussion (Fig. 1), the 2nd and 3rd layers (contrast, and energy masking) were determined using analytic MAD as in [5]. The experimental determination consisted of deciding between different distorted pairs corresponding to eigenvectors coming from models from different parameters. The final values found are those referred in the associated code (see Supplementary Materials 5.1 and 5.8). Interestingly, MAD images in this paper (Figs.

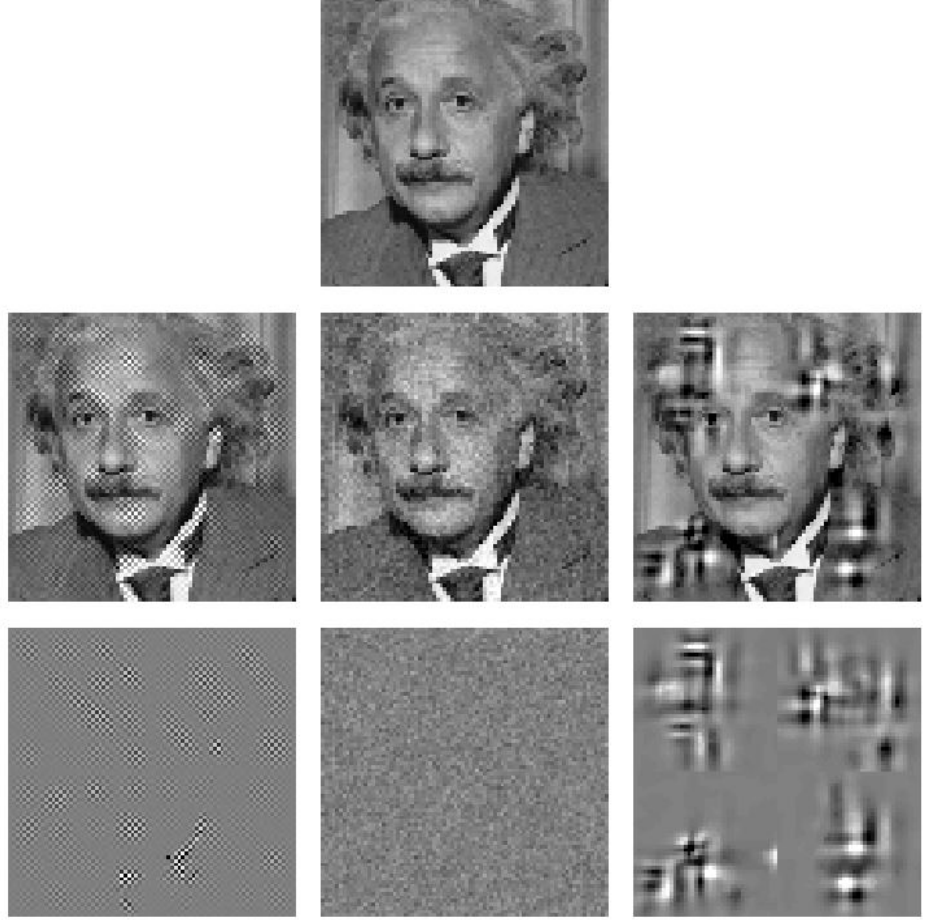


Fig 5. Analytic, but approximated, solution. *Top:* original image for comparison purposes. *Central row:* extreme images (perceptually best and worst -left and right-) for the same RMSE than the white-noise corrupted image at the center. Extreme images are built from the eigenvectors of the Jacobian dependent metric matrix, $M(\mathbf{x}_A^0) = \nabla_x S(\mathbf{x}_A^0)^\top \cdot \nabla_x S(\mathbf{x}_A^0)$ (hence requiring Result I). The fact that these extreme images are actually better and worse than the central image indicates that the theory works. *Bottom row:* isolated distortions of the same energy added on top of the original image.

3-5, and Fig. 15 in the demo of the Toolbox) were computed using two extra layers in the model (1st and 4th, accounting for brightness and wavelet masking respectively). The important point is that, either numeric or analytic MAD images, they give rise to distinct pairs by putting wavelet-like localized distortions of the right frequency in the regions with the right contrast or luminance.

Recently proposed visualization techniques to assess the biological plausibility of deep-network architectures [25] reduce to our analytic-MAD result originally proposed in [5]. The relevance of Result II is that it makes explicit the Jacobian expressions which are hidden in automatic differentiation techniques used in [25]. Incidentally, visual judgement of our distorted images and those presented in [25] suggests that the perceptual quality of our model is better since worse-case images are more annoying in our case than in the cases presented there.

3.2 Jacobian with regard to the parameters in model optimization

The standard methodology to set the free parameters of a model is looking for the values that better reproduce experimental results (either direct physiological recordings or indirect psychophysical results). Sometimes brute-force exhaustive search (as done in [35, 39–41]) is good enough given the low dimensionality of the parameter space. However, when considering thousands of parameters (as may happen in the considered model), brute-force approaches

are definitely unfeasible. In this high-dimensional scenario the Jacobian with regard to the model parameters (i.e. Result II) may be very convenient to look for the optimal solution, as for instance using gradient descent.

Interestingly, model fitting procedures based on alternative goals (as for instance optimal encoding/decoding performance, as in [42]) also depend on gradient descent and this Jacobian w.r.t. parameters. Unfortunately, the use of this Jacobian in similar biological models for optimal encoding/decoding (in [42]) or to reproduce psychophysical data (in [25]), was hidden behind automatic differentiation. On the contrary, here we gave the explicit equations (Result II) and show their practical performance and correctness in analyzing psychophysical data.

In this section we discuss how to use the presented Result II (generic Eqs. 19-21 and specific equations for the Divisive Normalization, Eqs. 29-36), to obtain the model parameters from classical subjective image quality ratings.

Reproducing direct input-output data. In a controlled input-output situation (as in [40]), you may have a set of experimental physiological responses, $\mathbf{x}_{\text{exp}}^n$, for a given set of known input stimuli, $\mathbf{x}_{\text{exp}}^0$, and the goal is finding the model that behaves like the recorded data.

A popular cost function depending on the parameters is the quadratic norm of the deviation between the theoretical and the experimental responses $\varepsilon(\Theta) = \|\mathbf{x}_{\text{exp}}^n - S(\mathbf{x}_{\text{exp}}^0, \Theta)\|_2^2$. Minimization of this deviation, requires the derivative of the cost with regard to the parameters,

$$\frac{\partial \varepsilon(\Theta)}{\partial \Theta} = 2 (\mathbf{x}_{\text{exp}}^n - S(\mathbf{x}_{\text{exp}}^0, \Theta))^\top \cdot \nabla_{\Theta} S(\mathbf{x}_{\text{exp}}^0, \Theta) \quad (43)$$

which of course depends on the Jacobian w.r.t the parameters (and hence on Result II).

Reproducing indirect data. By indirect data we refer to certain behavior that is mediated by the responses of the underlying L+NL mechanisms, but it is different from the actual responses themselves. This is the conventional situation in psychophysics. An illustrative example is the subjective assessment of perceived differences in image quality databases.

In this particular image quality situation instead of having a set of physiological responses for a given input, we have a Mean Opinion Score (MOS) of a set of distorted images (which is the usual ground truth in the image quality literature [92]), and we want to adjust our model to reproduce this opinion.

In this case, the goal function is the correlation between the experimental subjective distance and the perceptual distance computed using the model explained above. More specifically, consider a set of N corrupted images, $\mathbf{z}_{[c]}^0 = \mathbf{x}_{[c]}^0 + \Delta \mathbf{x}_{[c]}^0$, with $c = 1 \dots N$. For this set, we assume we know the N mean opinion scores, $\mathbf{M} = (m^{[1]}, \dots, m^{[N]})^\top$, and we can compute the N perceptual distortions, $\mathbf{D} = (d_p^{[1]}, \dots, d_p^{[N]})^\top$, using the model (e.g. using Eq. 22).

Therefore, the optimal parameters will be those maximizing the alignment between the ground truth, \mathbf{M} and the model predictions \mathbf{D} . Using the Pearson correlation, ϱ , as alignment measure, we have,

$$\Theta^* = \max_{\Theta} \varrho(\Theta) = \max_{\Theta} \frac{\mathbf{M}_s^T \cdot \mathbf{D}_s(\Theta)}{|\mathbf{M}_s| |\mathbf{D}_s(\Theta)|} \quad (44)$$

where subindex s stands for subtraction of the mean of the vectors.

The maximization of the correlation, ϱ , requires its derivative with regard to the parameters of the model. Interestingly (see the Supplementary Material 5.7), it turns out that the derivative of this goal function also depends on $\nabla_{\Theta} S$ (i.e. it depends on Result II):

$$\frac{\partial \varrho}{\partial \Theta} = \left(\frac{\mathbf{M}_s^T}{|\mathbf{M}_s| \cdot |\mathbf{D}_s|} - \frac{\mathbf{M}_s^T \mathbf{D}_s}{|\mathbf{M}_s| \cdot |\mathbf{D}_s|^3} \cdot \mathbf{D}_s^T \right) \cdot \left(\mathbf{1} - \frac{1}{N} \cdot \mathbf{1} \right) \cdot \begin{bmatrix} \frac{\Delta \mathbf{x}_{[1]}^n{}^\top}{|\Delta \mathbf{x}_{[1]}^n|} \cdot [\nabla_{\Theta} S(\mathbf{z}_{[1]}^0) - \nabla_{\Theta} S(\mathbf{x}_{[1]}^0)] \\ \frac{\Delta \mathbf{x}_{[2]}^n{}^\top}{|\Delta \mathbf{x}_{[2]}^n|} \cdot [\nabla_{\Theta} S(\mathbf{z}_{[2]}^0) - \nabla_{\Theta} S(\mathbf{x}_{[2]}^0)] \\ \vdots \\ \frac{\Delta \mathbf{x}_{[N]}^n{}^\top}{|\Delta \mathbf{x}_{[N]}^n|} \cdot [\nabla_{\Theta} S(\mathbf{z}_{[N]}^0) - \nabla_{\Theta} S(\mathbf{x}_{[N]}^0)] \end{bmatrix} \quad (45)$$

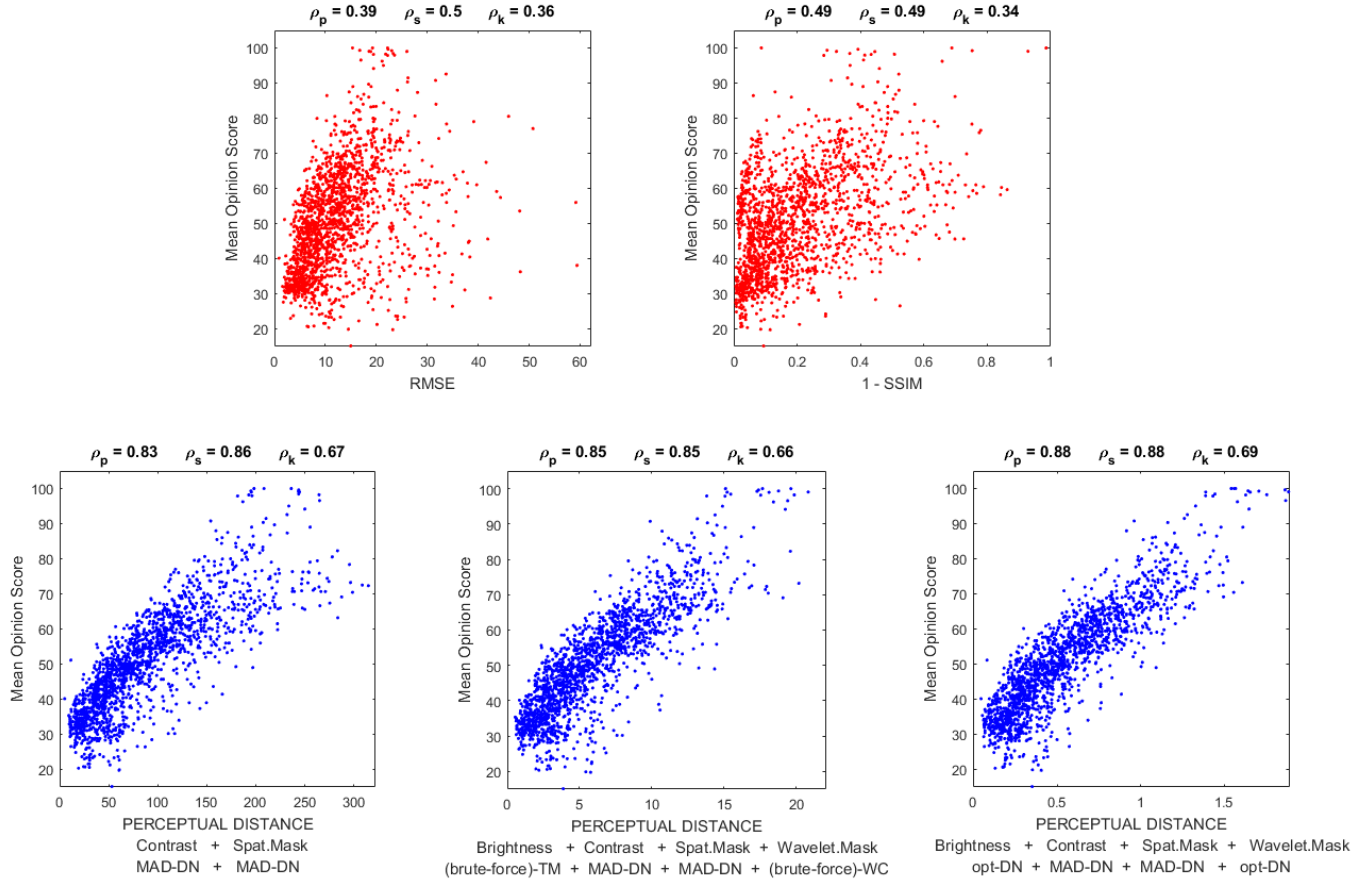


Fig 6. Prediction of subjective distortion. Correlation between predicted subjective distortion (in abscissas) and actual opinion (in ordinates) is a good performance measure of models in a variety of observation conditions. These results show the Pearson, Spearman and Kendall correlations of different models in reproducing the MOS values of the TID database [93]. Results show: (1) the quality of the baseline 2-stage model determined using MAD that accounts for contrast, frequency filtering and masking in the spatial domain [5]; (2) improvements in the performance due to the consideration of extra L+NL modules that account for brightness and masking in the wavelet domain, e.g. the two-gamma tone-mapping (TM) transform, and the Wilson-Cowan (WC) interaction between linear wavelet responses [41]; and (3) brute-force approaches can be improved through the appropriate search based on the Jacobian of the response w.r.t the parameters. Results in red (Euclidean distance, RMSE; and a widely used model of perceptual distortion, SSIM) have been included for convenient reference.

Cascaded L+NL model in image quality. The reproduction of image quality ratings is a good way to check the performance of vision models in a variety of observation conditions (variety of natural backgrounds and variety of suprathreshold tests).

The image quality results discussed in this section illustrate three interesting issues:

- They are a complementary evidence of the quality of the modular model (different from MAD results of the previous section).
- They point out the benefits of the modular nature of the model since inclusion of extra layers leads to consistent improvements of the performance (either by using canonical L+NL layers or by using alternative formulations such as the two-gamma tone mapping model or the Wilson-Cowan nonlinearity after a linear wavelet stage).
- They reveal the relevance of Result II in finding the model parameters in high-dimensional scenarios and the correctness of the presented expressions.

Figure 6 shows the performance of the kind of cascaded L+NL models we are considering here in the reproduction of mean opinion scores. We include two reference models (in red) for convenient comparison. The first reference is just the Euclidean distance between inputs (RMSE). The second reference is the most popular perceptual quality predictor in the image processing community (the Structural Similarity index, SSIM [94]). Our base-line model is the 2-stage L+NL model whose parameters were tuned using Maximum Differentiation [5]. Results reported here are better than those reported in [5] (using the same parameters) probably because of two reasons: (1) here we are using bigger patches and hence the patch-independence

assumption holds better, and (2) we are now applying luminance calibration to digital values of the TID database. This base-line model corresponds to the 2nd and 3rd canonical stages of the global model we are considering throughout the discussion section (see model details in the Supplementary Material 5.1).

Substantial jumps in correlation from the RMSE result indicate the well-known limitation of naive Euclidean distance [45] but also the potential of MAD to set the parameters of this 2-stage model [5]. Note that, assuming the Contrast Sensitivity Function (CSF) of the Standard Spatial Observer [39], this 2-stage model only has 5 free parameters (something affordable using MAD): the widths of the kernels and the semisaturation for contrast computation, and the width of the kernel, the semisaturation, and the excitation exponent in the masking nonlinearity.

Modularity and interpretability of the model is nice because it allows to propose straightforward improvements of the baseline model: just introduce extra layers according to the program suggested in [1]. We included extra layers before and after the two canonical layers in the base-line model: a brightness perception model before the contrast computation layer, and a wavelet interaction model after the CSF+spatial masking stage. To stress the generality of the proposed modular approach our first brightness model was the two-gamma tone mapping operator cited in Section 2.1, and our first wavelet masking scheme was the Wilson-Cowan model cited in Section 2.1 applied to each subband of a steerable pyramid. Following [41] the 5 extra parameters of these extra layers were obtained through brute-force search and the resulting model not only improves the correlation in image quality (as expected by construction), but it also has sensible behavior in reproducing contrast masking [41].

Finally, we explicitly explored the maximization of the correlation using different versions of the brightness and the wavelet+masking stages. In this final case we used canonical Divisive Normalization layers. Note that the joint optimization of the 1st and 4th layers is an interesting way to check Results I and II at once. First, relation to the Jacobian w.r.t the parameters in Result II is obvious from Eq. 45. But, more interestingly, note that the chain rule, Eq. 20, implies that distortions due to variations in the parameters propagate throughout the network. Then, the Jacobian w.r.t the stimulus (i.e. Result I of all the layers following the one under optimization) is also required in the joint optimization of 1st and 4th layers.

As a result of the chain rule, this optimization has a great experimental value but also a great computational cost. That is why we split the optimization of this illustration in two separate phases.

In the optimization *phase one* we addressed the (highly illustrative but extremely demanding) joint optimization of the 1st and 4th stages. In this *phase one* we used a reduced training set to avoid the computational burden, and we used structured versions of the parameters as discussed after Eq. 36 to address a relatively low-dimensional problem (but still not affordable through brute force). Then, in *phase two*, we took the results of *phase one* (which are only a first approximation to the right solution because of the small size of the training set) and focused on the optimization of a single parameter which is fast to compute but extremely high-dimensional to point out even more clearly the necessity of using Result II. Positive results of these first and second learning phases are illustrated in Fig. 7.

Computational cost of joint optimization (*phase one*) implies that not that many training points can be used in the gradient ascent. This implies that in order to generalize the training set has to be stochastically updated. We show the result of such stochastic maximization of the correlation using only 48 samples of the TID database at a time. The gradient ascent search in *phase one* (blue curve at the left) certainly increases the correlation for the considered small training set. Note that oscillations come from the random modification of the training set in each iteration. The consistent increase of correlation in the stochastic *phase one* points out the correctness of Results I and II. However, in the explored iterations in *phase one*, the correlation in the whole dataset only increased up to 0.84. This generalization problem means that the training set is too small to avoid overfitting or equivalently, that extra iterations would be necessary so that this small set could visit the whole variability in the dataset.

Once Result II (and also Result I) have been checked in the most demanding situation (joint optimization of two layers in *phase one*), we switch to *phase two*. In the *phase two* only the semisaturation of the 4th stage (only the vector \mathbf{b}^4) was optimized. Note that in this restricted case we do not need the Result I of the intermediate stages anymore. In fact, the computation of the Jacobian w.r.t. this single parameter is so fast that we allowed the

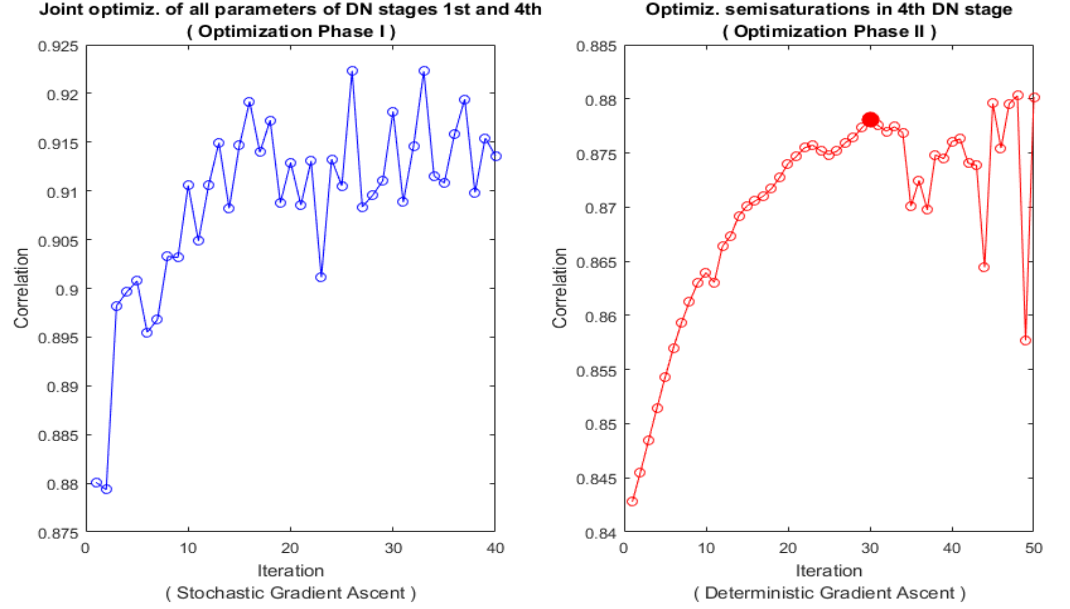


Fig 7. Maximization of correlation with subjective opinion (phase one and phase two). *Phase one* (left) involved the joint optimization of the following parameters: β, γ of the 1st stage and b, σ, γ, c of the 4th stage. In this case $\beta_1, \gamma_1, \gamma_4 \in \mathbb{R}^1$ and $\beta_4, \sigma_4, c_4 \in \mathbb{R}^{14}$ one parameter per orientation (with 4 orientation) and scale (with 4 scales) plus both residuals. Note that even though the relatively small number of parameters, the dimensionality is still huge to allow a brute force approach. Given the computational cost of *phase one* we used stochastic gradient descent on a extremely small training set. Results shown in the curve correspond to the randomly varying training set. In *phase one* the correlation for the whole database only arrives up to 0.84 because more iteration would be required. *Phase two* (right) only involved the optimization of b^4 . This is fast enough to use deterministic gradient ascent training with half the database. However, note that if no structure is imposed in b^4 , it has thousands of elements thus brute-force is not possible. In this case, correlation results shown correspond to the whole database (indicating proper generalization). The parameters leading to the maximum correlation in the test set (peak of the red curve) are those used for the scatter plot of Fig.6.

search in the full dimensionality of this vector and using deterministic gradient ascent (using a substantial part of the available database). In particular in this *phase two* we trained with 800 randomly chosen points of the database, as opposed to the randomly varying 48 points of *phase one*. In this high-dimensional case (note the full dimension of b^4) brute-force is not possible, and hence the gradient ascent (i.e. Result II) is the most sensible way. In this *phase two*, the correlation on the whole database consistently increases at the beginning of the search indicating both the correctness of Result II (for this parameter) and the fact that the training set is certainly representative. Finally, as expected in any learning problem using a limited training set, overfitting occurs and the correlation for the test set starts to oscillate. The values found at the (trustable) highlighted point are those used in the final scatter plot of Fig. 6.

3.3 Analytic inverse in visual brain decoding

Visual brain decoding refers to the reconstruction of the input stimulus from physiological recordings of the neural activity (for instance fMRI) [54]. Conventional decoding techniques are based on *learning-through-examples* the response-stimulus relation. First approaches to decoding used plain linear regression [59], but now the current practice is using non-linear regression as for instance based on kernel methods (as in [56,95]). However, given the fact that models of the BOLD signal also have this cascaded L+NL structure [40], the analytic inverse of the transform proposed here (Result III) may have obvious application in decoding the input from the recorded output.

In order to illustrate the eventual benefits of the analytic inverse in the visual decoding problem, in this discussion we consider a simulation were conventional blind machine-learning techniques (linear regression and nonlinear kernel-ridge regression) are compared to the analytic inversion. Here we simulate the recorded neural signal by applying the forward model to noisy inputs and distorting the output. This controlled scenario allows us to generate as many corresponding input-output pairs as necessary to train the machine-learning techniques, as done

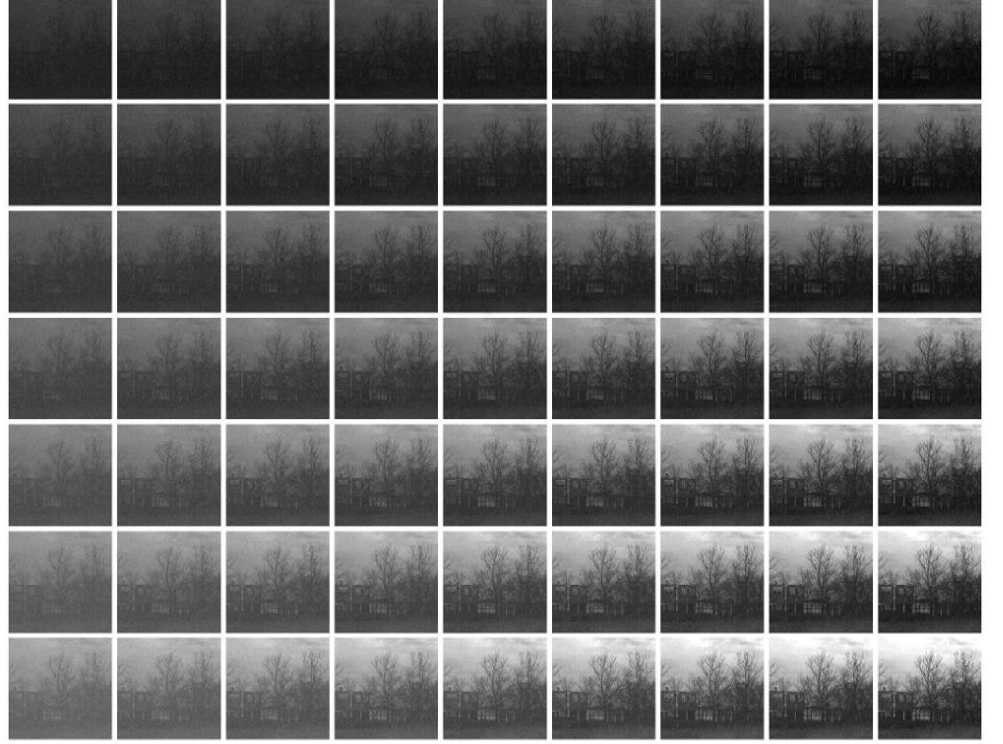


Fig 8. Range of illumination conditions. Average luminance increases from top to bottom and contrast increases from left to right. The learning-based decoders were trained with natural images from the central luminance/contrast condition, under two levels of distortion.

in the experimental acquisition phase in the brain decoding literature.

In fact, regression techniques depend both on the nature of the input-output pairs and on the nature of the distortions. In our simulation we controlled both:

- We controlled the nature of the signals by augmenting a calibrated set of natural images (Van Hateren database [96]) using controlled modifications of the illumination conditions. Specifically, we linearly modified the images to have different average luminance and contrast. We considered 7×9 combinations of luminance and contrast covering the range available in a conventional computer display (see Fig. 8).
- Distortion in the signals comes from random variations in the input (e.g. photon-noise at the retina), random variations of the output (e.g. noise in the cortical response), and distortions due to the measurement (e.g. blurring and noise in the BOLD signal). There is a debate on the psychophysical relevance of the noise at the input versus the neural noise [36,97,98] that we don't want to address here. Just for the sake of the illustration, we controlled these distortions by using uncorrelated noise at the input and blur+noise in the acquisition of the neural signal given by the model. The outputs of the model were blurred using a Gaussian kernel with width of 0.05 degrees (in visual angle units, in the spatial domain corresponding to each subband). We considered two distortion regimes: low-distortion and high distortion. The low-distortion regime involved Gaussian noise at the input with $\sigma = 3cd/m^2$, and Poisson noise at the responses with Fano factor 0.02. The high-distortion regime involved the same sources of noise with input deviation $\sigma = 30cd/m^2$, and internal Fano factor 0.05.

We trained the machine learning algorithms with images from the central luminance/contrast condition and responses under the low and high distortion regimes. We considered 5000 input-output examples in the training. We tested on an image not considered in the training set. In the test we considered the different illumination conditions (the one used in the training and the other conditions considered in Fig. 8), and we applied the two distortion regimes.

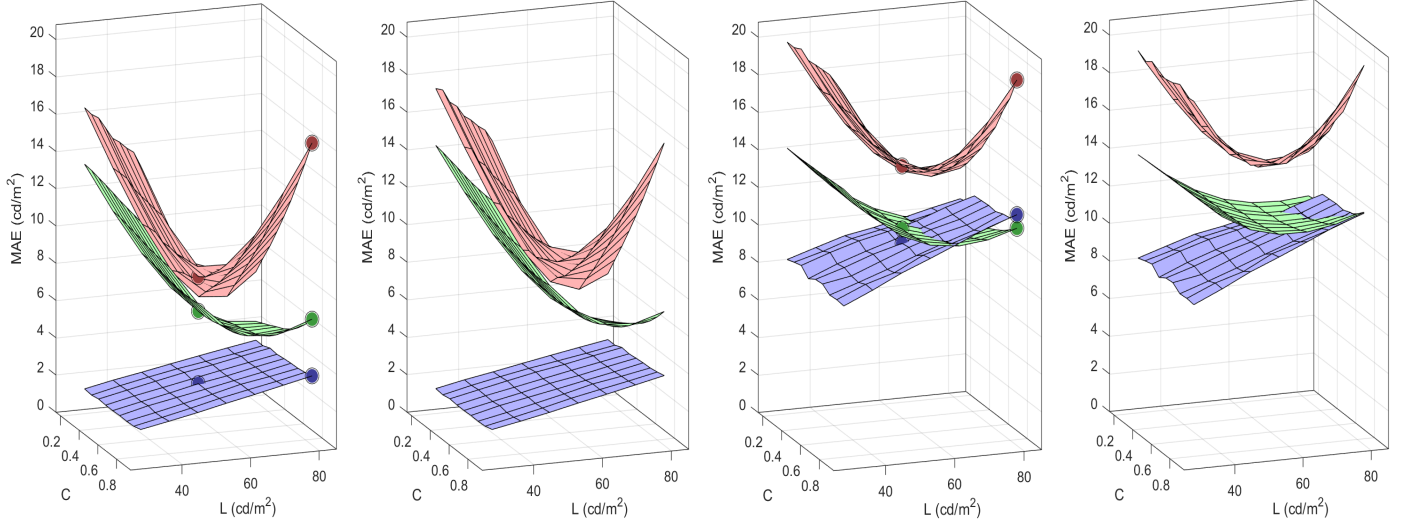


Fig 9. Decoding error. Left panels show the Mean Absolute Error (MAE) in the low-distortion regime and panels of the right show the MAE in the high-distortion regime. In each case surfaces red, green and blue respectively represent the error of the linear regression, non-linear regression and analytic decoders. In each distortion regime, the panel at the left shows the results of the decoders trained for that distortion. The panel of the right represents the situation where the signal is reconstructed by decoders trained in a different distortion regime. The highlighted points in the surfaces correspond to the error of the reconstructed images shown below. Note that the points at the center correspond to the optimal conditions for the learning-based decoders: the appropriate illumination and distortion. Axis label, L means Luminance, and C means Contrast

In each test example, in which illumination may or may not correspond to the training, we decoded the response with 5 decoders: (1) linear decoder trained for the considered distortion, (2) linear decoder trained with noise of different nature, (3) non-linear decoder trained for the considered distortion, (4) non-linear decoder trained with noise of different nature, (5) analytical decoder.

Distortion in the decoded signals is shown in Fig. 9. Here we use the Mean Absolute Error in the input domain (in cd/m^2 units) as distortion measure, just because it has direct physical interpretation (subjective accuracy will be apparent in the visual examples below). Results show that the error of the analytic decoder is lower and substantially more independent from the illumination conditions than the error of the machine learning models that depend on the training. The error surfaces of the data-dependent decoders are curved because they are trained for the central condition in the range. Therefore they have generalization problems in other regions. For bigger distortions all methods have lower performance (the analytic decoding is affected too), but note that in this case, appropriate training becomes more critical because using decoders trained in other distortion conditions increase the error (see how the green surface goes up in the plot of the right).

Beyond Mean Absolute Error or alternative arbitrary measures of reconstruction accuracy (all of them perceptually arguable), it is worth taking an explicit look at the reconstructed images. Representative examples of the decoded signals are shown in Figs. 10 and 11.

Note that the set of visual examples include the best case scenario for the learning-based decoders: training in the same illumination conditions and with distortion of the same nature (top row of Figs. 10 and 11). Even in this best case scenario, the analytic decoder better reproduces the visual structures even in the high distortion condition. These visual examples illustrate the advantages of considering the analytic decoding (generalization ability) with regard to the conventional linear and nonlinear regression.

4 Concluding remarks

This paper addressed relevant mathematical details of biologically plausible feed-forward cascades of linear+nonlinear neural models. These details, namely the Jacobians of the transform (w.r.t.

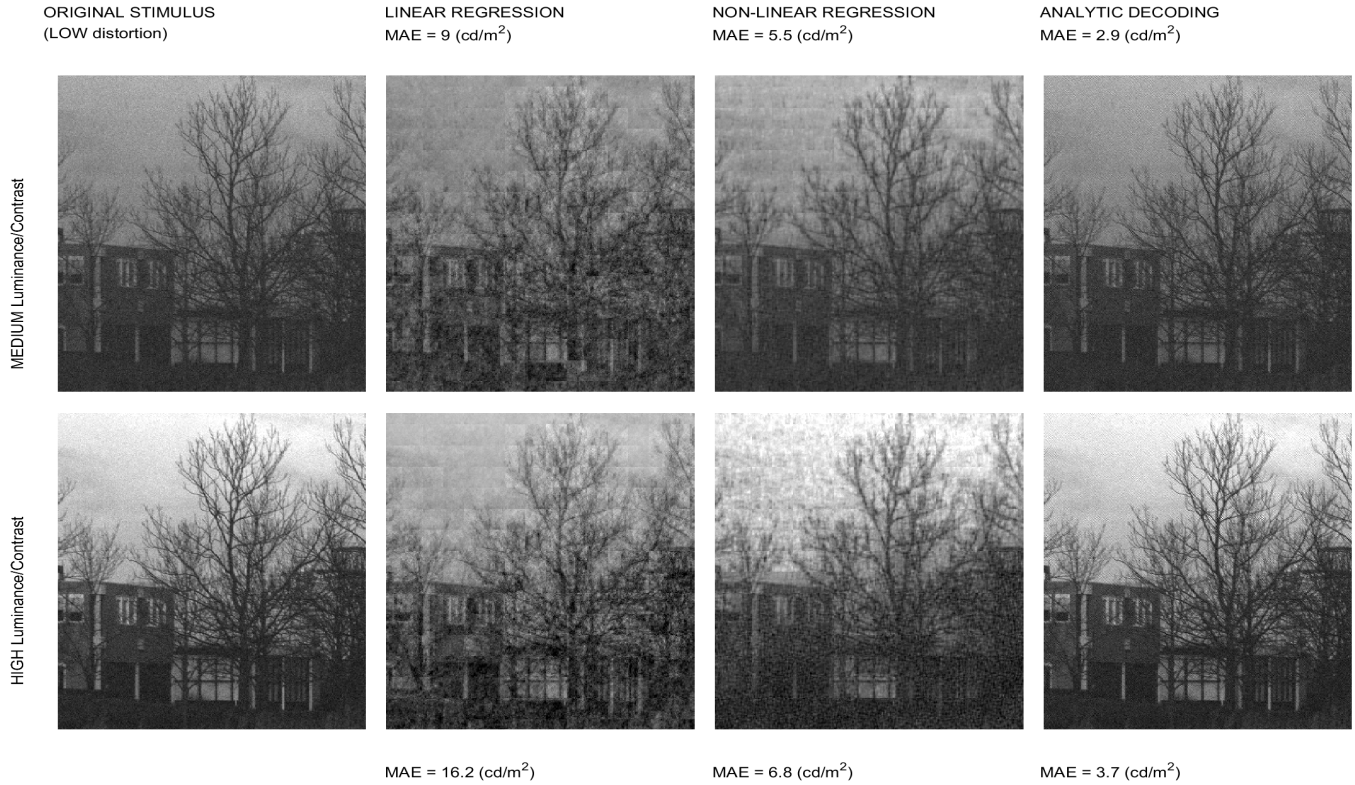


Fig 10. Reconstructions in the low-distortion regime. These six reconstructions correspond to the highlighted dots in the surfaces at the left plot of Fig. 9. The analytic decoding clearly overperforms the learning algorithms even in the case that the image has the illumination conditions used in the training (medium luminance/contrast) and the decoders are those trained for the considered distortion.

the stimulus and w.r.t. the parameters) and the inverse (decoding) transform, are usually disregarded in the conventional experimental literature (e.g. [1] and cites therein), because it is focused on obtaining the forward (encoding) transform in specific experimental settings.

The analytic results presented here for canonical neural models are a necessary reference in multiple biological applications. For instance, the Jacobian of the model with regard to the stimulus characterizes the deformation of the stimulus space induced by the sensory system, and this deformation is key in information-theoretic interpretations of perception [14–21]. These derivatives are also key in generalizing the definition of receptive fields (and features) [18], in describing the propagation of signal/noise information throughout the neural path [36], in computing subjective distances for threshold psychophysics [35, 84], and in synthesizing interesting visual stimuli which are required in novel psychophysics [5, 22, 24]. Moreover, conventional visual brain decoding based in blind regression or estimation [54–56, 59] may benefit from the analytic inverse of the encoding model.

The artificial deep neural networks literature addresses similar cascaded architectures [64], and this community has been recently attracted by the applications of their derivatives and inverse (e.g. in image synthesis [91], or new visualization methods to assess deep networks using derivatives [25] and the inverse [99]). However, this literature doesn't address all the analytic results reported here for biologically plausible nonlinearities such as the Divisive Normalization or the Wilson-Cowan model. One reason is because the most popular artificial networks use simplified nonlinearities and biological plausibility is not one of the goals when training the artificial models [64]. But more importantly, given the increasing popularity of automatic differentiation methods [65], derivatives may be extensively used, but explicit expressions are not given.

Even in the case of training biologically plausible models, the implicit use of the Jacobian matrices (instead of developing explicit expressions) makes the models more difficult to under-

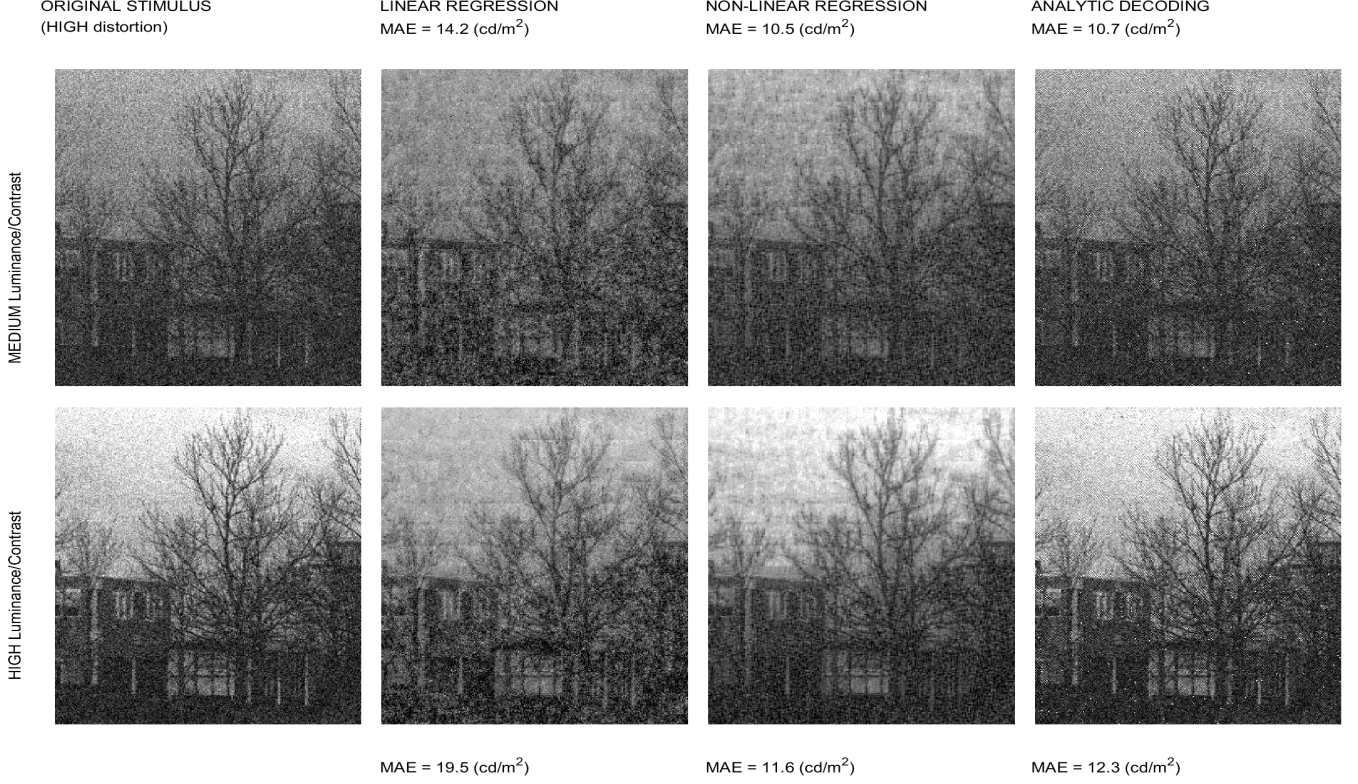


Fig 11. Reconstructions in the high-distortion regime. These six reconstructions correspond to the highlighted dots in the surfaces at the right plot of Fig. 9. In this example, with decoders properly trained in the high-distortion regime, the analytic decoding does not have the best MAE values (MAE is not a visually meaningful measure anyway), but it is certainly better in preserving the visual structures in the scene.

stand. Explicit expressions are better to know how the system works and how the biologically relevant parameters should be. Examples include the extent of the interactions between neurons in the kernels of Divisive Normalization or the Wilson-Cowan models, or the semisaturation in Divisive Normalization and the attenuation constant in the Wilson-Cowan equations. That is why, the explicit analytic results presented here may provide increased intuition and insight than relying on automatic differentiation.

More specifically, the results presented here show that the Jacobian with regard to the stimulus, $\nabla_{\mathbf{x}_0} S$, the Jacobian with regard to the parameters, $\nabla_{\boldsymbol{\theta}} S$, and the inverse, S^{-1} , reduce to knowing the corresponding Jacobian and inverse of the nonlinear part of each layer of the cascade, namely $\nabla_{\mathbf{y}^i} \mathcal{N}^{(i)}$, $\nabla_{\boldsymbol{\theta}^i} \mathcal{N}^{(i)}$, and $\mathcal{N}^{(i)-1}$.

These necessary elements are explicitly given here: the analytical expressions of $\nabla_{\mathbf{y}^i} \mathcal{N}^{(i)}$, $\nabla_{\boldsymbol{\theta}^i} \mathcal{N}^{(i)}$, and $\mathcal{N}^{(i)-1}$ for the case canonical Divisive Normalization. Equivalent results for alternative nonlinearities such as the Wilson-Cowan model [2, 3] and models of brightness perception [4] are also given.

Here we discussed how $\nabla_{\mathbf{x}_0} S$ can be used in the design of stimuli for novel psychophysics (MAXimum Differentiation); how $\nabla_{\boldsymbol{\theta}} S$ can be used to get the parameters of the model using classical psychophysics in image quality ratings; and how visual representation decoding may be benefited from the use of S^{-1} . These illustrations suggest that (1) the resulting model leads to better MAXimum Differentiation results than many successful deep-networks [25], (2) the proposed modular model can be easily extended including extra layers that can be fitted without relying in brute-force techniques (hence improving the results in [35, 39, 41]), and (3) the analytic inverse seems an interesting alternative to blind regression techniques [56, 59] previously used in visual decoding.

Following the example presented here, future modeling efforts should not be restricted to

the forward transform, but they should also address the derivatives and the inverse of the transform.

Acknowledgments.

This work was partially funded by the MINECO projects CICYT TEC2013-50520-EXP and CICYT BFU2014-59776-R, by the European Research Council, Starting Grant ref. 306337, by the Spanish government and FEDER Fund, grant ref. TIN2015-71537-P(MINECO/FEDER,UE), and by the Icrea Academia Award.

References

1. Carandini M, Heeger DJ. Normalization as a canonical neural computation. *Nature Rev Neurosci.* 2012;13(1):51–62.
2. Wilson HR, Cowan JD. Excitatory and inhibitory interactions in localized populations of model neurons. *Biophys J.* 1972;12:1–24.
3. Cowan JD, Neuman J, van Drongelen W. Wilson–Cowan Equations for Neocortical Dynamics. *Journal of Mathematical Neuroscience.* 2016;6(1):1–24. doi:10.1186/s13408-015-0034-5.
4. Cyriac P, Bertalmío M, Kane D, Vazquez-Corral J. A tone mapping operator based on neural and psychophysical models of visual perception. *Proc IS&T/SPIE Electronic Imaging.* 2015;9394. doi:10.1117/12.2081212.
5. Malo J, Simoncelli E. Geometrical and statistical properties of vision models obtained via maximum differentiation. In: *SPIE Electronic Imaging. International Society for Optics and Photonics*; 2015. p. 93940L–93940L.
6. Hillis JM, Brainard DH. Do common mechanisms of adaptation mediate color discrimination and appearance? *JOSA A.* 2005;22(10):2090–2106.
7. Simoncelli EP, Heeger D. A Model of Neuronal Responses in Visual Area MT. *Vision Research.* 1998;38(5):743–761.
8. Watson AB, Solomon JA. A model of visual contrast gain control and pattern masking. *JOSA A.* 1997;14:2379–2391.
9. Barlow HB. Possible principles underlying the transformation of sensory messages. In: Rosenblith W, editor. *Sensory Communication*. Cambridge, MA: MIT Press; 1961. p. 217–234.
10. Barlow H. Redundancy reduction revisited. *Network: Comp Neur Syst.* 2001;12(3):241–253.
11. Seung SH, Lee DD. The manifold ways of perception. *Trends in Cognitive Sciences.* 2006;290:2268–2269.
12. DiCarlo JJ, Cox DD. Untangling invariant object recognition. *Trends in Cognitive Sciences.* 2007;11(8):333–341.
13. Hastie TJ, Tibshirani RJ, Friedman JH. *The elements of statistical learning : data mining, inference, and prediction.* Springer series in statistics. New York: Springer; 2009.
14. Barlow H. A theory about the functional role and synaptic mechanism of visual aftereffects. In: Blakemore C, editor. *Vision: Coding and Efficiency*. Cambridge, UK: Cambridge Univ. Press; 1990.
15. Olshausen B, Field D. Emergence of simple-cell receptive field properties by learning a sparse code for natural images. *Nature.* 1996;281:607–609. doi:10.1038/381607a0.
16. Schwartz O, Simoncelli EP. Natural signal statistics and sensory gain control. *Nature Neurosci.* 2001;4(8):819–825.
17. Malo J, Gutiérrez J. V1 non-linear properties emerge from local-to-global non-linear ICA. *Network: Computation in Neural Systems.* 2006;17(1):85–102.

18. Hyvärinen A, Hurri J, Hoyer PO. Natural Image Statistics: A probabilistic approach to early computational vision. Springer; 2009.
19. Gutmann MU, Laparra V, Hyvärinen A, Malo J. Spatio-chromatic adaptation via higher-order canonical correlation analysis of natural images. *PloS one*. 2014;9(2):e86481.
20. Laparra V, Malo J. Visual aftereffects and sensory nonlinearities from a single statistical framework. *Frontiers in Human Neuroscience*. 2015;9:557. doi:10.3389/fnhum.2015.00557.
21. Golden J, Vilankar K, Wu M, Field D. Conjectures regarding the nonlinear geometry of visual neurons. *Vision Research*. 2016;120:74–92.
22. Wang Z, Simoncelli EP. Maximum differentiation (MAD) competition: A methodology for comparing computational models of perceptual quantities. *Journal of Vision*. 2008;8(12):8–8.
23. Ma K, Wu Q, Duanmu Z, Wang Z, Yong H, Zhang L, et al. Group MAD competition: A new methodology to compare objective image quality models. *IEEE Int Conf Comp Vision Patt Recogn*. 2016;.
24. Malo J, Kane D, Bertalmio M. The Maximum Differentiation competition depends on the Viewing Conditions. *J Vision*. 2016;16(12):822–822.
25. Berardino A, Balle J, Laparra V, Simoncelli EP. Eigen-distortion of hierarchical representations. *Adv Neur Inf Proc NIPS-17*. 2017;.
26. Wiener N. Extrapolation, Interpolation, and Smoothing of Stationary Time Series. New York, Wiley; 1949.
27. Aharon M, Elad M, Bruckstein A. K-SVD: An algorithm for designing overcomplete dictionaries for sparse representation. *Signal Processing, IEEE Transactions on*. 2006;54(11):4311–4322.
28. Ringach DL, Hawken MJ, Shapley R. Receptive field structure of neurons in monkey primary visual cortex revealed by stimulation with natural image sequences. *Journal of Vision*. 2002;2(1):2. doi:10.1167/2.1.2.
29. Spivak M. Calculus on manifolds : a modern approach to classical theorems of advanced calculus. Mathematics monograph series. Reading, Mass. Addison-Wesley; 1965. Available from: <http://opac.inria.fr/record=b1100161>.
30. Dubrovin B, Novikov S, Fomenko A. Modern Geometry: Methods and Applications. New York: Springer Verlag; 1982.
31. Cover TM, Thomas JA. Elements of Information Theory, 2nd Edition. 2nd ed. Wiley-Interscience; 2006.
32. Studeny M, Vejnarova J. In: Jordan MI, editor. The Multi-information function as a tool for measuring stochastic dependence. Kluwer; 1998. p. 261–298.
33. Epifanio I, Gutierrez J, Malo J. Linear transform for simultaneous diagonalization of covariance and perceptual metric matrix in image coding. *Pattern Recognition*. 2003;36(8):1799–1811.
34. Malo J, Epifanio I, Navarro R, Simoncelli EP. Nonlinear image representation for efficient perceptual coding. *IEEE Transactions on Image Processing*. 2006;15(1):68–80.
35. Laparra V, Muñoz-Marí J, Malo J. Divisive normalization image quality metric revisited. *JOSA A*. 2010;27(4):852–864.
36. Ahumada A. Putting the visual system noise back in the picture. *J Opt Soc Am A*. 1987;4(12):2372–2378.
37. Seriès P, Stocker AA, Simoncelli EP. Is the Homunculus "Aware" of Sensory Adaptation? *Neural Computation*. 2009;21(12):3271–3304.
38. da Fonseca M, Samengo I. Derivation of Human Chromatic Discrimination Ability from an Information-Theoretical Notion of Distance in Color Space. *Neural Computation*. 2016;28(12):2628–2655.

39. Watson AB, Malo J. Video quality measures based on the standard spatial observer. In: Image Processing. 2002. Proceedings. 2002 International Conference on. vol. 3. IEEE; 2002. p. III–41.
40. Kendrick KN, Winawer J, Rokem A, Mezer A, Wandell A. A two-stage cascade model of BOLD responses in human visual cortex. *PLoS Comput Biol*. 2013;9(5):e1003079.
41. Marcelo Bertalmio M, Cyriac P, Batard T, Martinez-Garcia M, Malo J. The Wilson-Cowan model describes Contrast Response and Subjective Distortion. *J Vision*. 2017;17(10):657–657.
42. Ballé J, Laparra V, Simoncelli EP. End-to-end Optimized Image Compression. *Int Conf Learn Repres*. 2017;5. doi:arXiv:1611.01704.
43. Sakrison DJ. On the role of the observer and a distortion measure in image transmission. *IEEE Trans Commun*. 1977;25:1251–1267.
44. Watson AB, editor. *Digital Images and Human Vision*. Cambridge, MA, USA: MIT Press; 1993.
45. Wang Z, Bovik AC. Mean squared error: Love it or leave it? A new look at signal fidelity measures. *IEEE Signal Processing Magazine*. 2009;26(1):98–117.
46. Mantiuk R, Myszkowski K, Seidel H. A perceptual framework for contrast processing of high dynamic range images. *ACM Transactions on Applied Perception*. 2000;3(3):286–308.
47. Wallace GK. The JPEG Still Picture Compression Standard. *Commun ACM*. 1991;34(4):30–44.
48. Le Gall D. MPEG: A Video Compression Standard for Multimedia Applications. *Commun ACM*. 1991;34(4):46–58. doi:10.1145/103085.103090.
49. Malo J, Gutiérrez J, Epifanio I, Ferri FJ, Artigas JM. Perceptual feedback in multi-grid motion estimation using an improved DCT quantization. *IEEE Trans Im Proc*. 2001;10(10):1411–1427.
50. Gutiérrez J, Ferri FJ, Malo J. Regularization operators for natural images based on nonlinear perception models. *IEEE Transactions on Image Processing*. 2006;15(1):189–200.
51. Laparra V, Gutiérrez J, Camps-Valls G, Malo J. Image denoising with kernels based on natural image relations. *The Journal of Machine Learning Research*. 2010;11:873–903.
52. Coen-Cagli R, Schwartz O. The impact on midlevel vision of statistically optimal divisive normalization in V1. *Journal of Vision*. 2013;13(8):13.
53. Del Bimbo A. *Visual Information Retrieval*. San Francisco, CA, USA: Morgan Kaufmann Publishers Inc.; 1999.
54. Kay KN, Naselaris T, Prenger RJ, Gallant JL. Identifying natural images from human brain activity. *Nature*. 2008;452(7185):352–355. doi:10.1038/nature06713.
55. Kamitani Y, Tong F. Decoding the visual and subjective contents of the human brain. *Nature neuroscience*. 2005;8(5):679–685.
56. Marré O, Botella V, Simmons T, Mora G, Tkacik G, Berry II MJ. High accuracy dynamical motion from a large retinal population. *PLoS Comput Biol*;11(7):e1004304.
57. Martinez-Garcia M, Galan B, Malo J. Image Reconstruction from Neural Responses: what can we learn from the analytic inverse? *Perception, ECVP-16*. 2016;45(S2):46–46.
58. Laparra V, Jiménez S, Camps-Valls G, Malo J. Nonlinearities and adaptation of color vision from sequential principal curves analysis. *Neural Computation*. 2012;24(10):2751–2788.
59. Stanley GB, F LF, Dan Y. Reconstruction of natural scenes from ensemble responses in the lateral geniculate nucleus. *J Neuroscience*. 1999;19(18):8036–8042.
60. Petersen KB, Pedersen MS. *The Matrix Cookbook*; 2012. Available from: <http://www2.imm.dtu.dk/pubdb/p.php?3274>.

61. Minka TP. Old and New Matrix Algebra Useful for Statistics; 2001.
62. Malo J, Laparra V. Psychophysically tuned divisive normalization approximately factorizes the PDF of natural images. *Neural computation*. 2010;22(12):3179–3206.
63. Kane D, Bertalmío M. System gamma as a function of image-and monitor-dynamic range. *Journal of vision*. 2016;16(6):4–4.
64. Goodfellow I, Bengio Y, Courville A. *Deep Learning*. MIT Press; 2016.
65. Baydin AG, Pearlmutter BA, Radul AA, Siskind JM. Automatic differentiation in machine learning: a survey. *CoRR*. 2015;abs/1502.05767.
66. Laparra V, Berardino A, Ballé J, Simoncelli EP. Perceptually optimized image rendering. *J Opt Soc Am A*. 2017;34(9):1511–1525. doi:10.1364/JOSAA.34.001511.
67. Tekalp AM. *Digital Video Processing*. Upper Saddle River, NJ: Prentice Hall; 1995.
68. Campbell FW, Robson JG. Application of Fourier Analysis to the Visibility of Gratings. *Journal of Physiology*. 1968;197:551–566.
69. Mullen KT. The CSF of Human Colour Vision to Red-Green and Yellow-Blue Chromatic Gratings. *J Physiol*. 1985;359:381–400.
70. Wyszecki G, Stiles WS. *Color Science: Concepts and Methods, Quantitative Data and Formulae*. New York: John Wiley & Sons; 1982.
71. Fairchild MD. *Color Appearance Models*. The Wiley-IS&T Series in Imaging Science and Technology. Wiley; 2013.
72. Wandell BA. *Foundations of Vision*. Massachusetts: Sinauer Assoc. Publish.; 1995.
73. Schwartz G, Rieke F. Nonlinear spatial encoding by retinal ganglion cells: when $1 + 1 \neq 2$. *The Journal of General Physiology*. 2011;138(3):283–290. doi:10.1085/jgp.201110629.
74. Schwartz GW, Okawa H, Dunn FA, Morgan JL, Kerschensteiner D, Wong RO, et al. The spatial structure of a nonlinear receptive field. *Nature neuroscience*. 2012;15(11):1572–1580.
75. Simoncelli E, Heeger D. A Model of Neuronal Responses in Visual Area MT. *Vision Research*. 1998;38(5):743–761.
76. Fairchild MD. *Color appearance models*. Wiley; 2013.
77. Cyriac P, Kane D, Bertalmio M. Optimized Tone Curve for In-Camera Image Processing. *IST Electronic Imaging Conference*. 2016;13:1–7.
78. Palma-Amestoy R, Provenzi E, Bertalmío M, Caselles V. A perceptually inspired variational framework for color enhancement. *IEEE transactions on pattern analysis and machine intelligence*. 2009;31(3):458–474.
79. Huang J, Mumford D. Statistics of natural images and models. In: *Computer Vision and Pattern Recognition, 1999. IEEE Computer Society Conference On.. vol. 1. IEEE; 1999. p. 541–547*.
80. Laughlin SB. Matching coding to scenes to enhance efficiency. In: In Braddick, O.J. & Sleigh, A.C. (Eds) *Physical and Biological Processing of Images*. Springer; 1983. p. 42–52.
81. Cyriac P, Kane D, Bertalmio M. Automatic, Viewing-Condition Dependent Contrast Grading based on Perceptual Models. *SMPTE 2016 Annual Tech Conf*. 2016; p. 1–11.
82. MacLeod D, von der Twer T. The pleistochrome: optimal opponent codes for natural colors. In: Heyer D, Mausfeld R, editors. *Color Perception: From Light to Object*. Oxford, UK: Oxford Univ. Press; 2003.
83. Teo PC, Heeger DJ. Perceptual image distortion. *Proceedings of the SPIE*. 1994;2179:127–141.
84. Pons A, Malo J, Artigas J, Capilla P. Image quality metric based on multidimensional contrast perception models. *Displays*. 1999;20(2):93–110.
85. Brown WRJ, MacAdam DL. Visual sensitivities to combined chromaticity and luminance differences. *JOSA*. 1949;39(10):808—834.

86. Press WH, Teukolsky SA, Vetterling WT, Flannery BP. Numerical Recipes 3rd Edition: The Art of Scientific Computing. 3rd ed. New York, NY, USA: Cambridge University Press; 2007.
87. Golub GH, Van Loan CF. Matrix Computations (3rd Ed.). Baltimore, MD, USA: Johns Hopkins University Press; 1996.
88. Kandel ER, Schwartz JH, Jessell TM, editors. Principles of Neural Science. 3rd ed. New York: Elsevier; 1991.
89. Malo J, Navarro R, Epifanio I, Ferri F, Artigas JM. Non-linear invertible representation for joint statistical and perceptual feature decorrelation. *Lect Not Comp Sci*. 2000;1876:658–667.
90. USC-SIPI Image Database; 1977. <http://sipi.usc.edu/database/>.
91. Gatys LA, Ecker AS, Bethge M. A Neural Algorithm of Artistic Style; 2015. Available from: <http://arxiv.org/abs/1508.06576>.
92. Wang Z, Bovik AC. Modern image quality assessment. *Synthesis Lectures on Image, Video, and Multimedia Processing*. 2006;2(1):1–156.
93. Ponomarenko N, Carli M, Lukin V, Egiazarian K, Astola J, Battisti F. Color Image Database for Evaluation of Image Quality Metrics. *Proc Int Workshop on Multimedia Signal Processing*. 2008; p. 403–408.
94. Wang Z, Bovik AC, Sheikh HR, Simoncelli EP. Image quality assessment: from error visibility to structural similarity. *IEEE Trans Im Proc*. 2004;13(4):600–612.
95. Miyawaki Y, Uchida H, Yamashita O, Sato MA, Morito Y, Tanabe HC, et al. Visual image reconstruction from human brain activity using a combination of multiscale local image decoders. *Neuron*. 2008;60(5):915–929.
96. Hateren JHv, Schaaf Avd. Independent Component Filters of Natural Images Compared with Simple Cells in Primary Visual Cortex. *Proceedings: Biological Sciences*. 1998;265(1394):359–366.
97. Pelli DG. Noise in the visual system may be early. In: Landy M, Movshon JA, editors. *Computational Models of Visual Processing*. Cambridge: MIT Press; 1991. p. 147–152.
98. Georgeson M, Meese T. Fixed or variable noise in contrast discrimination? The jury’s still out... *Vision Research*. 2006;46(25):4294–4303.
99. Mahendran A, Vedaldi A. Understanding Deep Image Representations by Inverting Them. *CoRR*. 2014;abs/1412.0035.
100. Abrams AB, Hillis JM, Brainard DH. The Relation Between Color Discrimination and Color Constancy: When Is Optimal Adaptation Task Dependent? *Neural Computation*. 2007;19(10):2610–2637.
101. Stockman A, Brainard DH. Color vision mechanisms. In: Bass M, editor. *OSA Handbook of Optics* (3rd. Ed.). NY: McGraw-Hill; 2010. p. 147–152.
102. Martinez-Uriegas E. Color detection and color contrast discrimination thresholds. *Proc OSA Meeting*. 1997; p. 81.
103. Simoncelli EP, Adelson EH. Subband Transforms. In: Woods JW, editor. *Subband image coding*. Norwell, MA: Kluwer Academic Publishers; 1990. p. 143–192.
104. Simoncelli EP, Freeman WT, Adelson EH, Heeger DJ. Shiftable multi-scale transforms. *IEEE Trans Information Theory*. 1992;38(2):587–607. doi:10.1109/18.119725.
105. Malo J, Luque MJ. ColorLab: A Matlab Toolbox for Color Science and Calibrated Color Image Processing; 2002. <http://isp.uv.es/code/visioncolor/colorlab.html>.
106. Kleiner M, Brainard D, Pelli D, Broussard C, Wolf T, Niehorster D. Psychtoolbox: A Matlab Toolbox for Vision and Neuroscience Research; 1995. <http://psychtoolbox.org/>.
107. Malo J, Gutiérrez J, Laparra V. BasicVideoTools: A Matlab Toolbox for Neural Processing of Video Signals; 2014. http://isp.uv.es/code/visioncolor/Basic_Video.html.

5 Supplementary Materials

5.1 A cascaded L+NL vision model

The illustrative model considered in the Discussion was originally intended to provide a psychophysically meaningful alternative to the *modular concept* in Structural Similarity measures (SSIM). The authors of SSIM suggest a separate consideration of luminance, contrast and structure [94], which is a sensible approach, but the definition of such factors has no obvious perceptual meaning in SSIM. The idea for a perceptual alternative to SSIM proposed in [5] was addressing one psychophysical factor at a time (i.e. also a modular approach), by using a cascade of linear-nonlinear transforms. In this paper we consider a cascade of 4 L+NL layers, each focused on a different psychophysical factor:

- Layer $S^{(1)}$ linear spectral integration to compute luminance and opponent tristimulus channels, and nonlinear brightness/color response.
- Layer $S^{(2)}$ definition of local contrast by using linear filters and divisive normalization.
- Layer $S^{(3)}$ linear LGN-like contrast sensitivity filter and nonlinear local contrast masking in the spatial domain.
- Layer $S^{(4)}$ linear V1-like wavelet decomposition and nonlinear divisive normalization to account for orientation and scale-dependent masking.

Here we extend previous results by considering two extra layers (1-st and 4-th layers were not considered in [5]). Following the suggestion in [1], here we use the canonical Divisive Normalization for each of these layers. Below we present the expressions of the *forward transforms*, their *derivatives w.r.t. the stimulus*, their *derivatives w.r.t. the parameters*, and their *inverses*.

5.1.1 Forward transforms.

The different layers are almost isomorphic: while the 3rd and 4th layers follow the divisive normalization expression introduced in the main text, the 1st and 2nd layers only differ in that they operate on positive signals (luminance and brightness respectively), and in a global normalization constant in the 1st layer.

Layer 1: Brightness from Radiance

$$\begin{aligned}\mathcal{L}^{(1)} &\equiv \mathbf{y}^1 = L^1 \cdot \mathbf{x}^0 \\ \mathcal{N}^{(1)} &\equiv \mathbf{x}^1 = K(\mathbf{y}^1) \cdot \mathbb{D}_{(\mathbf{b}^1 + H^1 \cdot \mathbf{y}^{1\gamma^1})}^{-1} \cdot \mathbf{y}^{1\gamma^1}\end{aligned}\quad (46)$$

where, L^1 is a matrix with the color matching functions for each spatial location. In particular, restricting ourselves to achromatic information, the only required color matching function would be the spectral sensitivity V_λ [70, 76], leading to the luminance in each spatial location. The global scaling matrix $K(\mathbf{y}^1) = \kappa \left(\mathbb{D}_{\mathbf{b}^1} + \mathbb{D}_{(\frac{\beta}{d} \mathbf{1} \cdot \mathbf{y}^{1\gamma^1})} + \mathbb{1} \right)$, just ensures that the maximum brightness value (for normalized luminance equal to 1) is κ . The role of the interaction kernel in the denominator $H^1 = (\frac{\beta}{d} \mathbf{1} + \mathbb{1})$, where $\mathbf{1}$ is the all-ones $d \times d$ matrix, and $\mathbb{1}$ is the identity matrix, is setting the anchor for the brightness adaptation. With this kernel in the denominator the anchor luminance is related to the average luminance energy $(\mathbf{b}^1 + \frac{\beta}{d} \mathbf{1} \cdot \mathbf{y}^{1\gamma^1})$. The effect of this nonlinear transform is a Weber-like adaptive saturation [100]. Similar nonlinear behavior can be assumed for the opponent chromatic channels [58, 76, 101], but we didnt implemented the color version of the model.

Layer 2: Contrast from Brightness

$$\begin{aligned}\mathcal{L}^{(2)} &\equiv \mathbf{y}^2 = L^2 \cdot \mathbf{x}^1 \\ \mathcal{N}^{(2)} &\equiv \mathbf{x}^2 = \mathbb{D}_{(\mathbf{b}^2 + H^2 \cdot \mathbf{y}^2)}^{-1} \cdot \mathbf{y}^2\end{aligned}\quad (47)$$

where the linear stage computes the deviation of point-wise brightness with regard to the local brightness through $L^2 = \mathbb{1} - \mathcal{H}^n$, and this kernel in the *numerator*, \mathcal{H}^n , represents the convolution by a two-dimensional Gaussian (as in Eq. 33). The normalization through $H^2 = \mathcal{H}^d \cdot (\mathbb{1} - \mathcal{H}^n)^{-1}$, where the kernel in the *denominator*, \mathcal{H}^d , is another two-dimensional Gaussian kernel, leads to the standard definition of contrast: normalization of the deviation of brightness by the local brightness.

Layer 3: Contrast sensitivity and spatial masking

$$\begin{aligned}\mathcal{L}^{(3)} &\equiv \mathbf{y}^3 = L^3 \cdot \mathbf{x}^2 \\ \mathcal{N}^{(3)} &\equiv \mathbf{x}^3 = \mathbb{D}_{\text{sign}(\mathbf{y}^3)} \cdot \mathbb{D}_{(b^3 + H^3 \cdot |\mathbf{y}^3|^{\gamma^3})}^{-1} \cdot |\mathbf{y}^3|^{\gamma^3}\end{aligned}\quad (48)$$

where L^3 is the convolution matrix equivalent to the application of a Contrast Sensitivity Function (CSF) [68]. The rows of this matrix consist of displaced versions of center-surround (LGN-like) receptive fields (impulse response of the CSF [102]). The kernel in the denominator, H^3 , represents the convolution by another two-dimensional Gaussian that computes the local contrast energy that masks the responses in high-energy environments.

Layer 4: Wavelet analysis and frequency masking

$$\begin{aligned}\mathcal{L}^{(4)} &\equiv \mathbf{y}^4 = L^4 \cdot \mathbf{x}^3 \\ \mathcal{N}^{(4)} &\equiv \mathbf{x}^4 = \mathbb{D}_{\text{sign}(\mathbf{y}^4)} \cdot \mathbb{D}_{(b^4 + H^4 \cdot |\mathbf{y}^4|^{\gamma^4})}^{-1} \cdot |\mathbf{y}^4|^{\gamma^4}\end{aligned}\quad (49)$$

where L^4 is the matrix of Gabor-like receptive fields corresponding to V1-like sensors [103]. The kernel in the denominator, H^4 , represents the masking interaction between sensors tuned to different space, frequency and orientation [8].

5.1.2 Derivatives.

Due to the slight differences in the transforms for the 1st and 2nd layers, the derivatives and inverses are slightly different from Results I, II and III presented in the main text. However, here we simply list the corresponding expressions because their derivation is straightforward using the methods described to get Results I, II and III. Since the formulation of the 3rd and 4th layers is the one given in the main text, the corresponding expressions will not be repeated here.

Derivatives w.r.t stimulus.

$$\nabla_{\mathbf{y}^1} \mathcal{N}^{(1)} = K(\mathbf{y}^1) \cdot \left[\mathbb{D}_{\mathcal{D}^{(1)}(\mathbf{y}^1)}^{-1} - \mathbb{D}\left(\frac{\mathbf{y}^1 \gamma^1}{\mathcal{D}^{(1)}(\mathbf{y}^1)^2}\right) \cdot H^1 \right] \cdot \mathbb{D}(\gamma^1 \mathbf{y}^1 \gamma^{1-1}) + \frac{\kappa \beta}{d} \mathbb{D}\left(\frac{\mathbf{y}^1 \gamma^1}{\mathcal{D}^{(1)}(\mathbf{y}^1)}\right) \cdot \mathbb{1} \cdot \mathbb{D}(\gamma^1 \mathbf{y}^1 \gamma^{1-1}) \quad (50)$$

$$\nabla_{\mathbf{y}^2} \mathcal{N}^{(2)} = \left[\mathbb{D}_{\mathcal{D}^{(2)}(\mathbf{y}^2)}^{-1} - \mathbb{D}\left(\frac{\mathbf{y}^2}{\mathcal{D}^{(2)}(\mathbf{y}^2)^2}\right) \cdot H^2 \right] \quad (51)$$

Where, as in the main text, $\mathcal{D}^{(i)}$, stands for the denominator corresponding to the normalization in the i -th layer.

Derivatives w.r.t. the semisaturation b

$$\nabla_{b^1} \mathcal{N}^{(1)} = -K(\mathbf{y}^1) \cdot \mathbb{D}_{\mathbf{y}^1 \gamma^1} \cdot \mathbb{D}_{\mathcal{D}^{(1)}(\mathbf{y}^1)}^{-2} + \kappa \mathbb{D}_{\mathbf{y}^1 \gamma^1} \cdot \mathbb{D}_{\mathcal{D}^{(1)}(\mathbf{y}^1)}^{-1} \quad (52)$$

$$\nabla_{b^2} \mathcal{N}^{(2)} = -\mathbb{D}_{\mathbf{y}^2} \cdot \mathbb{D}_{\mathcal{D}^{(2)}(\mathbf{y}^2)}^{-2} \quad (53)$$

Derivatives w.r.t. the excitation-inhibition exponent γ

$$\nabla_{\gamma^1} \mathcal{N}^{(1)} = \left[K(\mathbf{y}^1) \cdot \mathbb{D}_{\mathcal{D}^{(1)}(\mathbf{y}^1)}^{-1} \cdot \left[\mathbb{D}_{\log \mathbf{y}^1} - \mathbb{D}_{\mathcal{D}^{(1)}(\mathbf{y}^1)}^{-1} \cdot \mathbb{D}\left(H^1 \cdot \mathbb{D}_{(\mathbf{y}^1 \gamma^1)} \cdot \log \mathbf{y}^1\right) \right] + \frac{\kappa \beta}{d} \mathbb{D}\left(\frac{\mathbf{y}^1 \gamma^1}{\mathcal{D}^{(1)}(\mathbf{y}^1)}\right) \cdot \mathbb{1} \cdot \mathbb{D}_{\log \mathbf{y}^1} \right] \cdot \mathbf{y}^{1 \gamma^1} \quad (54)$$

Derivatives w.r.t. the global scaling constant κ

$$\nabla_{\kappa} \mathcal{N}^{(1)} = \left(\mathbb{D}_{b^1} + \mathbb{D}_{\left(\frac{\beta}{d} \mathbb{1} \cdot \mathbf{y}^{1\gamma^1}\right)} + \mathbb{1} \right) \cdot \mathbb{D}_{(b^1 + H^1 \cdot \mathbf{y}^{1\gamma^1})}^{-1} \cdot \mathbf{y}^{1\gamma^1} \quad (55)$$

Derivatives w.r.t. the parameters of kernels L and H . The parameter of the normalization kernel of the 1st stage, H^1 , is the weight, β , of the adaptation anchor for the luminance. The derivative w.r.t. β is:

$$\nabla_{\beta} \mathcal{N}^{(1)} = \frac{1}{d} \mathbb{D}_{\mathcal{D}^{(1)}(\mathbf{y}^1)}^{-1} \cdot \left[\kappa \mathbb{D}_{(\mathbb{1} \cdot \mathbf{y}^{1\gamma^1})} - K(\mathbf{y}^1) \cdot \mathbb{D}_{\left(\frac{\mathbf{y}^{1\gamma^1}}{\mathcal{D}^{(1)}(\mathbf{y}^1)}\right)} \cdot \mathbb{1} \right] \cdot \mathbf{y}^{1\gamma^1} \quad (56)$$

Contrast computation in the 2nd layer depends on the application of two Gaussian kernels: one in the linear stage, $L^2 = \mathbb{1} - \mathcal{H}^n$, and another in the nonlinear stage, $H^2 = \mathcal{H}^d \cdot (\mathbb{1} - \mathcal{H}^n)^{-1}$. The rows of each of these kernels depends on the corresponding width and amplitude.

For the set of widths and amplitudes of \mathcal{H}^n , σ^n and \mathbf{c}^n :

$$\nabla_{\sigma^n} \mathcal{L}^{(2)} = -\nabla_{\mathbf{y}^2} \mathcal{N}^{(2)} \cdot \text{diag} \left[\begin{pmatrix} \mathbf{x}^{1\top} \\ \mathbf{x}^{1\top} \\ \vdots \\ \mathbf{x}^{1\top} \end{pmatrix} \cdot F^n \right] \quad (57)$$

where, $F_{kk'}^n = c_k^n \frac{dp_{k1} dp_{k2}}{2\pi \sigma_k^{n2}} \left(\Delta_{kk'}^2 - 2\sigma_k^{n2} \right) e^{-\frac{\Delta_{kk'}^2}{2\sigma_k^{n2}}}$. In this expression, $\Delta_{kk'}^2$ and $dp_{k1} dp_{k2}$ have the same meaning used in the main text in the context of the Gaussian kernels, Eq. 33.

$$\nabla_{\mathbf{c}^n} \mathcal{L}^{(2)} = -\nabla_{\mathbf{y}^2} \mathcal{N}^{(2)} \cdot \text{diag} \left[\begin{pmatrix} \mathbf{x}^{1\top} \\ \mathbf{x}^{1\top} \\ \vdots \\ \mathbf{x}^{1\top} \end{pmatrix} \cdot G^n \right] \quad (58)$$

where, $G_{kk'}^n = \frac{dp_{k1} dp_{k2}}{2\pi \sigma_k^{n2}} e^{-\frac{\Delta_{kk'}^2}{2\sigma_k^{n2}}}$.

Similarly, for the set of widths and amplitudes of \mathcal{H}^d , σ^d and \mathbf{c}^d :

$$\nabla_{\sigma^d} \mathcal{N}^{(2)} = -\text{diag} \left[\mathbb{D}_{\mathbf{y}^2} \cdot \mathbb{D}_{\mathcal{D}^{(2)}(\mathbf{y}^2)}^{-2} \cdot \begin{pmatrix} ((\mathbb{1} - \mathcal{H}^n)^{-1} \cdot \mathbf{y}^2)^\top \\ ((\mathbb{1} - \mathcal{H}^n)^{-1} \cdot \mathbf{y}^2)^\top \\ \vdots \\ ((\mathbb{1} - \mathcal{H}^n)^{-1} \cdot \mathbf{y}^2)^\top \end{pmatrix} \cdot F^d \right] \quad (59)$$

where, $F_{kk'}^d = c_k^d \frac{dp_{k1} dp_{k2}}{2\pi \sigma_k^{d2}} \left(\Delta_{kk'}^2 - 2\sigma_k^{d2} \right) e^{-\frac{\Delta_{kk'}^2}{2\sigma_k^{d2}}}$.

$$\nabla_{\mathbf{c}^d} \mathcal{N}^{(2)} = -\text{diag} \left[\mathbb{D}_{\mathbf{y}^2} \cdot \mathbb{D}_{\mathcal{D}^{(2)}(\mathbf{y}^2)}^{-2} \cdot \begin{pmatrix} ((\mathbb{1} - \mathcal{H}^n)^{-1} \cdot \mathbf{y}^2)^\top \\ ((\mathbb{1} - \mathcal{H}^n)^{-1} \cdot \mathbf{y}^2)^\top \\ \vdots \\ ((\mathbb{1} - \mathcal{H}^n)^{-1} \cdot \mathbf{y}^2)^\top \end{pmatrix} \cdot G^d \right] \quad (60)$$

where, $G_{kk'}^d = \frac{dp_{k1} dp_{k2}}{2\pi \sigma_k^{d2}} e^{-\frac{\Delta_{kk'}^2}{2\sigma_k^{d2}}}$.

5.1.3 Inverses.

The inverse of the 2nd layer is simpler than Result III,

$$\mathbf{y}^2 = (\mathbb{1} - \mathbb{D}_{\mathbf{x}^2} \cdot H^2)^{-1} \cdot \mathbb{D}_{\mathbf{x}^2} \cdot \mathbf{b}^2 \quad (61)$$

On the contrary, the inverse of the 1st layer may require an iterative process. As stated above, the saturation in Eq. 46 depends on an anchor for the luminance adaptation. In the forward transform this anchor is computed through the average of the known luminance in the considered image. But of course, the luminance values are not known when computing the inverse. If there is no other way to assume certain adaptation state (or average luminance), the solution may be achieved iteratively. First, assume certain reasonable average luminance to estimate the scaling matrix K . Then, use this estimated K to compute a first estimation of the luminance from known the brightness response and the analytic inverse. This new estimation of the luminance vector can be used again for a better estimation of K , and this process can be iterated. By using the *energy* notation used in the main text, $\mathbf{e}^1 = \mathbf{y}^{1\gamma^1}$, and using n as iteration index,

$$\begin{aligned} \mathbf{e}_n^1 &\rightarrow K_n(\mathbf{e}_n^1) = \kappa \left(\mathbb{D}_{\mathbf{b}^1} + \mathbb{D}_{\left(\frac{\beta}{\alpha} \mathbf{1} \cdot \mathbf{e}_n^1\right)} + \mathbb{1} \right) \\ \mathbf{e}_{n+1}^1 &= \left(\mathbb{1} - \mathbb{D}_{(K_n^{-1} \cdot \mathbf{x}^1)} \cdot H^1 \right)^{-1} \cdot \mathbb{D}_{(K_n^{-1} \cdot \mathbf{x}^1)} \cdot \mathbf{b}^1 \end{aligned} \quad (62)$$

5.1.4 Note: alternative formulations in certain layers.

The illustrative model used in the Discussion, described in this supplementary material, and implemented in the toolbox associated to the paper, is based on a cascade of almost isomorphic L+NL transforms (see Eqs. 46 - 49). However, as stated in the main text, this implementation based on isomorphic divisive normalization transforms is not the only possible choice.

Section 2.1 in the main text cites specific alternatives for the brightness transform (the two-gamma curve [4, 63, 77]) and for the interaction between V1-like sensors (the Wilson-Cowan model [2, 3]). The alternative transforms and their jacobians w.r.t. the stimulus were presented in the main text in sections 2.1 and 2.2. The analytic inverse of the Wilson-Cowan interaction was presented in section 2.4.

The inverse of the two-gamma nonlinearity was not addressed there because, given the coupling between the input and the exponent (see Eq. 14), Eq. 13 has no analytical inverse. Nevertheless, iterative approximations to the actual luminance value can be obtained in the following way. First one makes an initial guess of the exponent (for instance the average value between the two extremes), and then one obtains the first guess for the luminance assuming this approximate exponent. Afterwards, the estimate of the exponent is recomputed from the new luminance estimate, and so on. At the n -th iteration,

$$\begin{aligned} n &= 0 \quad \left\{ \begin{array}{l} \gamma_0^1 = \frac{1}{2}(\gamma_L + \gamma_H) \\ \mathbf{y}_0^1 = \mathbf{x}^{1\frac{1}{\gamma_0^1}} \end{array} \right. \\ n &> 0 \quad \left\{ \begin{array}{l} \gamma_n^1 = \gamma^1(\mathbf{y}_{n-1}^1) \\ \mathbf{y}_n^1 = \mathbf{x}^{1\frac{1}{\gamma_n^1}} \end{array} \right. \end{aligned} \quad (63)$$

where the subindex n indicates the iteration and $\gamma^1(\mathbf{y}^1)$ is computed using Eq. 14. Note that, given the singularity at the origin of the jacobian of the two-gamma response (see the discussion made after Eq. 27), the above only holds for big enough luminance, $\mathbf{y}^1 \in [\epsilon^{\gamma^1(\epsilon)}, 1]$. For small luminance values, $\mathbf{y}^1 \in [0, \epsilon^{\gamma^1(\epsilon)}]$, it holds the robust regime introduced to solve the mentioned singularity, and this parabolic expression is invertible:

$$\mathbf{y}^1 = \frac{1}{\sqrt{a_1}} \sqrt{\mathbf{x}^1 + \frac{a_2^2}{4a_1}} - \frac{a_2}{2a_1} \quad (64)$$

5.2 Derivative of a linear function with regard to its parameters

The technical result in this section, namely Eq. 68, is necessary when deriving one of the analytical results of the paper: the Jacobian with regard to the parameters requires this sort of derivative in Eq. 21 (dependence with receptive fields) and in Eq. 32 (dependence with the masking kernel).

Given a general linear function depending on the rectangular matrix $L^i \in \mathbb{R}^{d_i \times d_{i-1}}$,

$$\mathbf{y}^i = \mathcal{L}^{(i)}(\mathbf{x}^{i-1}, L^i) = L^i \cdot \mathbf{x}^{i-1}$$

here we are interested in a matrix expression for its derivatives with regard to the parameters, L^i , i.e. we address the issue of the matrix form of,

$$\nabla_{L^i} \mathcal{L}^{(i)} = \frac{\partial \mathbf{y}^i}{\partial L^i}$$

In order to do so, go back to the individual dimensions for a moment: remember that we have d_i 1-dimensional functions like this,

$$y_k^i = \sum_{k'=1}^{d_{i-1}} L_{kk'}^i x_{k'}^{i-1}$$

where $k = 1, \dots, d_i$. Therefore, $\nabla_{L^i} \mathbf{y}^i \in \mathbb{R}^{d_i \times (d_i \times d_{i-1})}$ because $\mathbf{y}^i \in \mathbb{R}^{d_i \times 1}$ and we have $d_i \times d_{i-1}$ elements in L^i . In this setting,

$$\frac{\partial y_k^i}{\partial L_{lm}^i} = \delta_{kl} x_m^{i-1} \quad (65)$$

With a convenient rearrangement of L^i , it is possible to give a single matrix expression that summarizes the multiple element-wise derivatives in Eq. 65.

In particular, here we rearrange the parameters of the linear transform in the column vector $\mathbf{l}^i = \text{vect}(L^{i\top}) \in \mathbb{R}^{(d_i \times d_{i-1}) \times 1}$. This arrangement is sensible in our context (feed-forward neural model) because of the following considerations. As stated above, the k -th row of the matrix, $L_{k\star}^i$, represents the linear weights of the k -th linear sensor in the i -th linear stage \mathcal{L}^i . In other words, $L_{k\star}^i$ represents the weighted connectivity or interaction of the k -th linear sensor with the previous stage. Given the scalar-product description of receptive fields [15, 28], one may say that each $L_{k\star}^i$ plays the role of a *receptive field* in the domain \mathbf{x}^{i-1} because the k -th response is computed through these scalar products: $y_k^i = L_{k\star}^i \cdot \mathbf{x}^{i-1} = \mathbf{x}^{i-1\top} \cdot L_{k\star}^{i\top}$. With the proposed rearrangement, the column vector \mathbf{l}^i is built by concatenating the transposed *receptive fields* of every linear sensor in the i -th layer,

$$\mathbf{l}^i = \text{vect}(L^{i\top}) = \begin{pmatrix} \begin{pmatrix} L_{11}^i \\ L_{12}^i \\ \vdots \\ L_{1d_{i-1}}^i \end{pmatrix} \\ \begin{pmatrix} L_{21}^i \\ L_{22}^i \\ \vdots \\ L_{2d_{i-1}}^i \end{pmatrix} \\ \vdots \\ \begin{pmatrix} L_{d_i1}^i \\ L_{d_i2}^i \\ \vdots \\ L_{d_id_{i-1}}^i \end{pmatrix} \end{pmatrix} = \begin{pmatrix} \begin{pmatrix} \vdots \\ L_{1\star}^{i\top} \\ \vdots \end{pmatrix} \\ \begin{pmatrix} \vdots \\ L_{2\star}^{i\top} \\ \vdots \end{pmatrix} \\ \vdots \\ \begin{pmatrix} \vdots \\ L_{d_i\star}^{i\top} \\ \vdots \end{pmatrix} \end{pmatrix} \quad (66)$$

As a result, the small variations of the linear responses due to perturbations in the parameters of the linear transform (which are $\Delta y_k^i = \mathbf{x}^{i-1\top} \cdot \Delta L_{k\star}^{i\top}$), can be put in matrix form using the rearrangement $\mathbf{l}^i = \text{vect}(L^{i\top})$:

$$\begin{pmatrix} \Delta y_1^i \\ \Delta y_2^i \\ \vdots \\ \Delta y_{d_i}^i \end{pmatrix} = \begin{pmatrix} (\dots \mathbf{x}^{i-1\top} \dots) & (\dots 0 \dots) & \dots & (\dots 0 \dots) \\ (\dots 0 \dots) & (\dots \mathbf{x}^{i-1\top} \dots) & \dots & (\dots 0 \dots) \\ \vdots & \vdots & \ddots & \vdots \\ (\dots 0 \dots) & (\dots 0 \dots) & \dots & (\dots \mathbf{x}^{i-1\top} \dots) \end{pmatrix} \cdot \Delta \mathbf{l}^i \quad (67)$$

since this leads to the appropriate scalar products. Identifying terms with the linear approximation in terms of the Jacobian,

$$\Delta \mathbf{y}^i = \nabla_{L^i} \mathcal{L}^{(i)} \cdot \Delta \mathbf{l}^i = \frac{\partial \mathbf{y}^i}{\partial L^i} \cdot \Delta \mathbf{l}^i$$

we see that, assuming the referred rearrangement of the parameters, the Jacobian we are interested in is given by the block diagonal matrix shown above.

In summary, given the linear transform $\mathbf{y}^i = L^i \cdot \mathbf{x}^{i-1}$, the Jacobian with regard to its parameters is:

$$\nabla_{L^i} \mathcal{L}^{(i)} = \frac{\partial \mathbf{y}^i}{\partial L^i} = \mathbb{B}_{(\mathbf{x}^{i-1}^\top)}^{d_i} \quad (68)$$

where $\mathbb{B}_{(A)}^m$ is a *block-diagonal* matrix built by replicating m times the matrix (or vector) A along the diagonal.

5.3 Derivation of the Jacobian with regard to the stimulus

In this section we provide the proofs for (a) Eq. 24 for the canonical divisive normalization, and (b) Eq. 27 for the particular two-gamma nonlinearity. Remember the Jacobian of the particular Wilson-Cowan nonlinearity was already derived in the Results section (Eqs. 25 and 26).

Divisive normalization: proof of Eq. 24. Explicitly considering the sign and amplitude terms of the nonlinearity in Eq. 10, we can write, $\mathcal{N}^{(i)}(\mathbf{y}^i) = \mathbb{D}_{\text{sign}(\mathbf{y}^i)} \cdot N^{(i)}(\mathbf{e}^i)$. Then, using the chain rule, we have:

$$\nabla_{\mathbf{y}^i} \mathcal{N}^{(i)} = \nabla_{\mathbf{y}^i} \text{sign}(\mathbf{y}^i) \cdot \mathbb{D}_{N^{(i)}(\mathbf{e}^i)} + \mathbb{D}_{\text{sign}(\mathbf{y}^i)} \cdot \nabla_{\mathbf{y}^i} N^{(i)}(\mathbf{e}^i)$$

where,

$$\nabla_{\mathbf{y}^i} \text{sign}(\mathbf{y}^i) \cdot \mathbb{D}_{N^{(i)}(\mathbf{e}^i)} = 0, \text{ since } \text{sign}(y_k^i) \text{ is constant } \forall y_k^i \neq 0, \text{ and } N^{(i)}(0) = 0$$

$$\nabla_{\mathbf{y}^i} N^{(i)}(\mathbf{e}^i) = \nabla_{\mathbf{e}^i} N^{(i)}(\mathbf{e}^i) \cdot \nabla_{\mathbf{y}^i} \mathbf{e}^i$$

where,

$$\nabla_{\mathbf{e}^i} N^{(i)}(\mathbf{e}^i) = \nabla_{\mathbf{e}^i} \mathbf{e}^i \cdot \mathbb{D}\left(\frac{1}{\mathcal{D}^{(i)}(\mathbf{e}^i)}\right) + \mathbb{D}_{\mathbf{e}^i} \cdot \nabla_{\mathbf{e}^i} \frac{1}{\mathcal{D}^{(i)}(\mathbf{e}^i)}$$

where,

$$\nabla_{\mathbf{e}^i} \mathbf{e}^i = \mathbb{I}$$

$$\nabla_{\mathbf{e}^i} \frac{1}{\mathcal{D}^{(i)}(\mathbf{e}^i)} = -\mathbb{D} \frac{1}{\mathcal{D}^{(i)}(\mathbf{e}^i)^2} \cdot \nabla_{\mathbf{e}^i} \mathcal{D}^{(i)}(\mathbf{e}^i) = -\mathbb{D} \frac{1}{\mathcal{D}^{(i)}(\mathbf{e}^i)^2} \cdot H^i$$

therefore,

$$= \mathbb{D}\left(\frac{1}{\mathcal{D}^{(i)}(\mathbf{e}^i)}\right) - \mathbb{D}_{\mathbf{e}^i} \cdot \mathbb{D} \frac{1}{\mathcal{D}^{(i)}(\mathbf{e}^i)^2} \cdot H^i$$

$$\nabla_{\mathbf{y}^i} \mathbf{e}^i = \nabla_{|\mathbf{y}^i|} \mathbf{e}^i \cdot \nabla_{\mathbf{y}^i} |\mathbf{y}^i|$$

where,

$$\nabla_{|\mathbf{y}^i|} \mathbf{e}^i = \mathbb{D}_{\gamma^i |\mathbf{y}^i|^{\gamma^i - 1}}$$

$$\nabla_{\mathbf{y}^i} |\mathbf{y}^i| = \mathbb{D}_{\text{sign}(\mathbf{y}^i)}, \text{ since the slope of } |\mathbf{y}^i| \text{ is } \text{sign}(\mathbf{y}^i)$$

therefore,

$$= \mathbb{D}_{\gamma^i |\mathbf{y}^i|^{\gamma^i - 1}} \cdot \mathbb{D}_{\text{sign}(\mathbf{y}^i)}$$

as a result,

$$= \left[\mathbb{D}\left(\frac{1}{\mathcal{D}^{(i)}(\mathbf{e}^i)}\right) - \mathbb{D} \frac{\mathbf{e}^i}{\mathcal{D}^{(i)}(\mathbf{e}^i)^2} \cdot H^i \right] \cdot \mathbb{D}_{\gamma^i |\mathbf{y}^i|^{\gamma^i - 1}} \cdot \mathbb{D}_{\text{sign}(\mathbf{y}^i)}$$

finally, putting all the pieces together, we have Eq. 24.

Two-gamma nonlinearity: proof of Eq. 27. Given the separation in sign/amplitude, $\mathbf{x} = \mathbb{D}_{\text{sign}(\mathbf{y})} \cdot |\mathbf{y}|^{\gamma(|\mathbf{y}|)}$, the derivative is,

$$\frac{\partial \mathbf{x}}{\partial \mathbf{y}} = \frac{\partial \mathbf{x}}{\partial |\mathbf{y}|} \cdot \frac{\partial |\mathbf{y}|}{\partial \mathbf{y}} = \left[\frac{\partial \text{sign}(\mathbf{y})}{\partial |\mathbf{y}|} \cdot \mathbb{D}_{|\mathbf{y}|^{\gamma(|\mathbf{y}|)}} + \mathbb{D}_{\text{sign}(\mathbf{y})} \cdot \frac{\partial |\mathbf{y}|^{\gamma(|\mathbf{y}|)}}{\partial |\mathbf{y}|} \right] \cdot \frac{\partial |\mathbf{y}|}{\partial \mathbf{y}}$$

where the first term in the parenthesis cancels for the same reasons stated in the previous proof, and the slope the magnitude is the sign, therefore,

$$\frac{\partial \mathbf{x}}{\partial \mathbf{y}} = \mathbb{D}_{\text{sign}(\mathbf{y})} \cdot \frac{\partial |\mathbf{y}|^{\gamma(|\mathbf{y}|)}}{\partial |\mathbf{y}|} \cdot \mathbb{D}_{\text{sign}(\mathbf{y})} = \frac{\partial |\mathbf{y}|^{\gamma(|\mathbf{y}|)}}{\partial |\mathbf{y}|}$$

where signs cancel out because all the matrices are diagonal and hence the product is commutative. Now, by calling $f = |\mathbf{y}|^{\gamma(|\mathbf{y}|)}$, our problem is computing $\frac{\partial f}{\partial |\mathbf{y}|}$. This notation is convenient since, taking the element-wise logarithm,

$$\log f = \gamma(|\mathbf{y}|) \odot \log |\mathbf{y}| \quad (69)$$

and hence, applying the chain rule in the derivative of $\log f$ we have,

$$\frac{\partial \log f}{\partial |\mathbf{y}|} = \frac{\partial \log f}{\partial f} \cdot \frac{\partial f}{\partial |\mathbf{y}|} = \mathbb{D}_f^{-1} \cdot \frac{\partial f}{\partial |\mathbf{y}|} \Rightarrow \frac{\partial f}{\partial |\mathbf{y}|} = \mathbb{D}_f \cdot \frac{\partial \log f}{\partial |\mathbf{y}|} \quad (70)$$

because the derivative matrices are diagonal, and hence all the products and quotients are Hadamard.

On the other hand, direct derivation of Eq. 69, leads to,

$$\frac{\partial \log f}{\partial |\mathbf{y}|} = \frac{\partial \gamma(|\mathbf{y}|)}{\partial |\mathbf{y}|} \cdot \mathbb{D}_{\log |\mathbf{y}|} + \mathbb{D}_{\gamma(|\mathbf{y}|)} \cdot \frac{\partial \log |\mathbf{y}|}{\partial |\mathbf{y}|} \quad (71)$$

where, given the expression of the exponent γ , Eq. 14, its straightforward derivative:

$$\frac{\partial \gamma(|\mathbf{y}|)}{\partial |\mathbf{y}|} = \mathbb{D}_{\left((\gamma_H - \gamma_L) \cdot \frac{m |\mathbf{y}|^{(m-1)} \cdot \mu_1^m}{(\mu_1^m + |\mathbf{y}|^m)^2} \right)}$$

Then, plugging this derivative into Eq. 71, and the result into Eq. 70, we have Eq. 27.

5.4 Derivation of the Jacobian with regard to the parameters

In this section we provide the proofs for the Jacobian of the canonical divisive normalization, namely for the Eqs. 30 - 35.

Dependence on γ^i : Proof of Eq. 30. The divisive normalization, Eq. 10, reproduced above depends on the exponent γ^i through the vector of energies $\mathbf{e}^i = |\mathbf{y}^i|^{\gamma^i}$. Therefore,

$$\nabla_{\gamma^i} \mathcal{N}^{(i)} = -\mathbb{D}_{\text{sign}(\mathbf{y}^i)} \cdot \mathbb{D}_{\mathcal{D}^{(i)}(\mathbf{e}^i)}^{-2} \cdot \frac{\partial \mathbb{D}_{\mathcal{D}^{(i)}(\mathbf{e}^i)}}{\partial \gamma^i} \cdot \mathbf{e}^i + \mathbb{D}_{\text{sign}(\mathbf{y}^i)} \cdot \mathbb{D}_{\mathcal{D}^{(i)}(\mathbf{e}^i)}^{-1} \cdot \frac{\partial \mathbf{e}^i}{\partial \gamma^i} \quad (72)$$

where, if we perturb γ , the vector in the diagonal gets perturbed, so,

$$\frac{\partial \mathbb{D}_{\mathcal{D}^{(i)}(\mathbf{e}^i)}}{\partial \gamma^i} = \mathbb{D}_{\frac{\partial \mathcal{D}^{(i)}(\mathbf{e}^i)}{\partial \gamma^i}} = \mathbb{D}_{\frac{\partial \mathcal{D}^{(i)}(\mathbf{e}^i)}{\partial \mathbf{e}^i} \cdot \frac{\partial \mathbf{e}^i}{\partial \gamma^i}} \quad (73)$$

where the chain rule was also applied. Now, lets address the two derivatives in Eq. 73. First, given that $\mathcal{D}^{(i)}(\mathbf{e}^i) = \mathbf{b}^i + H^i \cdot \mathbf{e}^i$, the first term is,

$$\frac{\partial \mathcal{D}^{(i)}(\mathbf{e}^i)}{\partial \mathbf{e}^i} = H^i \quad (74)$$

Regarding the second term in Eq. 73, $\nabla_{\gamma^i} \mathbf{e}^i$, by taking element-wise logarithms,

$$\log \mathbf{e}^i = \gamma^i \log |\mathbf{y}^i| \quad (75)$$

this is convenient because, on the one hand, following a reasoning similar to the one used in Eq. 70, namely chain rule and direct derivation, we have:

$$\frac{\partial \mathbf{e}^i}{\partial \gamma^i} = \mathbb{D}_{\mathbf{e}^i} \cdot \frac{\partial \log \mathbf{e}^i}{\partial \gamma^i} = \mathbb{D}_{\mathbf{e}^i} \cdot \log |\mathbf{y}^i| \quad (76)$$

Now, plugging Eqs. 74 and 76 into Eq. 73 and this in Eq. 72, we get Eq. 30. Note that $\nabla_{\gamma^i} \mathcal{N}^{(i)} \in \mathbb{R}^{d_i \times 1}$ as it should be since γ^i is scalar (a single parameter to be perturbed which affects to the set of d_i responses in \mathbf{x}^i).

Dependence on \mathbf{b}^i : Proof of Eq. 31. Before deriving with regard to \mathbf{b}^i , it is convenient to rearrange the terms in Eq. 10 to put the only parameter depending on \mathbf{b}^i (the denominator) at the end. As the Hadamard product is commutative we can rearrange terms, and using the diagonal matrix notation for the terms independent of \mathbf{b}^i ,

$$\mathcal{N}^{(i)} = \text{sign}(\mathbf{y}^i) \odot \mathbf{e}^i \odot \frac{1}{\mathcal{D}^{(i)}(\mathbf{e}^i)} = \mathbb{D}_{\text{sign}(\mathbf{y}^i)} \cdot \mathbb{D}_{\mathbf{e}^i} \cdot \frac{1}{\mathcal{D}^{(i)}(\mathbf{e}^i)} \quad (77)$$

Now, we derive the vector at the end (the Hadamard quotient with the denominator),

$$\nabla_{\mathbf{b}^i} \mathcal{N}^{(i)} = \mathbb{D}_{\text{sign}(\mathbf{y}^i)} \cdot \mathbb{D}_{\mathbf{e}^i} \cdot \frac{\partial (\mathbf{b}^i + H^i \cdot \mathbf{e}^i)^{-1}}{\partial \mathbf{b}^i} = -\mathbb{D}_{\text{sign}(\mathbf{y}^i)} \cdot \mathbb{D}_{\mathbf{e}^i} \cdot \mathbb{D}_{\mathcal{D}^{(i)}(\mathbf{e}^i)}^{-2} \cdot \mathbb{1} \quad (78)$$

which is Eq. 31. This Jacobian is a $d_i \times d_i$ matrix consistently with the dimensions of the output and of the vector \mathbf{b}^i .

Dependence on general H^i : Proof of Eq. 32. With the same rearrangement done in Eq. 77 to leave the denominator in the end, we take derivatives with regard to H^i ,

$$\nabla_{H^i} \mathcal{N}^{(i)} = \mathbb{D}_{\text{sign}(\mathbf{y}^i)} \cdot \mathbb{D}_{\mathbf{e}^i} \cdot \frac{\partial (\mathbf{b}^i + H^i \cdot \mathbf{e}^i)^{-1}}{\partial H^i} = -\mathbb{D}_{\text{sign}(\mathbf{y}^i)} \cdot \mathbb{D}_{\mathbf{e}^i} \cdot \mathbb{D}_{\mathcal{D}^{(i)}(\mathbf{e}^i)}^{-2} \cdot \frac{\partial H^i \cdot \mathbf{e}^i}{\partial H^i} \quad (79)$$

where, again, we apply the block diagonal result for the derivative of a linear function with regard to the parameters, Eq.68, leading to $\mathbb{B}_{\mathbf{e}^i}^{d_i}$ and hence obtaining Eq.32. Given this final block-diagonal term this Jacobian is a $d_i \times (d_i \times d_i)$ matrix, consistently with the number of parameters than may vary in H^i . Note also that small perturbations of the response from perturbations in H^i should be computed using is the column-wise rearrangement for H^i defined in Eq. 66.

Dependence on parametric kernels: Proof of Eqs. 35 and 36. Considering the Gaussian parametrization, Eq. 33, the derivative with regard to the width of the k -th row is,

$$\frac{\partial \mathcal{N}^{(i)}}{\partial \sigma_k^i} = \frac{\partial \mathcal{N}^{(i)}}{\partial H^i} \cdot \frac{\partial H^i}{\partial H_{k*}^i} \cdot \frac{\partial H_{k*}^i}{\partial \sigma_k^i} \quad (80)$$

The matrix that transmits the variations in a single row of the kernel into the whole vector-rearranged kernel, $\Delta \text{vect}(H^{i^\top}) = \frac{\partial H^i}{\partial H_{k*}^i} \cdot \Delta H_{k*}^{i^\top}$, has to be formed by $d_i - 1$ replicas of the zero matrix, with the identity matrix, $\mathbb{1}$, in the k -th location,

$$\frac{\partial H^i}{\partial H_{k*}^i} = \begin{pmatrix} \emptyset_{d_i \times d_i} \\ \emptyset_{d_i \times d_i} \\ \vdots \\ \emptyset_{d_i \times d_i} \\ \mathbb{1}_{d_i \times d_i} \\ \emptyset_{d_i \times d_i} \\ \vdots \\ \emptyset_{d_i \times d_i} \end{pmatrix} \begin{matrix} \text{1st submatrix} \\ \text{2nd submatrix} \\ \vdots \\ \vdots \\ \text{k-th submatrix} \\ \vdots \\ \text{d}_i\text{-th submatrix} \end{matrix} \quad (81)$$

This derivative, $\frac{\partial H^i}{\partial H_{k\star}^i}$, selects a single submatrix in the huge block-diagonal matrix, $\mathbb{B}_{\mathbf{e}^i}^{d_i}$, that is in $\frac{\partial \mathcal{N}^{(i)}}{\partial H^i}$, Eq. 32. As a result, this product leads to a square matrix where the only nonzero row is in the k -th location,

$$\mathbb{B}_{\mathbf{e}^i}^{d_i} \cdot \frac{\partial H^i}{\partial H_{k\star}^i} = \begin{pmatrix} \emptyset_{1 \times d_i} \\ \emptyset_{1 \times d_i} \\ \vdots \\ \emptyset_{1 \times d_i} \\ \mathbf{e}^{i\top} \\ \emptyset_{1 \times d_i} \\ \vdots \\ \emptyset_{1 \times d_i} \end{pmatrix} \begin{matrix} \text{1st row} \\ \text{2nd row} \\ \vdots \\ \text{\textit{k}-th row} \\ \vdots \\ \text{\textit{d}_i\text{-th row}} \end{matrix} \quad (82)$$

When multiplying the above matrix by the extra diagonal matrix in $\frac{\partial \mathcal{N}^{(i)}}{\partial H^i}$, Eq. 32, we have the only nonzero row scaled by the k -th component of the diagonal of $-\mathbb{D}_{\text{sign}(\mathbf{y}^i)} \cdot \mathbb{D}_{\mathbf{e}^i} \cdot \mathbb{D}_{\mathcal{D}^{(i)}(\mathbf{e}^i)}^{-2}$, i.e.

$$\frac{\partial \mathcal{N}^{(i)}}{\partial \sigma_k^i} = \begin{pmatrix} \emptyset_{1 \times d_i} \\ \emptyset_{1 \times d_i} \\ \vdots \\ \emptyset_{1 \times d_i} \\ -\text{sign}(y_k^i) e_k^i \mathcal{D}^{(i)k}{}^{-2} \mathbf{e}^{i\top} \\ \emptyset_{1 \times d_i} \\ \vdots \\ \emptyset_{1 \times d_i} \end{pmatrix} \cdot \frac{\partial H_{k\star}^i}{\partial \sigma_k^i} \quad (83)$$

Now, taking into account the straightforward derivative of a normalized 2D Gaussian with regard to its width,

$$\frac{\partial}{\partial \sigma} \left[c \frac{dp^2}{2\pi \sigma^2} \exp\left(-\frac{\Delta_{kk'}^2}{2\sigma^2}\right) \right] = c \frac{dp^2}{2\pi \sigma^5} (\Delta_{kk'}^2 - 2\sigma^2) \exp\left(-\frac{\Delta_{kk'}^2}{2\sigma^2}\right)$$

and considering that this holds $\forall k' \in \text{subband } k$, the considered $\frac{\partial H_{k\star}^i}{\partial \sigma_k^i}$ is a column vector:

$$\nabla_{\sigma_k^i} \mathcal{N}^{(i)} = \begin{pmatrix} \emptyset_{1 \times d_i} \\ \emptyset_{1 \times d_i} \\ \vdots \\ \emptyset_{1 \times d_i} \\ -\text{sign}(y_k^i) e_k^i \mathcal{D}^{(i)k}{}^{-2} \mathbf{e}^{i\top} \\ \emptyset_{1 \times d_i} \\ \vdots \\ \emptyset_{1 \times d_i} \end{pmatrix} \cdot \begin{pmatrix} F_{k1}^i \\ F_{k2}^i \\ F_{k3}^i \\ \vdots \\ F_{kd_i}^i \end{pmatrix} \quad (84)$$

where

$$F_{kk'}^i = \begin{cases} 0 & \forall k' \notin \text{subband } k \\ c_k^i \frac{dp_{k1} dp_{k2}}{2\pi \sigma_k^{i5}} \left(\Delta_{kk'}^2 - 2\sigma_k^{i2} \right) e^{-\frac{\Delta_{kk'}^2}{2\sigma_k^{i2}}} & \forall k' \in \text{subband } k \end{cases}$$

Note that the matrix-on-vector product in Eq. 84 is a vector with a single nonzero element (the one in the k -th location). Therefore, the derivatives with regard to all the widths can be expressed in a single matrix expression by replicating the transposed vector $\mathbf{e}^{i\top}$ in d_i rows, and

by stacking the different column vectors $F_{kk'}^i \forall k$. Then, the elements we are looking for are in the diagonal of the resulting matrix. This leads to the diagonal matrix in Eq. 35.

In the case of the derivative with regard to the amplitudes of the Gaussians, Eq. 83 also holds $\forall k$ with the corresponding change of variables. Then, taking into account that the remaining derivative with regard to the amplitude is simply the Gaussian, and the consideration of all coefficients k stacked leads to Eq. 36.

5.5 Derivation of the inverse

From Eq. 10, the vector of absolute values of the responses is $|\mathbf{x}^i| = \mathbb{D}_{(\mathbf{b}^i + H^i \cdot \mathbf{e}^i)}^{-1} \cdot \mathbf{e}^i$. Therefore, inverting the matrix, it holds,

$$\mathbb{D}_{(\mathbf{b}^i + H^i \cdot \mathbf{e}^i)} \cdot |\mathbf{x}^i| = \mathbf{e}^i$$

which can be written using the Hadamard product,

$$(\mathbf{b}^i + H^i \cdot \mathbf{e}^i) \odot |\mathbf{x}^i| = \mathbf{e}^i$$

Now, using the diagonal matrix notation of Hadamard products and the fact that $\mathbb{D}_{\mathbf{a}} \cdot \mathbf{b} = \mathbb{D}_{\mathbf{b}} \cdot \mathbf{a}$, we have:

$$\begin{aligned} \mathbb{D}_{\mathbf{b}^i} \cdot |\mathbf{x}^i| + \mathbb{D}_{|\mathbf{x}^i|} \cdot H^i \cdot \mathbf{e}^i &= \mathbf{e}^i \\ \mathbb{D}_{\mathbf{b}^i} \cdot |\mathbf{x}^i| &= (\mathbb{I} - \mathbb{D}_{|\mathbf{x}^i|} \cdot H^i) \cdot \mathbf{e}^i \\ \mathbf{e}^i &= (\mathbb{I} - \mathbb{D}_{|\mathbf{x}^i|} \cdot H^i)^{-1} \cdot \mathbb{D}_{\mathbf{b}^i} \cdot |\mathbf{x}^i| \end{aligned}$$

and considering that $\mathbf{e}^i = |\mathbf{y}^i|^{\gamma^i}$, and that \mathbf{y}^i inherits the sign from \mathbf{y}^i , it follows Eq. 39.

5.6 Region-based approach to MAXimum Differentiation

Analytic MAXimum Differentiation involves computing the eigenvectors of the metric matrix based on the Jacobian (Eq. 23). This matrix is huge even for moderate size images and one would like to break this problem into smaller (more tractable) pieces. Here we consider how a region-based strategy affects MAD optimization.

Independent processing of the distinct patches of an image implies assuming that perception of a patch is independent of the content of neighbor patches. Caution has to be taken with such an assumption. In fact, the main reason to include the nonlinear stage in a sensor is accounting for the masking effect of the neighbor sensors tuned to surrounding locations. The scale of the local interactions between the sensors (e.g. the width of the linear receptive fields in the rows of the L^i matrices and the width of the interaction in the rows of the H^i matrices) will induce edge effects if patch size is limited. Therefore, this is the length scale that must be taken into account in order to break the problem into pieces. As an example, in our case (in the model used in the Discussion) the wider interaction has a length scale of 0.2 degrees (see the specific values of the parameters in Supplementary Material 3).

Here, we point out that assuming region-independence in perception implies certain structure in $\nabla_{\mathbf{x}^0} S$. This structure has consequences on the metric matrix, which leads to simplified solutions of MAD, which are also consistent with the original region-independence assumption and with the quadratic summation assumption.

Imagine that large images are formed by N distinct spatial blocks. In this case, data corresponding to the difference between two images can be arranged in a column vector by stacking the vectors corresponding to the N distinct regions: $\Delta \mathbf{x}^0 = (\Delta \mathbf{x}_{[1]}^0 \top \Delta \mathbf{x}_{[2]}^0 \top \cdots \Delta \mathbf{x}_{[N]}^0 \top)^\top$. Assuming that these distinct regions are perceptually independent, implies a block-diagonal structure in $\nabla_{\mathbf{x}^0} S$, because the variation of the responses corresponding to the i -th region

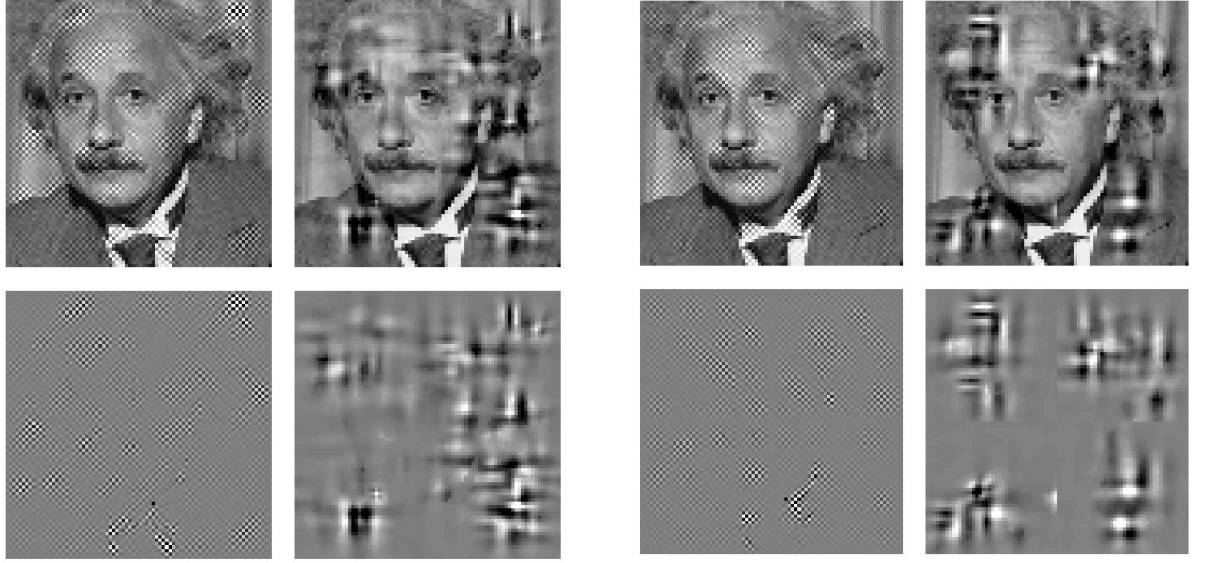


Fig 12. Global vs region-based MAD computation. *Left:* best and worst MAD-analytic images computed from an image subtending 1.25 deg. *Right:* best and worst MAD-analytic images computed from 4 subimages subtending 0.63 deg each.

should not depend on the variation of the inputs for the j -th region:

$$\begin{pmatrix} \Delta \mathbf{x}_{[1]}^n \\ \Delta \mathbf{x}_{[2]}^n \\ \vdots \\ \Delta \mathbf{x}_{[N]}^n \end{pmatrix} = \begin{pmatrix} \nabla_{\mathbf{x}_{[1]}^0} S(\mathbf{x}_{[1]}^0) & \emptyset_{d_n \times d_0} & \cdots & \emptyset_{d_n \times d_0} \\ \emptyset_{d_n \times d_0} & \nabla_{\mathbf{x}_{[2]}^0} S(\mathbf{x}_{[2]}^0) & \cdots & \emptyset_{d_n \times d_0} \\ \vdots & \vdots & \ddots & \vdots \\ \emptyset_{d_n \times d_0} & \emptyset_{d_n \times d_0} & \cdots & \nabla_{\mathbf{x}_{[N]}^0} S(\mathbf{x}_{[N]}^0) \end{pmatrix} \cdot \begin{pmatrix} \Delta \mathbf{x}_{[1]}^0 \\ \Delta \mathbf{x}_{[2]}^0 \\ \vdots \\ \Delta \mathbf{x}_{[N]}^0 \end{pmatrix} \quad (85)$$

where each (relatively small) rectangular sub-matrix, $\nabla_{\mathbf{x}_{[i]}^0} S(\mathbf{x}_{[i]}^0)$, describes the behavior for the i -th region.

In this situation, in the 2nd-order (or local-linear) approximation, Eq. 23, the perceptual difference induced by the large $\Delta \mathbf{x}^0$ would be given by $d_p^2 = \Delta \mathbf{x}^{0\top} \cdot \nabla_{\mathbf{x}^0} S(\mathbf{x}^0)^\top \cdot \nabla_{\mathbf{x}^0} S(\mathbf{x}^0) \cdot \Delta \mathbf{x}^0$, and using the block diagonal structure in Eq. 85, one has:

$$d_p^2 = \begin{pmatrix} \Delta \mathbf{x}_{[1]}^{0\top} & \Delta \mathbf{x}_{[2]}^{0\top} & \cdots & \Delta \mathbf{x}_{[N]}^{0\top} \end{pmatrix} \cdot \begin{pmatrix} M(\mathbf{x}_{[1]}^0) & \emptyset_{d_0 \times d_0} & \cdots & \emptyset_{d_0 \times d_0} \\ \emptyset_{d_0 \times d_0} & M(\mathbf{x}_{[2]}^0) & \cdots & \emptyset_{d_0 \times d_0} \\ \vdots & \vdots & \ddots & \vdots \\ \emptyset_{d_0 \times d_0} & \emptyset_{d_0 \times d_0} & \cdots & M(\mathbf{x}_{[N]}^0) \end{pmatrix} \cdot \begin{pmatrix} \Delta \mathbf{x}_{[1]}^0 \\ \Delta \mathbf{x}_{[2]}^0 \\ \vdots \\ \Delta \mathbf{x}_{[N]}^0 \end{pmatrix} \quad (86)$$

where each (relatively small) square sub-matrix $M(\mathbf{x}_{[i]}^0) = \nabla_{\mathbf{x}_{[i]}^0} S(\mathbf{x}_{[i]}^0)^\top \cdot \nabla_{\mathbf{x}_{[i]}^0} S(\mathbf{x}_{[i]}^0)$ is the metric matrix corresponding to the i -th region.

Eq. 86 has one interesting consequence for its use in Maximum Differentiation: since the eigenvectors of a (large) block-diagonal matrix can be computed from the eigenvectors of the (smaller) blocks in the diagonal [87], there is no need to explicitly build and work with the huge matrices in Eqs. 85 and 86. This relieving mathematical result is completely consistent with intuition: if perceptual independence is assumed (and responses are computed block-wise), then, large MAD images can be also computed block-wise from the eigenvectors of the smaller metric matrices corresponding to each image block.

Figure 12 shows an example of the comparison of block-wise versus global approaches to compute MAD images. In both best and worst images (computed from eigenspaces with maximum and minimum eigenvalues) the energy is focused roughly in the same spatial regions with the same frequency content. Qualitative behavior is similar meaning that edge effects are negligible. Therefore, it is computationally sensible to take a block-wise approach.

A lateral consequence of Eq. 86 is related to the summation of distortions across the visual field. Note that the total distortion is the quadratic sum of individual distortions in the regions of the image, $\mathfrak{d}_p^2 = \sum_{i=1}^N \Delta \mathbf{x}_{[i]}^{0\top} \cdot M(\mathbf{x}_{[i]}^0) \cdot \Delta \mathbf{x}_{[i]}^0 = \sum_{i=1}^N \mathfrak{d}_p^{[i]2}$. This quadratic summation is consistent with the quadratic norm chosen for the summation over individual response elements.

5.7 Maximization of correlation with subjective opinion

The linear correlation between the ground truth, \mathbf{M} and the model predictions \mathbf{D} is,

$$\varrho = \frac{E((\mathbf{M} - \bar{\mathbf{M}})(\mathbf{D} - \bar{\mathbf{D}}))}{\sigma(\mathbf{M})\sigma(\mathbf{D})} \quad (87)$$

where $E(\cdot)$ stands for expected value, $\bar{\mathbf{v}}$ stands for the average of vector \mathbf{v} , and $\sigma(\cdot)$ stands for standard deviation.

However, there is a more convenient expression to apply the chain rule in the derivatives with regard to the parameters. Note that the sums in the average to compute $E(\cdot)$ and $\sigma(\cdot)$ can be written as dot products and norms, and subtraction of the mean can be written as $\mathbf{M}_s = \mathbf{M} - \frac{1}{N} \cdot \mathbf{1} \cdot \mathbf{M}$, where $\mathbf{1}$ is an all-ones matrix. As a result, the linear correlation can be written as,

$$\varrho = \frac{\mathbf{M}_s^T \cdot \mathbf{D}_s}{|\mathbf{M}_s| |\mathbf{D}_s|} \quad (88)$$

In this way, the derivatives of $\varrho(\boldsymbol{\Theta})$ with regard to $\boldsymbol{\Theta}$:

$$\frac{d\varrho}{d\boldsymbol{\Theta}} = \frac{d\varrho}{d\mathbf{D}_s} \cdot \frac{d\mathbf{D}_s}{d\boldsymbol{\Theta}} \quad \text{where} \quad \begin{cases} \frac{d\varrho}{d\mathbf{D}_s} \in \mathbb{R}^{1 \times N} \\ \frac{d\mathbf{D}_s}{d\boldsymbol{\Theta}} \in \mathbb{R}^{N \times m} \end{cases} \quad (89)$$

Developing the term (1)

$$\begin{aligned} \frac{d\varrho}{d\mathbf{D}_s} &= \frac{d}{d\mathbf{D}_s} \left[\frac{\mathbf{M}_s^T \mathbf{D}_s}{|\mathbf{M}_s| \cdot |\mathbf{D}_s|} \right] \\ &= \frac{\mathbf{M}_s^T}{|\mathbf{M}_s| \cdot |\mathbf{D}_s|} + \frac{\mathbf{M}_s^T \mathbf{D}_s}{|\mathbf{M}_s|} \cdot \frac{d}{d\mathbf{D}_s} (\mathbf{D}_s^T \cdot \mathbf{D}_s)^{-1/2} \\ &= \frac{\mathbf{M}_s^T}{|\mathbf{M}_s| \cdot |\mathbf{D}_s|} - \frac{1}{2} \frac{\mathbf{M}_s^T \mathbf{D}_s}{|\mathbf{M}_s|} \cdot (\mathbf{D}_s^T \cdot \mathbf{D}_s)^{-3/2} \cdot \frac{d}{d\mathbf{D}_s} (\mathbf{D}_s^T \cdot \mathbf{D}_s) \\ &= \frac{\mathbf{M}_s^T}{|\mathbf{M}_s| \cdot |\mathbf{D}_s|} - \frac{\mathbf{M}_s^T \mathbf{D}_s}{|\mathbf{M}_s|} \cdot \frac{1}{|\mathbf{D}_s|^3} \cdot \mathbf{D}_s^T \\ &= \frac{\mathbf{M}_s^T}{|\mathbf{M}_s| \cdot |\mathbf{D}_s|} - \frac{\mathbf{M}_s^T \mathbf{D}_s}{|\mathbf{M}_s| \cdot |\mathbf{D}_s|^3} \cdot \mathbf{D}_s^T \end{aligned} \quad (90)$$

Developing the term (2)

$$\frac{d\mathbf{D}_s}{d\boldsymbol{\Theta}} = \frac{d}{d\boldsymbol{\Theta}} \left(\mathbf{D} - \frac{1}{N} \mathbf{1} \mathbf{D} \right) = \frac{d\mathbf{D}}{d\boldsymbol{\Theta}} - \frac{1}{N} \mathbf{1} \frac{d\mathbf{D}}{d\boldsymbol{\Theta}} \quad (91)$$

where,

$$\frac{d\mathbf{D}}{d\boldsymbol{\Theta}} = \begin{pmatrix} \frac{\partial \mathfrak{d}_p^{[1]}}{\partial \boldsymbol{\Theta}} \\ \frac{\partial \mathfrak{d}_p^{[2]}}{\partial \boldsymbol{\Theta}} \\ \vdots \\ \frac{\partial \mathfrak{d}_p^{[N]}}{\partial \boldsymbol{\Theta}} \end{pmatrix},$$

where, for the i-th image,

$$\begin{aligned}
\frac{\partial d_p^{[i]}}{\partial \Theta} &= \frac{\partial (\Delta \mathbf{x}_{[i]}^n \cdot \Delta \mathbf{x}_{[i]}^n)^{1/2}}{\partial \Theta} = \frac{1}{2d_p^{[i]}} \cdot \frac{\partial (\Delta \mathbf{x}_{[i]}^n \cdot \Delta \mathbf{x}_{[i]}^n)}{\partial \Theta} \\
&= \frac{1}{2d_p^{[i]}} 2 \cdot \Delta \mathbf{x}_{[i]}^n \cdot \frac{\partial \Delta \mathbf{x}_{[i]}^n}{\partial \Theta} \\
&= \frac{1}{d_p^{[i]}} \cdot \Delta \mathbf{x}_{[i]}^n \cdot \frac{\partial (\mathbf{z}_{[i]}^n - \mathbf{x}_{[i]}^n)}{\partial \Theta} \\
&= \frac{1}{d_p^{[i]}} \cdot \Delta \mathbf{x}_{[i]}^n \cdot \left(\frac{\partial \mathbf{z}_{[i]}^n}{\partial \Theta} - \frac{\partial \mathbf{x}_{[i]}^n}{\partial \Theta} \right) \\
&= \frac{1}{d_p^{[i]}} \cdot \Delta \mathbf{x}_{[i]}^n \cdot [\nabla_{\Theta} S(\mathbf{z}_{[i]}^0) - \nabla_{\Theta} S(\mathbf{x}_{[i]}^0)] \tag{92}
\end{aligned}$$

Plugging Eqs. 90-92 into Eq. 89, one gets Eq. 45.

5.8 The BioMultiLayer-L+NL Toolbox

This **Matlab** toolbox implements all the maths related to the kind of multilayer feedforward L+NL neural models considered in the paper. Specifically, it implements the vision model detailed in the Supplementary Material 5.1, which consists of a cascade of isomorphic linear+nonlinear transforms based on linear receptive fields and canonical Divisive Normalization nonlinearities).

The **BioMultiLayer-L+NL** toolbox includes the forward transform, the inverse, and all the derivatives (w.r.t. the signal and w.r.t. the parameters). The derivatives allow (i) Novel M_AXimum Differentiation (MAD) psychophysics and (ii) fitting the model from classical psychophysics. The inverse allows improved decoding of neural signals.

For convenience, this release includes other public-domain toolboxes (please cite these sources as well):

- CSF of the Standard Spatial Observer (**SS0** folder) by J. Malo and A.B. Watson [39].
- Steerable wavelet pyramid (**matlabPyrTools** folder) by E.P. Simoncelli [104].

5.8.1 Installing the toolbox

- (1) Download the toolbox from http://isp.uv.es/docs/BioMultiLayer_L_NL.zip.
- (2) Decompress all the contents of the file.
- (3) Compile the mex files of the **matlabPyrTools** toolbox.
- (4) Include the folders in the Matlab path.

Once the toolbox is installed you may enter **help BioMultiLayer_L_NL** at the Matlab prompt to get an overview of all the routines in the toolbox. It is convenient to take a look at the demo scripts included in the toolbox for worked-out examples.

5.8.2 Basic routines: responses, derivatives and inverse

The basic use of the **BioMultiLayer-L+NL** toolbox reduces to two routines (the forward and the inverse transform):

- Given an image, **deep_model_DN_isomorph.m** computes the responses and the Jacobians of the vision model made of isomorphic Linear+Nonlinear layers with Divisive Normalization. This function sequentially calls **stage_L_NL.m** that computes the response and the Jacobians of a single layer in the network.
- Given a response vector, **inv_deep_model_DN_isomorph.m** decodes the response and reconstructs the input image. This function sequentially calls the function **inv_stage_L_NL.m** that computes the inverse of a single layer in the network.

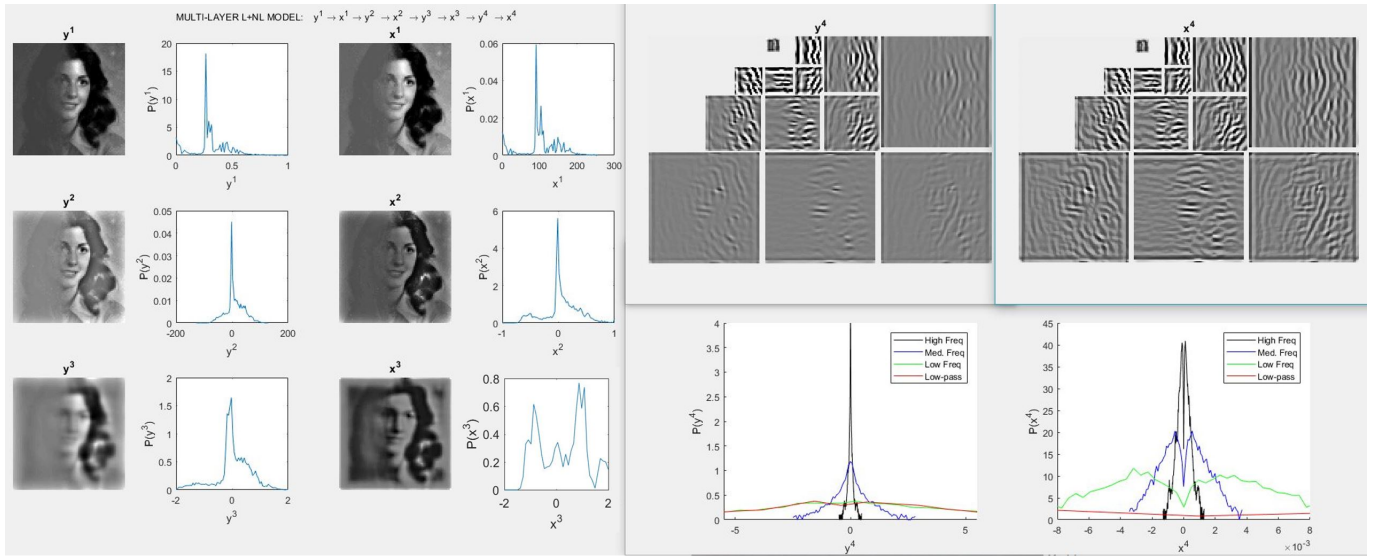


Fig 13. Forward Transform (in the demo script `demo_deep_DN_iso.m`). Responses and marginal PDFs along the layers of the network. Note that the bimodal PDFs of \mathbf{x}^3 and \mathbf{x}^4 are consistent with the predictive behavior reported in [62]. Equalization behavior at \mathbf{x}^1 reported at [63] is not that evident in this example because this is a low-dynamic-range image.

The user is referred to the `help` of these functions for details on how to use them. Additionally, step-by-step examples on how to use the above functions is given in the demo script `demo_deep_DN_iso.m`. Particularly relevant is how to select which Jacobian(s) should be computed. This is controlled with a structure described in the `help` of `stage_L_NL.m`.

Initialization note: before using the above utilities, (a) images have to be prepared for the toolbox, and (b) the parameters of the model have to be set.

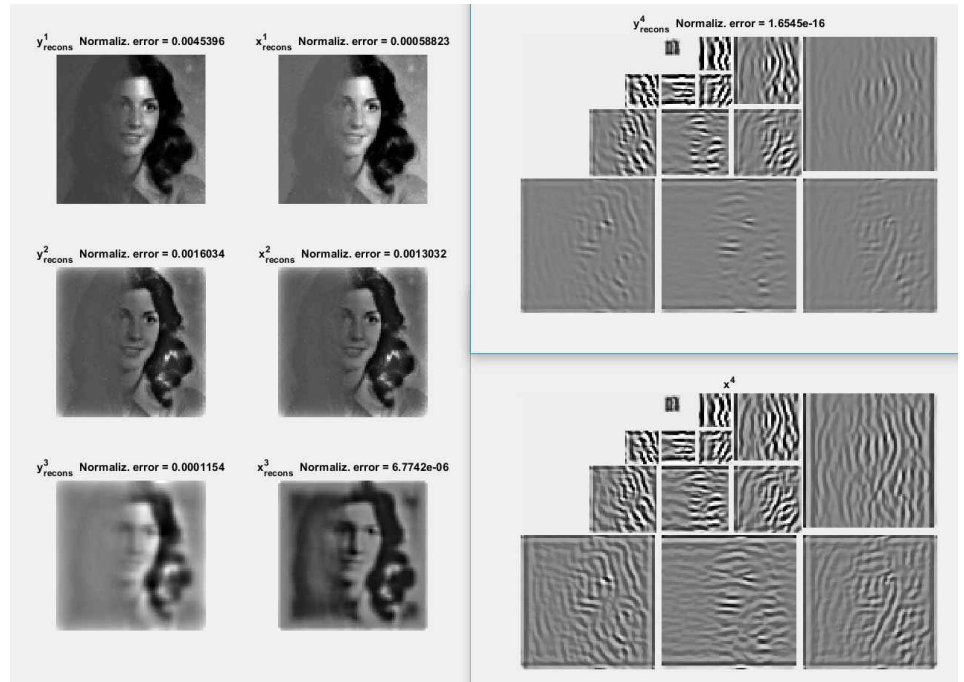


Fig 14. Inverse Transform (in the demo script `demo_deep_DN_iso.m`). Decoded signals from the response at the last layer of the network.

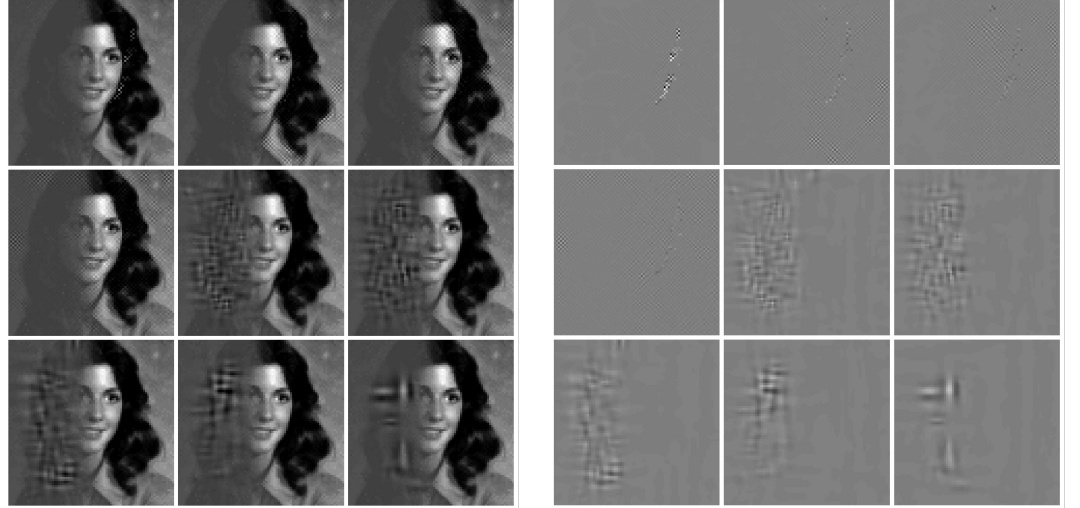


Fig 15. Derivatives w.r.t. the signal: Analytic MAD (in the demo script `demo_deep_DN_iso.m`)
Left panel: Distorted images in the directions of low and high eigenvalues of the 2nd order metric matrix. Low eigendistortions correspond to the upper-left images where distortions are not noticeable, and high eigendistortions correspond to the lower-right images where distortions are highly noticeable. Right panel: isolated distortions. All the distortions have the same energy (induce the same MSE), but they are visually very different. Note that highly visible distortions are concentrated in the low contrast part of the image (and the other way around for highly visible distortions), which is consistent with the masking phenomenon and indicates the quality of the model.

(a) Input stimuli, image normalization, and image arrangement The current version of the `BioMultiLayer-L+NL` toolbox operates on *achromatic images* in normalized luminance units. This means that in the current implementation the model starts from luminance vectors, \mathbf{y}^0 , and not from hyperspectral stimuli, \mathbf{x}^0 . In other words, the spectral and the chromatic elements of the first stage in Fig. 1, or the linear integration of the spectrum, L^1 , in Eq. 46, are not included in this release. This missing linear stage, L^1 , can be easily implemented using the `Colorlab` toolbox [105]. Specifically, the `Colorlab` functions `spect2tri.m` and `xyz2atd.m` compute CIE XYZ tristimulus values from radiances, and transform the CIE XYZ result to convenient opponent chromatic representations (luminance, red-green and yellow-blue) [76, 101].

Normalized luminance refers to division by *what is assumed to be the maximum luminance in the considered class of scenes*. This implies that input values in \mathbf{y}^0 are mainly in the $[0, 1]$ range except for highlights that may be over 1. See the comment on proper image normalization and luminance calibration in `deep_model_DN_isomorph.m`. More accurate transforms from conventional digital images to tristimulus images can be done using the `Colorlab` [105] or the `Psychtoolbox` [106].

If your input luminance image is a matrix, \mathbf{y}^0 , vector arrangement according to the *last-dimension-first* convention cited in Eq. 1, is simply obtained using `y0(:)`, and large images can be patch-wise vectorized using `im2col.m`. The `BasicVideoTools` toolbox [107] has convenient generalizations of these vectorization functions to be applied in spatio-spectral (or spatio-temporal) arrays (namely `im2colcube.m` and `col2imcube.m`). These could be applied to extend the current toolbox to start from the hyperspectral stimulus \mathbf{x}^0 instead of starting from \mathbf{y}^0 .

(b) Model parameters The considered network has many parameters. The Jacobians implemented in this toolbox enable experimental methods to determine the parameters. In fact, a side result of this paper is the specific set of values of the parameters obtained from MAD psychophysics and image quality optimization. These parameters have to be passed to different functions of the `BioMultiLayer-L+NL` toolbox in a specific `struct` variable. In order to simplify the construction of the parameter variable, it is generated in the script `parameters_DN_isomorph.m`. An example on how to set the parameters and call the script is given in `demo_deep_DN_iso.m`. If you are happy with certain set of parameters, you may store them in a `*.mat` file so that you will not need to generate them again.

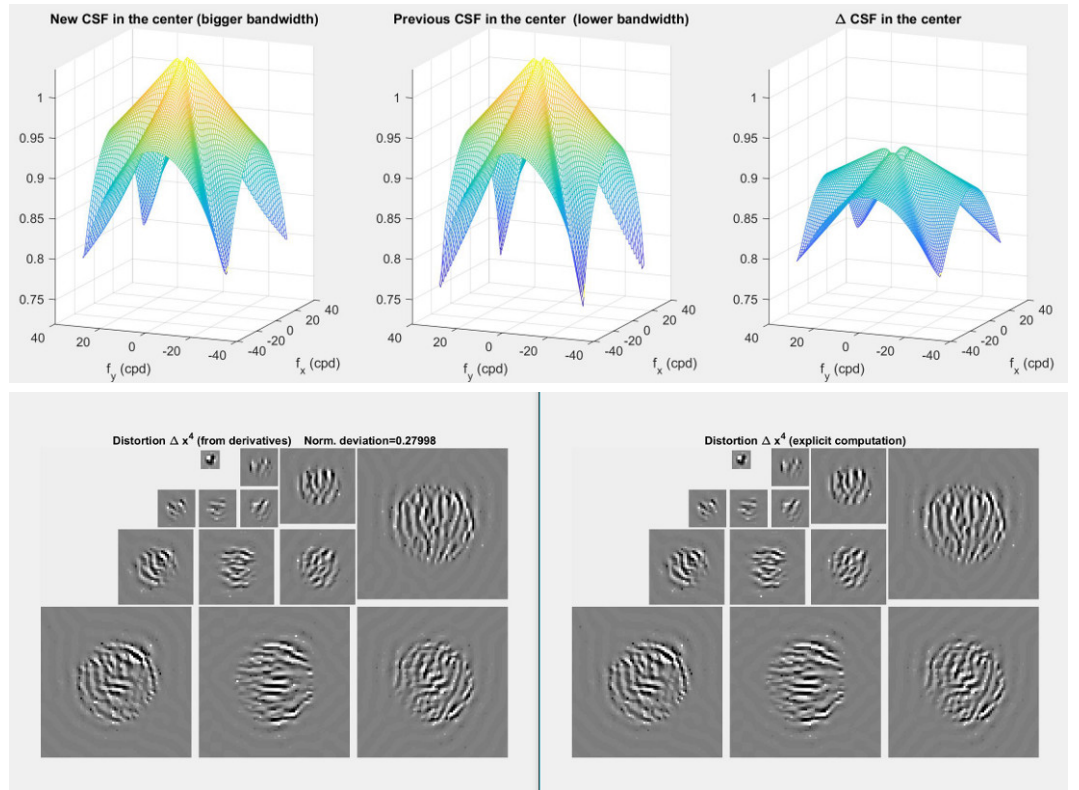


Fig 16. Derivatives w.r.t. the parameters: Propagation of the perturbation in the CSF (in the demo script `demo_deep_DN_iso.m`) Imagine a modification in the CSF filter of stage 3. For instance, increasing the bandwidth of the filter. How would it affect the response?. This can be done in two different ways: (1) the exact one (compute the response with and without the modification and subtract), and (2) using the first order approximation based on the Jacobian of the response w.r.t. the parameters (linearly propagate the effect of the modification). The top panel shows the different filter functions used in the center of the visual field, and the bottom panel shows the corresponding perturbation in the response computed exactly (right) and according to the first order approximation (left).

5.8.3 Advanced routines

The flexible vision model in the `BioMultiLayer-L+NL` toolbox may be used to (a) compute perceptual distances between images, (b) generate stimuli for MAXimum Differentiation (MAD), and (c) look for a specific model that maximizes the correlation with subjective opinion in image quality ratings. These advanced applications are available using:

- `metric_deep_DN_iso.m` computes the perceptual distance between an original image and a distorted image according to the multi-layer vision model. The use of this function is illustrated in the script `demo_metric_deep_DN_iso.m`.
- `mad_deep_DN_iso.m` performs the general MAXimum Differentiation (MAD) search for an image and a multi-layer vision model defined by its parameters. The use of this function and the equivalent analytic 2nd order result using eigenvectors of the metric is illustrated in the script `demo_mad_DN_iso.m`.
- `maximize_correlation_DN_iso.slurm` launches stochastic gradient descent search in the parameter space to look for the model that maximizes the correlation with the mean opinion score of subjectively rated image quality databases. A `*.slurm` function is invoked because this search is computationally expensive and the optimization has to be parallelized over multiple cores in a cluster. The folder `Corr_max_TID` contains an illustrative example of such parallelization.

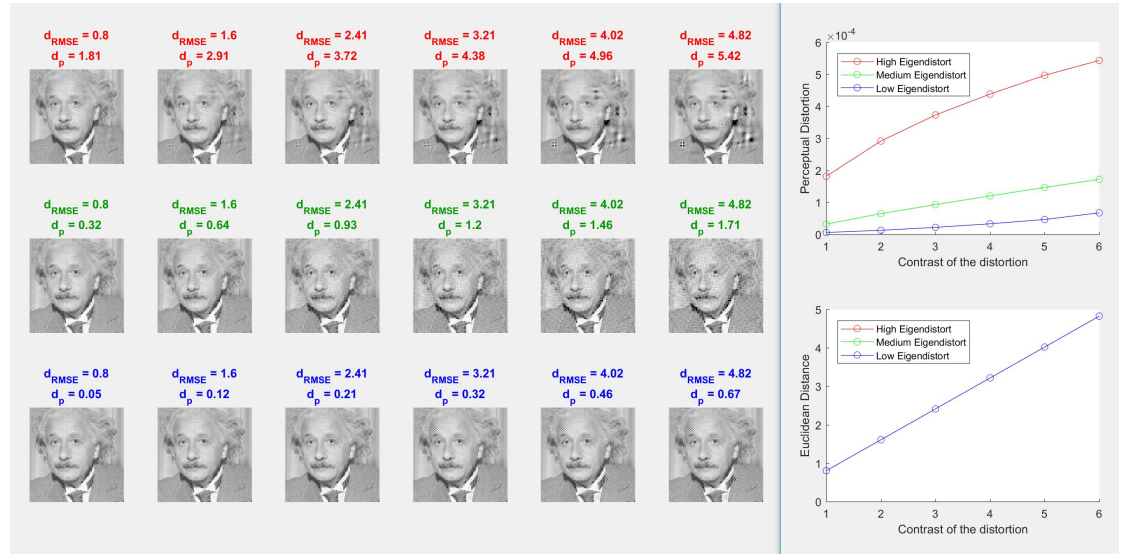


Fig 17. Perceptual distance (demo script demo.metric.DN.iso.m) Distortions of different nature (eigen distortions) of the metric of low, medium and high eigenvalue in the top, medium and bottom rows). The distortion linearly increases the RMSE contrast from left to right columns. The images in each column have the same RMSE (Euclidean distance) with regard to the original image. The numbers and the plots at the right display the Euclidean and the perceptual distances.

5.8.4 Demos

Basic use of the toolbox: [demo_deep_DN_iso.m](#) This script illustrates the use of the toolbox to compute: (1) the response at the different layers (2) the inverse (decoded signal) (3) the Jacobians (w.r.t. the signal and w.r.t. the parameters).

Responses (see Fig. 13) and inverses (see Fig. 14) are shown for an illustrative natural image with nonstationary contrast. Marginal PDFs of the responses are also shown in Fig. 13 to illustrate the predictive effect of Divisive Normalization. The Jacobian with regard to the stimuli is used to compute the 2nd order metric for that image. We compute eigen-distortions corresponding to such metric matrix and they make perceptual sense (see Fig. 15). The Jacobian with regard to the parameters is used to estimate the effect of perturbations of the model (see Fig. 16).

Perceptual distances: [demo.metric.deep.DN.iso.m](#) This script shows how the Euclidean distance in the response domain is substantially different from the Euclidean distance in the input space, and it is better correlated to subjective opinion. In this script, distortions of different nature are linearly scaled in contrast to lead to different distorted images. Euclidean and perceptual distances are computed and displayed together with the images (see Fig. 17).

MAXimum Differentiation search: [demo_mad_DN_iso.m](#) This script compares the three methods to generate maximally different images (1) General MAXimum Differentiation search (2) Simplified MAXimum Differentiation search based on the 2nd order approximation of distance (3) Analytic result based on the 2nd order approximation of distance. The procedure in this demo was used to compute the results in the Discussion section 3.1.

Checking the analytical expressions: [check_results.m](#) This script shows that the analytic results and the implementation are correct.

Analytic derivatives are compared to derivatives computed through finite differences. The analytic inverses and the inverses based on expansions are compared to the actual input. Derivatives and inverses are computed using patches from natural images (new patches are randomly selected in each realization of this script). Reasonable values for the parameters of the model are assumed. Agreement between the compared quantities is graphically and

STAGE 1			STAGE 2			STAGE 3			STAGE 4		
Error J.ny	6e-08	± 6e-08	Error J.sx	1.5e-05	± 0.3e-05	Error J.sx	1.4e-07	± 0.4e-07	Error J.sx *	4e-04	± 10e-04
			Error J.lx	5e-06	± 1e-06	Error J.lx	2.3e-08	± 0.4e-08	Error J.lx	5e-07	± 2e-07
			Error J.ny	2.9e-05	± 0.7e-05	Error J.ny	8e-07	± 5e-07	Error J.ny *	1e-03	± 3e-03
Error J.scale	2.9e-07	± 8e-08	Error J.L	6.8e-09	± 0.7e-09	Error J.L	8e-07	± 7e-07	Error J.b_full	0.8e-12	± 3e-12
Error J.b	1e-07	± 1e-07	Error L.pertur	7e-09	± 2e-09	Error L.pertur	2e-07	± 1e-07	Error J.b_subbnd	5e-08	± 4e-08
Error J.g	3e-08	± 1e-08	Error L.update	7e-09	± 2e-09	Error L.update	2e-07	± 1e-07	Error J.b_scale	8e-08	± 7e-08
Error J.beta	5e-08	± 3e-08	Error J.Lc	1.9e-06	± 0.2e-06	Error J.b	4e-07	± 1e-07	Error J.b	4e-07	± 5e-08
			Error J.Lc	7e-08	± 0.6e-08	Error J.g	3.6e-08	± 0.3e-08	Error J.g	3e-07	± 10e-07
			Error J.b	9e-08	± 1e-08	Error J.H	6e-07	± 3e-07	Error J.Hs_full *	2e-02	± 0.2e-02
			Error J.H	2.2e-07	± 0.2e-07	Error H.pertur	6e-07	± 4e-07	Error J.Hs_subbnd	1.0e-06	± 0.3e-06
			Error H.pertur	1.9e-07	± 0.2e-07	Error H.update	6e-07	± 3e-07	Error J.Hs_scale	1.1e-06	± 0.3e-06
			Error H.update	1.9e-07	± 0.2e-07	Error J.Hs	2.2e-06	± 0.5e-06	Error J.Hs	1.3e-06	± 0.4e-06
			Error J.Hs	4.2e-07	± 0.9e-07	Error J.Hc	9.2e-08	± 0.1e-08	Error J.Hc_full *	2e-06	± 1e-06
			Error J.Hc	6.7e-08	± 0.5e-08				Error J.Hc_subbnd	6e-06	± 2e-06
									Error J.Hc_scale	6e-06	± 2e-06
									Error J.Hc	8e-06	± 2e-06
Error Inv_analyt	4e-12	± 14e-12	Error Inv_ana_LNL	5.2e-16	± 0.8e-16	Error Inv_ana_LNL	7e-14	± 1e-14	Error Inv_exp_LNL	2.2e-06	± 0.9e-06
Error Inv_expans	5e-03	± 2e-03	Error Inv_ana_NL	4.0e-16	± 0.5e-16	Error Inv_ana_NL	9e-16	± 3e-16	Error Inv_exp_NL	1.2e-16	± 0.2e-17
			Error Inv_exp_LNL	5.0e-16	± 0.6e-16	Error Inv_exp_LNL	1e-04	± 4e-04	Error Inv_ana_LNL	2.3e-06	± 0.9e-06
			Error Inv_exp_NL	3.0e-16	± 0.5e-16	Error Inv_exp_NL	1e-04	± 4e-04	Error Inv_ana_NL	4.9e-16	± 0.5e-16
			Error Inv_expans	1e-07	± 7e-07	Error Inv_analyt	2e-11	± 1e-11	Error Inv_analyt	3e-05	± 1e-05
			Error inv_analyt	8e-11	± 40e-11	Error Inv_expans	5e-04	± 10e-04	Error Inv_expans	1e-03	± 2e-03

Table 1. Numerical check of analytical Jacobians and Inverses. Data displays the normalized error. Normalized error for the Jacobians stands for the ratio of the 2-norm of the numerical-vs-analytical deviation over the 2-norm of the analytical result. For the inverses the normalized error stands for the ratio of the 2-norm of the deviation of the reconstructed signal over the 2-norm of the input signal. The different columns contain the errors at the different stages. The data-blocks from top to bottom are: (1) errors of the derivatives w.r.t. the signal (check of Result I), (2) errors of the derivatives w.r.t. the parameters (check of Result II), and (3) errors of the inverses (isolated in each stage, and propagated through the stages). These numerical experiments were carried out using `check_results.m`. Small errors (errors are always orders of magnitude lower than the actual value) show that expressions and implementation are correct. We highlighted in color the larger errors. Errors of different color indicate different nature in the source of the deviation. Errors in green are obtained at the inverse using the expansion method. As expected, these errors decrease by increasing the number of terms in the expansion (i.e. it is only a matter of increasing the cpu time). Errors in blue come from checking the analytical derivative with finite differences. The finite nature of the increment induces an error. These errors decrease by decreasing the size of the finite difference step. Not a theoretical problem either. Finally, errors in orange correspond to the case where too small increments lead to noisy variations of functions (imagine the differences induced in a Gaussian kernel due to a very small difference in its width). This introduces extra errors that accumulate when considering huge kernels (as is the case in the 4th stage). These deviations reduce when reducing the size of the finite difference in the numerical derivative.

numerically assessed. *Graphic assessment:* Values of the analytic results are plotted versus the equivalent numerical results. Good alignment along the unit-slope diagonal means good agreement. *Numeric assessment:* Deviations between the compared results are expressed as ratios between the norm of the deviation over the norm of the analytic result. small values of this ratio mean good agreement.

A summary of the numeric results computed on 50 patches of natural images is given in Table 1.

5.9 Toolbox-oriented matrix properties

These properties are useful in the implementation of the model for large images or multiple image patches. These properties are particularly convenient in `Matlab` since it is not very efficient in building large diagonal matrices.

5.9.1 Products

Hadamard product and diagonal matrices. Useful to define divisive normalization (e.g. in Eq. 10)

$$\mathbf{a}.*\mathbf{b} = \mathbf{a} \odot \mathbf{b} = \mathbf{b} \odot \mathbf{a} = \mathbf{D}_\mathbf{a} \cdot \mathbf{b} = \mathbf{D}_\mathbf{b} \cdot \mathbf{a} \quad \text{with } \mathbf{a}, \mathbf{b} \in \mathbb{R}^{d \times 1}, \quad \mathbf{D}_\mathbf{a}, \mathbf{D}_\mathbf{b} \in \mathbb{R}^{d \times d} \quad (93)$$

Kronecker product and matrix replication. This non-commutative product is useful to avoid the large diagonal matrices below.

$$\text{repmat}(\mathbf{A}, \mathbf{m}, \mathbf{n}) = \text{kron}(\text{ones}(\mathbf{m}, \mathbf{n}), \mathbf{A}) = \mathbf{1}_{\mathbf{m} \times \mathbf{n}} \otimes \mathbf{A} \quad (94)$$

5.9.2 Large matrices (single image patch)

Left-multiplication by diagonal: weight each *row* of \mathbf{A} by the corresponding v_i (e.g. in Result I, Eq. 24):

$$\mathbf{D}_\mathbf{v} \cdot \mathbf{A} = (\mathbf{1}_{1 \times d} \otimes \mathbf{v}) \odot \mathbf{A} = \text{repmat}(\mathbf{v}, 1, d) .* \mathbf{A} \quad (95)$$

Right-multiplication by diagonal: weight each *column* of A by the corresponding v_i :

$$A \cdot \mathbb{D}_v = (\mathbb{1}_{d \times 1} \otimes \mathbf{v}^\top) \odot A = \text{repmat}(\mathbf{v}', d, 1) .* A \quad (96)$$

Large block-diagonal matrices in $\nabla_H S$: When dealing with derivatives w.r.t. non-parametric kernels in Result II (either to optimize the kernel or to compute the effect of perturbations) one find products involving huge block-diagonal matrices. These can be avoided:

- In optimization (use Eq. 32 in 45), `deltaS_times_blk_diagJ.m`:

$$\mathbf{a}^\top \cdot \mathbb{B}_{\mathbf{v}^\top}^d = (\mathbb{1}_{1 \times d_v} \otimes \mathbf{a}) \odot (\mathbb{1}_{d \times 1} \otimes \mathbf{v}^\top) \quad (97)$$

- In perturbations due to ΔH (apply 32), `blk_diagJ_times_deltaH.m`:

$$\mathbb{B}_{\mathbf{v}^\top}^d \cdot \text{vect}(\Delta H^\top) = \text{diag} \left((\mathbb{1}_{d \times 1} \otimes \mathbf{v}^\top) \cdot \Delta H^\top \right) \quad (98)$$

5.9.3 Even larger matrices (multiple image patches)

This is how different expressions change when working with N image vectors at the same time (stacked in a single matrix of size $d \times N$) as done by `im2col.m`.

Single vector	$\xrightarrow{\text{stack } N \text{ vectors}}$	Multiple vectors
<hr/>		
$\mathbf{v} \in \mathbb{R}^{d \times 1}$	\longrightarrow	$\mathbf{v} = \begin{pmatrix} \vdots & \vdots & & \vdots \\ \mathbf{v}^{[1]} & \mathbf{v}^{[2]} & \dots & \mathbf{v}^{[N]} \\ \vdots & \vdots & & \vdots \end{pmatrix} \in \mathbb{R}^{d \times N}$ and $\text{vect}(\mathbf{v}) = \begin{pmatrix} \mathbf{v}^{[1]} \\ \mathbf{v}^{[2]} \\ \vdots \\ \mathbf{v}^{[N]} \end{pmatrix} \in \mathbb{R}^{(Nd) \times 1}$
<hr/>		
$\Delta \mathbf{x}^i = \nabla_{\mathbf{x}^{i-1}} S^{(i)} \cdot \Delta \mathbf{x}^{i-1}$	\longrightarrow	$\text{vect}(\Delta \mathbf{x}^i) = \nabla_{\mathbf{x}^{i-1}} S^{(i)} \cdot \text{vect}(\Delta \mathbf{x}^{i-1})$
where $\nabla_{\mathbf{x}^{i-1}} S^{(i)} \in \mathbb{R}^{d_i \times d_{i-1}}$		where $\nabla_{\mathbf{x}^{i-1}} S^{(i)} \in \mathbb{R}^{Nd_i \times Nd_{i-1}}$ is block-diag. but stored by convenience as $\in \mathbb{R}^{(Nd_i) \times d_{i-1}}$
<hr/>		
$\Delta \mathbf{x}^i = \nabla_{\boldsymbol{\Theta}^i} S^{(i)} \cdot \Delta \boldsymbol{\Theta}^i$	\longrightarrow	$\text{vect}(\Delta \mathbf{x}^i) = \nabla_{\boldsymbol{\Theta}^i} S^{(i)} \cdot \Delta \boldsymbol{\Theta}^i$
where $\nabla_{\boldsymbol{\Theta}^i} S^{(i)} \in \mathbb{R}^{d_i \times d_{\boldsymbol{\Theta}^i}}$		where $\nabla_{\boldsymbol{\Theta}^i} S^{(i)} \in \mathbb{R}^{(Nd_i) \times d_{\boldsymbol{\Theta}^i}}$
<hr/>		
$\mathbb{D}_v \cdot A$	\longrightarrow	$(\mathbb{1}_{1 \times d} \otimes \text{vect}(\mathbf{v})) \odot (\mathbb{1}_{N \times 1} \otimes A)$
<hr/>		
$A \cdot \mathbb{D}_v$	\longrightarrow	$(\mathbf{v}^\top \otimes \mathbb{1}_{d \times 1}) \odot (\mathbb{1}_{N \times 1} \otimes A)$
<hr/>		